PHYSICAL REVIEW D **109,** 094515 (2024)

$B \to D^*$ and $B_s \to D_s^*$ vector, axial-vector and tensor form factors for the full q^2 range from lattice QCD

Judd Harrison,[*] and Christine T. H. Davies[†]

(HPQCD Collaboration)[‡]

SUPA, School of Physics and Astronomy, University of Glasgow, Glasgow, G12 8QQ, United Kingdom

(Received 24 July 2023; accepted 15 April 2024; published 29 May 2024)

We compute the complete set of Standard Model (SM) and tensor $B \to D^* \ell\bar{\nu}$ and $B_s \to D_s^* \ell\bar{\nu}$ semileptonic form factors across the full kinematic range of the decays using second generation MILC $n_f = 2 + 1 + 1$ highly improved staggered quark (HISQ) gluon field configurations and HISQ valence quarks, with the *heavy-HISQ* method. Lattice spacings range from 0.09 to 0.044 fm with pion masses from $\approx$300 MeV down to the physical value and heavy quark masses ranging between $\approx 1.5 m_c$ and $4.1 m_c \approx 0.9 m_b$; currents are normalized nonperturbatively. Using the recent untagged $B \to D^* \ell\bar{\nu}_\ell$ data from Belle and $B_s \to D_s^* \mu\bar{\nu}_\mu$ from LHCb together with our form factors, we determine a model independent value of $V_{cb} = 39.03(56)_{\mathrm{exp}}(67)_{\mathrm{latt}} \times 10^{-3}$, in agreement with previous exclusive determinations and in tension with the most recent inclusive result at the level of 3.6σ. We also observe a $\approx 1\sigma$ tension between the shape of the differential decay rates computed using our form factors and those measured by Belle. We compute a purely theoretical Standard Model value for the ratio of semitauonic and semimuonic decay rates, $R(D^*) = 0.273(15)$, which we find to be closer to the recent Belle measurement and heavy flavor averaging group average than theory predictions using fits to experimental differential rate data for $B \to D^* \ell\bar{\nu}_\ell$. Determining V_{cb} from our form factors and the experimental total rate for $B \to D^* \ell\nu$ also gives a value in agreement with inclusive results. We also compute the longitudinal polarization fraction for the semitauonic mode, $F_L^{D^*} = 0.395(24)$, which is in tension at the level of 2.2σ with the recent Belle measurement. Our calculation combines $B \to D^*$ and $B_s \to D_s^*$ lattice results in a simultaneous chiral continuum extrapolation, maintaining correlations between both modes. We then give results for both $B \to D^*$ and $B_s \to D_s^*$, with the $B_s \to D_s^*$ results superseding our previous lattice computation. We also give the chiral perturbation theory needed to analyze the tensor form factors.

DOI: 10.1103/PhysRevD.109.094515

I. INTRODUCTION

Semileptonic and leptonic decays of mesons allow for many high precision tests of the Standard Model (SM) description of the weak interaction. For example, in the SM the Cabibbo-Kobayashi-Maskawa (CKM) matrix, which encodes the couplings of flavor-changing quark currents with the SM W bosons, is unitary. Determinations of the CKM matrix elements using the weak decays of mesons [1,2] allow us to check if the unitarity constraints are satisfied. Currently those coming from the first row and column, which describe the couplings with up and down quarks, are in tension with unitarity at the level of 3σ [3].

The CKM matrix element V_{cb}, governing the strength of the quark level $b \to c\ell\bar{\nu}_\ell$ transition, can be determined most precisely either from inclusive semileptonic B decays, where all charmed final states are included, or from exclusive semileptonic decays to a specific charmed meson. The inclusive determination of V_{cb}, which uses the operator product expansion [4] to express the nonperturbative physics in terms of matrix elements of local operators with B mesons, gives $|V_{cb}| = 42.16(51) \times 10^{-3}$ [5].

Until very recently the exclusive determination only used experimental data for $B \to D$ and $B \to D^*$. This data has typically been extrapolated to the zero recoil point, where the $D^{(*)}$ meson is at rest, before being compared to lattice determinations [6,7] of the single form factor relevant at

---

[*] judd.harrison@glasgow.ac.uk
[†] christine.davies@glasgow.ac.uk
[‡] http://www.physics.gla.ac.uk/HPQCD

this point. Recently, $B_s \to D_s^{(*)}$ experimental data from LHCb was used together with HPQCD's early calculation of the $B_s \to D_s$ form factors [8] (as well as the $B_s \to D_s^*$ form factor at zero recoil [9]) to provide a complementary determination of V_{cb}. Averaging $B_{(s)} \to D_{(s)}^{(*)}$ results gives a value of $|V_{cb}| = 38.90(53) \times 10^{-3}$ [10], in tension at the level of 4.4σ with the most recent inclusive result. This determination is most sensitive to $B \to D^*$ data, which is much more precise than existing $B_s \to D_s^{(*)}$ data, and is preferred over $B \to D$ owing to the kinematic factors appearing in the differential rate, which allow for more data to be collected near zero recoil and thus for a more precise extrapolation to this point. Note that while lattice form factors for $B \to D$ are available away from zero recoil [11], extrapolation of experimental data to zero recoil is still used in order to straightforwardly average experimental results [10].

The extrapolation of experimental data to the zero recoil point has typically been done using either the Caprini, Lellouch, and Neubert (CLN) parametrization scheme [12], or the Boyd, Grinstein, and Lebed (BGL) parametrization scheme [13]. The CLN scheme imposes strong unitarity constraints based on heavy quark symmetry, and uses heavy quark effective theory (HQET) to reduce the number of independent parameters. This results in a highly constrained fit with only a single parameter able to modify the shape of the form factors. This approach has been widely criticized as underestimating residual uncertainties [14–16], and theoretical analyses of the 2017 Belle dataset [17] indicated that CLN was not well suited to describe the data [18,19]. The BGL scheme is more general, imposing unitarity bounds based on analyticity [13]. Early analyses of the 2017 Belle dataset indicated that the use of BGL, as opposed to CLN, would go some way to resolving the tension between inclusive and exclusive decays [15,18,20]. However, analysis of the more recent larger untagged dataset from Belle [21] instead finds very similar central values and uncertainties for V_{cb} using BGL and CLN schemes, both in similar tension with the inclusive result at the same level as previous exclusive results.

Recent advances in lattice QCD have allowed for the calculation of pseudoscalar to vector form factors for b-quark decays across the full kinematic range of the decays, with HPQCD producing the first calculations for $B_c \to J/\psi$ [22] and $B_s \to D_s^*$ [23], related to $B \to D^*$ by the exchange of the light spectator quark with a charm or strange quark, respectively. These calculations used highly improved staggered quarks (HISQs) [24] for all quarks, and were carried out using the $n_{\mathrm{f}} = 2+1+1$ second generation MILC gauge configurations including up/down, strange, and charm HISQ quarks in the sea. In order to extract form factors for mesons including a physically massive b quark the so-called *heavy-HISQ* method was used. This framework involves using a heavy quark, h, in place of the b, and varying the mass of h from close to the charm quark mass all the way up to the physical b quark mass. By using multiple lattices with different lattice spacings this procedure allows us to map out discretization effects and the physical dependence on the h quark mass in the quantities of interest and to extract precise values at the physical point where the h quark mass is equal to that of the b. The determination of the full set of $B_s \to D_s^*$ form factors allowed for a model-independent determination of V_{cb} [23], using recent experimental results from LHCb [25].

The Fermilab lattice and MILC collaborations have recently also published first results for $B \to D^*$ form factors away from zero recoil [26], with lattice data extending across $\approx 1/3$ the full kinematic range of the decay, using the Fermilab action [27] for b and c quarks and using gluon field configurations with $n_f = 2+1$ flavors of asqtad sea quarks. They found, using the recent untagged data from Belle [21] and synthetic data from *BABAR* [28], $|V_{cb}| = 38.40(66)_{\mathrm{th}}(34)_{\mathrm{exp}} \times 10^{-3}$, in tension at the level of $\approx 4\sigma$ with the most recent inclusive determinations, and confirming the persistent tension currently seen in global averages [10]. The JLQCD collaboration has also presented preliminary results for the $B \to D^*$ form factors [29,30]. Note that these lattice results have been used in combination with unitarity constraints via the "dispersive matrix" method to extend these form factors across the kinematic range. Those studies found values of V_{cb} closer to the inclusive result [31].

Semileptonic decays of mesons also allow us to search directly for violations of the universality of the SM coupling between leptons and W bosons, as might result from new physics (NP) beyond the Standard Model. The most common method by which this is done is to construct ratios of branching fractions to final states with different leptons. This results in the cancellation of the CKM matrix element factors, as well as a substantial cancellation of correlated uncertainties entering through the form factors. The ratio relevant for $B \to D^*$ is

$$R(D^*) = \frac{\Gamma(B \to D^* \tau \bar{\nu}_\tau)}{\Gamma(B \to D^* \mu \bar{\nu}_\mu)}. \tag{1}$$

The most precise theoretical determinations of $R(D^*)$ in the SM use fits to experimental data for $B \to D^* \mu \bar{\nu}_\mu$, together with the assumption that NP can only appear in the semitauonic mode, to pin down the three form factors needed for the light lepton case ($\ell = e, \mu$). Until recently, the remaining pseudoscalar form factor relevant for the case of the heavy τ lepton was determined using HQET inputs [19,20,32]. This approach results in a very precise theory prediction for $R(D^*) = 0.254(5)$ [10] in tension with the most recent experimental average, $R^{\mathrm{HFLAV}}(D^*) = 0.295(14)$ [10], at the level of 2.7σ. This tension increases to $\approx 3\sigma$ if $R(D)$ is included. However, more recent measurements from the *BABAR*, Belle, and LHCb collaborations are closer to the SM prediction [33–35].

Recently, the Fermilab-MILC collaboration presented a lattice-only determination of $R(D^*)$ as well as a determination using a joint fit to lattice and experimental data [26], resulting in values of $R(D^*) = 0.265(13)$ and $R(D^*) = 0.2483(13)$, respectively. The difference between these results, while only at the 1σ level, is surprising and makes clear the desirability of additional precise lattice-only determinations of $R(D^*)$, as well as direct comparisons of the shape of the differential rate between theory and experiment, where some tension was also seen in [26].

The ratio of Eq. (1) was also computed using lattice QCD for $B_s \to D_s^* \ell \bar{\nu}$ and $B_c \to J/\psi$ in [22,23], respectively. The former is of particular interest as the value computed there, $R(D_s^*) = 0.2490(69)$, is in agreement with the theory prediction for $R(D^*)$ using experimental data as input. The form factors for $B \to D^* \ell \bar{\nu}$ and $B_s \to D_s^* \ell \bar{\nu}$ are related by the change of spectator quark from up/down to strange, and the corresponding $SU(3)_{\text{flav}}$ symmetry breaking effects are expected to be small, at the level of $\approx 1\%$ [7]. As such, a simultaneous analysis of $B_s \to D_s^*$ and $B \to D^*$ is desirable in order to investigate the differences between the results presented in [23] and those in [26].

In addition to $R(D^*)$, there are other observables, such as the τ lepton polarization asymmetry, the forward-backward asymmetry and the D^* longitudinal polarization fraction. These are expected to be sensitive to NP [36] and theoretical predictions for these would be valuable for future measurements. They also provide further tests of $SU(3)_{\text{flav}}$ breaking, which is expected to be small [37] as for $R(D^*)$. The Belle collaboration has recently measured both the lepton polarization asymmetry [38] and the D^* longitudinal polarization fraction [39], both of which may be computed directly on the lattice without the need for inputs such as V_{cb}.

Until now, lattice calculations of form factors for pseudoscalar to vector decays have focused exclusively on those form factors needed to describe the decay within the SM. Specifically, these are the two axial-vector form factors, one vector form factor, and one pseudoscalar form factor. However, assuming left-handed neutrinos, there are two additional dimension-6, parity-conserving four-fermion operators which can appear in the effective Hamiltonion whose matrix elements between B and D^* states are nonzero. These are the tensor operators:

$$\begin{aligned} &(\bar{c}\sigma_{\mu\nu} b)(\bar{\ell}_R \sigma^{\mu\nu} \nu_L) \\ &(\bar{c}\sigma_{\mu\nu}\gamma_5 b)(\bar{\ell}_R \sigma^{\mu\nu} \nu_L). \end{aligned} \tag{2}$$

The form factors for pseudoscalar to vector decays for the quark currents $\bar{c}\sigma_{\mu\nu} b$ and $\bar{c}\sigma_{\mu\nu}\gamma_5 b$ have not previously been computed on the lattice, though the single form factor for the related $\bar{s}\sigma_{\mu\nu} b$ was computed for the rare decay $B_c \to D_s \ell^+ \ell^- (\nu\bar{\nu})$ in [40], as well as for $B \to K$ [41], using the *heavy-HISQ* method together with renormalization factors matching the lattice tensor currents to those in the continuum $\overline{\text{MS}}$ scheme, computed in [42] using an intermediate RI-SMOM scheme.

In this work, we build on previous *heavy-HISQ* calculations of pseudoscalar to vector decays and compute both the SM and tensor form factors for $B \to D^*$. We also compute the SM and tensor form factors for $B_s \to D_s^*$, which we analyze simultaneously in order to better map out the dependence of the form factors on the spectator quark mass and in order to study $SU(3)_{\text{flav}}$ breaking effects between the two. We then give values for $|V_{cb}|$, $R(D^*)$ and other observables.

The remaining sections are organized as follows:

(i) In Sec. II we detail the theoretical framework relevant for semileptonic $B \to D^*$ decays, including the effective Hamiltonian, definitions of form factors and helicity amplitudes and expressions for the differential decay rate.

(ii) Section III contains the details of our lattice calculation, including our correlator fitting procedure, current renormalization, and how form factors are extracted from correlator fit results.

(iii) In Sec. IV we give the results of our lattice calculation and describe our chiral-continuum fit procedure including the heavy quark mass dependence. We give our results for the SM and tensor form factors and demonstrate the stability of our results to changes in correlator fits and changes to our chiral-continuum fit procedure.

(iv) In Sec. V we use our form factors to compute observables including $R(D^*)$. We compare our results to the recent measurement by Belle and determine a value of V_{cb}.

(v) Finally, in Sec. VI we summarize our findings and suggest directions for future investigations.

(vi) In Appendix A we compute expressions for the full differential decay rate including all operators relevant for NP. In Appendix B we discuss our approach to binning correlator data. In Appendix C we give the numerical results for the form factors on each ensemble, extracted from fits to correlation functions. In Appendix D we compute the next-to-leading order chiral logarithms, needed for the chiral-continuum extrapolation of the tensor form factors, using heavy-meson rooted staggered chiral perturbation theory. In Appendix E we compare the updated $B_s \to D_s^*$ form factor results of this work to those in [23].

II. THEORETICAL BACKGROUND

The effective Hamiltonian relevant for semileptonic $b \to c$ decays is, assuming left-handed neutrinos,

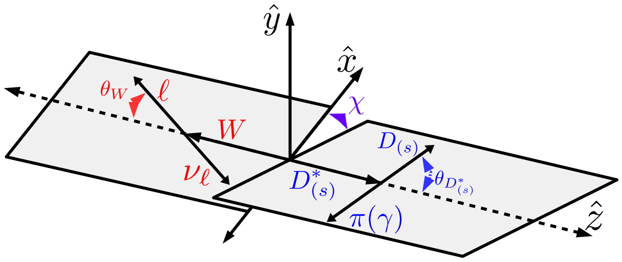

FIG. 1. Conventions for the angular variables entering the differential decay rate.

$$\begin{aligned}\mathcal{H}_{\rm eff} = \sqrt{2}G_F V_{cb}\big[&g_V\bar{c}\gamma_\mu b\bar{\ell}_L\gamma^\mu\nu_L + g_A\bar{c}\gamma_\mu\gamma_5 b\bar{\ell}_L\gamma^\mu\nu_L \\ &+ g_S\bar{c}b\bar{\ell}_R\nu_L + g_P\bar{c}\gamma_5 b\bar{\ell}_R\nu_L + g_T\bar{c}\sigma_{\mu\nu}b\bar{\ell}_R\sigma^{\mu\nu}\nu_L \\ &+ g_{T5}\bar{c}\sigma_{\mu\nu}\gamma^5 b\bar{\ell}_R\sigma^{\mu\nu}\nu_L + \text{H.c.}\big],\end{aligned} \tag{3}$$

where $\sigma_{\mu\nu} = i/2[\gamma_\mu,\gamma_\nu]$ and g_X are potentially complex coefficients. In the SM $g_T = g_{T5} = g_P = g_S = 0$ and $g_V = -g_A = 1$.

The differential decay rate to $D\pi\ell\bar{\nu}_\ell$ is, taking the D^* as a narrow resonance,

$$\frac{d\Gamma}{dq^2 d\cos(\theta_{D^*})d\cos(\theta_W)d\chi} = N(q^2)\sum_{\lambda_\ell}\Big|\sum_{\lambda_{D^*}}\mathcal{M}^{\lambda_{D^*}\lambda_\ell}\Big|^2, \tag{4}$$

where $N(q^2)$ is an overall kinematic factor

$$N(q^2) = \frac{3G_F^2|V_{cb}\eta_{\rm EW}|^2}{8(4\pi)^4}\frac{k(q^2-m_\ell^2)^2}{q^2M_B^2}\mathcal{B}(D^*\to D\pi) \tag{5}$$

and the angular variables are defined in Fig. 1.

The right-hand side of Eq. (4) is conventionally expressed in terms of helicity amplitudes, which are related to the form factors that parametrize the nonperturbative matrix elements of the quark currents in Eq. (3). The form factors, h_Y, for $B\to D^*$ are defined in the HQET basis as [43]

$$\begin{aligned}\langle D^*|\bar{c}b|\bar{B}\rangle &= 0, \\ \langle D^*|\bar{c}\gamma^5 b|\bar{B}\rangle &= -\sqrt{M_BM_{D^*}}(\epsilon^*\cdot v)h_P, \\ \langle D^*|\bar{c}\gamma^\mu b|\bar{B}\rangle &= i\sqrt{M_BM_{D^*}}\varepsilon^{\mu\nu\alpha\beta}\epsilon^*_\nu v'_\alpha v_\beta h_V, \\ \langle D^*|\bar{c}\gamma^\mu\gamma^5 b|\bar{B}\rangle &= \sqrt{M_BM_{D^*}}[h_{A_1}(w+1)\epsilon^{*\mu} \\ &\quad - h_{A_2}(\epsilon^*\cdot v)v^\mu - h_{A_3}(\epsilon^*\cdot v)v'^\mu], \\ \langle D^*|\bar{c}\sigma^{\mu\nu}b|\bar{B}\rangle &= -\sqrt{M_BM_{D^*}}\varepsilon^{\mu\nu\alpha\beta}[h_{T_1}\epsilon^*_\alpha(v+v')_\beta \\ &\quad + h_{T_2}\epsilon^*_\alpha(v-v')_\beta + h_{T_3}(\epsilon^*\cdot v)v_\alpha v'_\beta],\end{aligned} \tag{6}$$

where $w = v'\cdot v$ and v' and v are the four velocities of the D^* and B, respectively. Note that the matrix element of $\bar{c}\sigma_{\mu\nu}\gamma^5 b$ is related to that of $\bar{c}\sigma_{\mu\nu}b$, since $\sigma_{\mu\nu}\gamma^5 = \frac{i}{2}\epsilon_{\mu\nu\alpha\beta}\sigma^{\alpha\beta}$. The tensor current is renormalized in the SM, and so the tensor form factors depend on the renormalization scale which for b decays is typically taken as $\mu = m_b^{\rm pole}$.

In terms of these form factors, the nonzero helicity amplitudes for the (axial-)vector currents are

$$\begin{aligned}H_\pm = &-g_A^*h_{A_1}\sqrt{M_BM_{D^*}}(1+w) \\ &\mp g_V^*h_V\sqrt{M_BM_{D^*}(w^2-1)}\end{aligned} \tag{7}$$

$$\begin{aligned}H_0 = &-g_A^*M_B(1+w)\sqrt{\frac{M_BM_{D^*}}{q^2}} \\ &\times[h_{A_1}(w-r)-(w-1)[h_{A_3}+rh_{A_2}]]\end{aligned} \tag{8}$$

$$\begin{aligned}H_t = &-g_A^*M_B\sqrt{\frac{M_BM_{D^*}(w^2-1)}{q^2}} \\ &\times[h_{A_1}(1+w)-h_{A_2}(1-wr)-h_{A_3}(w-r)],\end{aligned} \tag{9}$$

where $r = M_{D^*}/M_B$. Note that the complex conjugates of the coefficients g_X appear in the conjugate mode $B^0\to D^{*-}\ell^+\nu$ for the general complex g_X appearing in Eq. (3). Expressions for the tensor helicity amplitudes are given in Appendix A.

The squared matrix element entering the differential rate may be written as

$$\sum_{\lambda_\ell}\Big|\sum_{\lambda_{D^*}}\mathcal{M}^{\lambda_{D^*}\lambda_\ell}\Big|^2 = \sum_i k_i(\theta_W,\theta_{D^*},\chi)\mathcal{H}_i. \tag{10}$$

The combinations k_i and $\mathcal{H}_i$ are given in Table I for the charge conjugate mode, $B^0\to D^{*-}\ell^+\nu$, for the case where only g_A and g_V are nonzero. We have checked that this expression matches that given in [21]. Note that it also agrees with the expression for the $\ell^+\nu$ final state given in [44], though there one must also take $H_+\leftrightarrow H_-$ for the conjugate hadronic current.

The construction of the full differential rate including tensor, axial-tensor, and pseudoscalar currents is described in Appendix A, together with the combinations k_i and $\mathcal{H}_i$. The explicit coefficients for the full and partially integrated differential rate are also provided as a supplementary PYTHON script for the general case of complex g_X.

III. LATTICE CALCULATION

Our lattice QCD calculation of the $B\to D^*$ form factors follows broadly the same heavy-HISQ approach as those presented in [23,45] for the related $B_s\to D_s^*$ and $B_c\to J/\psi$ form factors, respectively. We use a range of masses for a heavy quark, h, between the charm and physical bottom quark mass. The heavy-light pseudoscalar meson, which we will refer to as H, is at rest on the lattice. We give momentum to the charm quark using twisted boundary conditions so that the D^* covers the range of physical

TABLE I. The helicity amplitude combinations and coefficients for them that appear in Eq. (10) for $B^0 \to D^{*-}\ell^+\nu$ when only g_A and g_V in Eq. (3) are nonzero.

i	$\mathcal{H}_i$	$k_i(\theta_W, \theta_{D^*}, \chi)$
1	$\lvert H_+(q^2)\rvert^2$	$(1-\cos(\theta_W))^2(\sin^2(\theta_{D_s^*}))$
2	$\lvert H_-(q^2)\rvert^2$	$(1+\cos(\theta_W))^2(\sin^2(\theta_{D_s^*}))$
3	$\lvert H_0\rvert^2$	$4\sin^2(\theta_W)\cos^2(\theta_{D_s^*})$
4	$\mathrm{Re}(H_+H_0^*)$	$-2\sin(\theta_W)\sin(2\theta_{D_s^*})\cos(\chi)(1-\cos(\theta_W))$
5	$\mathrm{Re}(H_-H_0^*)$	$2\sin(\theta_W)\sin(2\theta_{D_s^*})\cos(\chi)(1+\cos(\theta_W))$
6	$\mathrm{Re}(H_+H_-^*)$	$-2\sin^2(\theta_W)\sin^2(\theta_{D_s^*})\cos(2\chi)$
7	$\frac{m_\ell^2}{q^2}\lvert H_+(q^2)\rvert^2$	$\sin^2(\theta_W)\sin^2(\theta_{D_s^*})$
8	$\frac{m_\ell^2}{q^2}\lvert H_-(q^2)\rvert^2$	$\sin^2(\theta_W)\sin^2(\theta_{D_s^*})$
9	$\frac{m_\ell^2}{q^2}\lvert H_0\rvert^2$	$4\cos^2(\theta_W)\cos^2(\theta_{D_s^*})$
10	$\frac{m_\ell^2}{q^2}\lvert H_t(q^2)\rvert^2$	$4\cos^2(\theta_{D_s^*})$
11	$\frac{m_\ell^2}{q^2}\mathrm{Re}(H_+H_0^*)$	$-2\sin(\theta_W)\sin(2\theta_{D_s^*})\cos(\chi)\cos(\theta_W)$
12	$\frac{m_\ell^2}{q^2}\mathrm{Re}(H_-H_0^*)$	$-2\sin(\theta_W)\sin(2\theta_{D_s^*})\cos(\chi)\cos(\theta_W)$
13	$\frac{m_\ell^2}{q^2}\mathrm{Re}(H_+H_-^*)$	$2\sin^2(\theta_W)\sin^2(\theta_{D_s^*})\cos(2\chi)$
14	$\frac{m_\ell^2}{q^2}\mathrm{Re}(H_tH_0^*)$	$-8\cos^2(\theta_{D_s^*})\cos(\theta_W)$
15	$\frac{m_\ell^2}{q^2}\mathrm{Re}(H_+H_t^*)$	$4\sin(\theta_W)\sin(2\theta_{D_s^*})\cos(\chi)$
16	$\frac{m_\ell^2}{q^2}\mathrm{Re}(H_-H_t^*)$	$4\sin(\theta_W)\sin(2\theta_{D_s^*})\cos(\chi)$

momenta for $H \to D^*$ decay. We use the HISQ action [24] for all valence quarks and use the second generation $N_f = 2+1+1$ MILC ensembles of gauge configurations, which include equal mass $(m_u = m_d)$ HISQ light quarks in the sea, as well as physically tuned strange and charm sea quarks [46,47]. We include ensembles with a range of lattice spacings from 0.09 fm down to 0.045 fm and a range of light quark masses. On the finest ensemble with 0.045 fm we are able to reach very close to the physical bottom quark mass for h. The details of these ensembles are given in Table II. Note that compared to [23,45] we include an additional ensemble, set 5, with $w_0/a = 3.0170(23)$ [48], which we refer to as "physical superfine." This additional ensemble is important, along with "physical fine" lattices, for resolving the logarithmic dependence of the form factors on the pion mass [49] arising from the proximity of the D^* to the $D^* \to D\pi$ threshold. The heavy quark masses used, together with the valence charm and strange quark masses (for the $B_s \to D_s^*$ case), are given in Table III. We use valence light quarks with masses equal to the sea light quark masses in Table II.

On the lattice, we compute two-point and three-point correlation functions of meson interpolating operators and currents in order to extract matrix elements, amplitudes, and energies. Note that in our lattice calculation the correlation functions are constructed from staggered

TABLE II. Details of the gauge field configurations used in our calculation [46,47]. We use the Wilson flow parameter [50], w_0, to fix the lattice spacing given in column 2. The physical value of w_0 was determined in [51] to be 0.1715(9) fm and the values of w_0/a, which are used together with w_0 to compute a, were taken from [8,52,53]. Set 1 with $w_0/a = 1.9006(20)$ is referred to as "fine," set 2 with $w_0/a = 2.896(6)$ as "superfine," set 3 with $w_0/a = 3.892(12)$ as "ultrafine", and set 4 with $w_0/a = 1.9518(7)$ as "physical fine." Note that compared to [23,45] we include an additional ensemble, set 5, with $w_0/a = 3.0170(23)$ [48], which we refer to as "physical superfine," that includes physical light quarks. n_{cfg} and n_{t} give the number of configurations and the number of time sources, respectively. am_{l0}, am_{s0}, and am_{c0} are the masses of the sea up/down, strange, and charm quarks in lattice units. We also include the approximate mass of the Goldstone pion, computed in [2].

Set	a (fm)	$N_x \times N_t$	am_{l0}	am_{s0}	am_{c0}	M_π (MeV)	$n_{\mathrm{cfg}} \times n_{\mathrm{t}}$
1	0.0902	32×96	0.0074	0.037	0.440	316	1000×16
2	0.0592	48×144	0.0048	0.024	0.286	329	500×4
3	0.0441	64×192	0.00316	0.0158	0.188	315	375×4
4	0.0879	64×96	0.0012	0.0363	0.432	129	600×8
5	0.0568	96×192	0.0008	0.022	0.260	135	100×4

TABLE III. Details of the strange, charm, and heavy valence masses.

Set	am_h^{val}	am_s^{val}	am_c^{val}
1	0.65, 0.725, 0.8	0.0376	0.449
2	0.427, 0.525, 0.65, 0.8	0.0234	0.274
3	0.5, 0.65, 0.8	0.0219	0.194
4	0.65, 0.725, 0.8	0.036	0.433
5	0.427, 0.525, 0.65, 0.8	0.0165	0.2585

TABLE IV. Values of twists, θ, together with values of T used in the three-point functions in Eq. (11). Note that we use a momentum direction $\vec{p}\,' = (k, k, 0)$ with $ak = \theta\pi/N_x$.

Set	θ	T/a
1	0.0, 0.3859, 0.7718, 1.1577, 1.5436, 1.9295	14,17,20
2	0.0, 0.8464, 1.6929, 2.5393, 3.3857, 4.2322	22,25,28
3	0.0, 1.2596, 2.5192, 3.7788, 5.0384, 6.2981	31,36,41
4	0.0, 0.7672, 1.5343, 2.3015, 3.0687, 3.8358	14,17,20
5	0.0, 1.6929, 3.3857, 5.0786, 6.7715, 8.4643	22,25,28

spin-taste operators [24]. In this section, for notational simplicity, we write the correlation functions in terms of the equivalent continuum operators built from Dirac fermions. For a general current operator $\bar{c}\Gamma h$, the two-point and three-point correlation functions take the form

$$\begin{aligned}
C_{\mathrm{2pt}}^{D_l^*}(t,0) &= \langle 0|\bar{l}\gamma^\nu c(t)(\bar{l}\gamma^\nu c(0))^\dagger|0\rangle,\\
C_{\mathrm{2pt}}^{H_l}(t,0) &= \langle 0|(\bar{h}\gamma^5 l(t))^\dagger \bar{h}\gamma^5 l(0)|0\rangle,\\
C_{\mathrm{3pt}}(T,t,0) &= \langle 0|\bar{l}\gamma^\nu c(T)\bar{c}\Gamma h(t)\bar{h}\gamma^5 l(0)|0\rangle. \qquad (11)
\end{aligned}$$

We compute correlation functions for both $l = u/d$ and $l = s$, and we will distinguish the mesons with $l = s$ with a subscript s. We use random wall sources at time t_{src} for the light and charm quark propagators in order to improve statistics, as well as for the heavy quarks entering the two-point functions, and we use twisted boundary conditions [54,55] to give momentum to the charm quark. We use the light quark propagator at time $t_{\mathrm{src}} - T$ to construct the source for the heavy quark propagator needed for the three-point correlation functions. Finally, this heavy quark propagator is tied together with the charm propagator at time $t_{\mathrm{src}} - T + t$ to form the three-point correlation function. The arrangement of quark propagators entering the three-point functions is shown in Fig. 2. We compute three-point correlation functions using multiple values of T in order to resolve the T dependence of the correlation functions. The values of T used on each ensemble, together with the twists used to give momentum to the charm quarks, are given in Table IV. Note that the twists differ slightly from those used in [23].

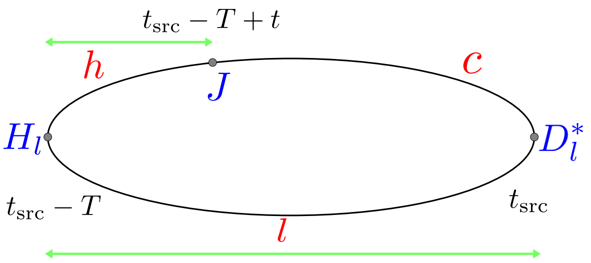

FIG. 2. Arrangement of propagators in the three-point function; we refer to c as the "active" charm quark, h as the "extended" heavy quark, and l as the "spectator" light/strange quark. J represents the insertion of either a vector, axial-vector, or tensor current, and H_l and D_l^* represent the insertion of the corresponding meson interpolating operators.

A. Correlator fits

We fit the correlation functions in Eq. (11) to exponentials, including time-oscillating terms as is typical when using staggered quarks [22–24,41,56]:

$$\begin{aligned}
C_{\mathrm{2pt}}^{D_s^*}(t,0) &= \sum_i \left((A_n^i)^2 e^{-tE_n^i} + (-1)^t (A_o^i)^2 e^{-tE_o^i}\right),\\
C_{\mathrm{2pt}}^{H_s}(t,0) &= \sum_i \left((B_n^i)^2 e^{-tM_n^i} + (-1)^t (B_o^i)^2 e^{-tM_o^i}\right) \qquad (12)
\end{aligned}$$

and

$$\begin{aligned}
C_{\mathrm{3pt}}(T,t,0) = \sum_{i,j} \Big(& A_n^i B_n^j J_{nn}^{ij} e^{-(T-t)E_n^i - tM_n^j}\\
& + (-1)^{T-t} A_o^i B_n^j J_{\mathrm{on}}^{ij} e^{-(T-t)E_o^i - tM_n^j}\\
& + (-1)^t A_n^i B_o^j J_{no}^{ij} e^{-(T-t)E_n^i - tM_o^j}\\
& + (-1)^T A_o^i B_o^j J_{oo}^{ij} e^{-(T-t)E_o^i - tM_o^j} \Big). \qquad (13)
\end{aligned}$$

Here i and j are integers corresponding to on-shell particle states of increasing energies, A^i and B^i are the amplitudes (together with relativistic normalization factors) of the $D_{(s)}^*$ and $H_{(s)}$ operators, respectively, and E_i and M_i are their energies and masses. The time-oscillating terms, with subscript "o" are a consequence of the use of staggered quarks; since our interpolating operators are only projected onto definite spatial momentum they may couple to "time doubled" states. The subscript n indicates nonoscillating states. J_{nn}^{ij} is then related to the matrix element of the current $\bar{c}\Gamma h(t)$ in Eq. (11) between the nonoscillating states labeled i and j. The ground state parameters are related to matrix elements as

$$\begin{aligned}
A_n^0 &= \frac{N_{D_{(s)}^*}}{\sqrt{2E_{D_{(s)}^*}}}\left(1 + \frac{\vec{p}_\nu^{\,\prime 2}}{M_{D_{(s)}^*}^2}\right)^{1/2},\\
B_n^0 &= \frac{N_{H_{(s)}}}{\sqrt{2M_{H_{(s)}}}}, \qquad (14)
\end{aligned}$$

where

$$\begin{aligned} \langle 0|\bar{l}\gamma^\nu c|D^*_{(s)}(p',\lambda)\rangle &= N_{D^*_{(s)}}\epsilon^\nu(p',\lambda), \\ \langle H_{(s)}(p)|\bar{h}\gamma^5 c|0\rangle\rangle &= N_{H_{(s)}}. \end{aligned} \tag{15}$$

$$J^{00}_{nn(\nu,\Gamma)} = \sum_\lambda \frac{\epsilon^\nu(p',\lambda)\langle D^*_{(s)}(p',\lambda)|\bar{c}\Gamma h|H_{(s)}\rangle}{\sqrt{2E_{D^*_{(s)}}2M_{H_{(s)}}\left(1+\vec{p}_\nu'^2/M^2_{D^*_{(s)}}\right)}}, \tag{16}$$

where $\vec{p}'_\nu$ is the ν component of the $D^*_{(s)}$ spatial momentum, with ν corresponding to the choice of polarization in Eq. (11), with current $\bar{c}\Gamma h$.

B. Extracting form factors

In order to extract the form factors from our correlator fits, we must use appropriate combinations of $D^*_{(s)}$ momentum, p', four-vector component, ν, and current Dirac matrix, Γ, when computing correlation functions. These combinations must produce matrix elements corresponding to linearly independent combinations of form factors. In order to isolate h_V and $h_{A_{1,2,3}}$ on each ensemble for each combination of q^2 and am_h we use the same combinations of ν and Γ as described in [22,23]. We give the relation of these matrix elements to the form factors below. We work with the H at rest throughout.

1. Vector and axial-vector form factors

As in [22,23] we define Φ_ν, corresponding to the denominator in the right-hand side of Eq. (16):

$$\Phi_\nu = \sqrt{2E_{D^*}2M_H(1+\vec{p}_\nu'^2/M^2_{D^*})}. \tag{17}$$

With this definition, together with Eq. (6) and the completeness relation for the D^* polarization vectors $\sum_\lambda \epsilon^\mu\epsilon^{\nu*} = -g^{\mu\nu} + v'^\mu v'^\nu$, we have for the combinations listed in Table V

$$\begin{aligned} \tilde{J}^{00}_{nn(1,\gamma^3)} &= ih_V\tilde{k}, \\ \tilde{J}^{00}_{nn(1,\gamma^5)} &= \frac{M_H w\tilde{k}}{m_h+m_c}\big(h_{A_1}(w+1) \\ &\quad - h_{A_2}(1-rw) - h_{A_3}(w-r)\big), \\ \tilde{J}^{00}_{nn(3,\gamma^3\gamma^5)} &= (1+w)h_{A_1}, \\ \tilde{J}^{00}_{nn(1,\gamma^1\gamma^5)} &= h_{A_1}(w+1)(1+\tilde{k}^2) - wh_{A_3}\tilde{k}^2, \end{aligned} \tag{18}$$

where we have defined the reduced combination $\tilde{J}^{00}_{nn(\nu,\Gamma)} = J^{00}_{nn(\nu,\Gamma)}\Phi_\nu/\sqrt{M_{H_{(s)}}M_{D^*_{(s)}}}$, $\tilde{k} = k/M_{D^*}$ and where $\vec{p}_{D^*} = \vec{p}' = (k,k,0)$. Note that when converting between form factors and matrix elements, we use the masses obtained from the local spin-taste operators for the $D^*_{(s)}$ and $H_{(s)}$. Discretization effects resulting from this choice only enter at the level of the taste splittings, which for heavy-light mesons using HISQ quarks are very small [24,47], and will be consistently included in our chiral-continuum extrapolation along with other discretization effects.

TABLE V. Spin-taste operators used to isolate the SM form factors, $h_{V,A_{1,2,3}}$. The first column is the operator used for the $H_{(s)}$, the second for the $D^*_{(s)}$ and the third column is the operator used at the current.

	$\mathcal{O}_{H_{(s)}}$	$\mathcal{O}_{D^*_{(s)}}$	$\mathcal{O}_J$
$\tilde{J}^{00}_{nn(1,\gamma^3)}$	$\gamma_0\gamma_5\otimes\gamma_0\gamma_5$	$\gamma_1\otimes\gamma_1\gamma_2$	$\gamma_3\otimes\gamma_3$
$\tilde{J}^{00}_{nn(1,\gamma^5)}$	$\gamma_5\otimes\gamma_5$	$\gamma_1\otimes 1$	$\gamma_5\otimes\gamma_5$
$\tilde{J}^{00}_{nn(3,\gamma^3\gamma^5)}$	$\gamma_5\otimes\gamma_5$	$\gamma_3\otimes\gamma_3$	$\gamma_3\gamma_5\otimes\gamma_3\gamma_5$
$\tilde{J}^{00}_{nn(1,\gamma^1\gamma^5)}$	$\gamma_5\otimes\gamma_5$	$\gamma_1\otimes\gamma_1$	$\gamma_1\gamma_5\otimes\gamma_1\gamma_5$

2. Tensor form factors

We now proceed to detail the procedure adopted here for isolating the tensor form factors. For the tensor current the sum over D^* polarizations in Eq. (16) gives

$$\begin{aligned} \tilde{J}^{00}_{nn(\kappa,\sigma^{\mu\nu})} &= \varepsilon^{\mu\nu\alpha\beta}[h_{T_1}(\delta^\kappa_\alpha - v'^\kappa v'_\alpha)(v+v')_\beta \\ &\quad + h_{T_2}(\delta^\kappa_\alpha - v'^\kappa v'_\alpha)(v-v')_\beta \\ &\quad + h_{T_3}(v^\kappa - wv'^\kappa)v_\alpha v'_\beta]. \end{aligned} \tag{19}$$

We choose combinations of Lorentz indices for the tensor current and $D^*_{(s)}$ operator, $\mu\nu = 12$ and $\kappa = 3$, $\mu\nu = 14$ and $\kappa = 3$, $\mu\nu = 23$ and $\kappa = 1$. These choices give

$$\begin{aligned} \tilde{J}^{00}_{nn(3,\sigma^{12})} &= h_{T_1}(1+w) + h_{T_2}(1-w), \\ \tilde{J}^{00}_{nn(3,\sigma^{14})} &= \tilde{k}(h_{T_1} - h_{T_2}), \\ \tilde{J}^{00}_{nn(1,\sigma^{23})} &= h_{T_1}(1+w+\tilde{k}^2) + h_{T_2}(1-w+\tilde{k}^2) - h_{T_3}w\tilde{k}^2. \end{aligned} \tag{20}$$

TABLE VI. Spin-taste operators used to isolate the tensor form factors $h_{T_{1,2,3}}$. The first column is the operator used for the $H_{(s)}$, the second for the $D^*_{(s)}$ and the third column is the operator used at the current.

	$\mathcal{O}_{H_s}$	$\mathcal{O}_{D^*_s}$	$\mathcal{O}_J$
$\tilde{J}^{00}_{nn(3,\sigma^{12})}$	$\gamma_0\gamma_5\otimes\gamma_0\gamma_5$	$\gamma_3\otimes\gamma_3$	$\gamma_1\gamma_2\otimes\gamma_1\gamma_2$
$\tilde{J}^{00}_{nn(3,\sigma^{14})}$	$\gamma_5\otimes\gamma_5$	$\gamma_3\otimes\gamma_2\gamma_3$	$\gamma_0\gamma_1\otimes\gamma_0\gamma_1$
$\tilde{J}^{00}_{nn(1,\sigma^{23})}$	$\gamma_0\gamma_5\otimes\gamma_0\gamma_5$	$\gamma_1\otimes\gamma_1$	$\gamma_2\gamma_3\otimes\gamma_2\gamma_3$

TABLE VII. Z factors from [8,9] for the axial-vector and vector operators used in this work, together with the discretization corrections. Z^A and Z^V values for $am_h = 0.725$ on set 1 and $am_h = 0.65$ on set 4 were obtained by interpolation from the other values for those sets. The total renormalization factor is given by $Z^{A(V)}Z^{\mathrm{disc}}$.

Set	am_h	Z^A	Z^V	Z^{disc}
1	0.65	1.03740(58)	1.0254(35)	0.99635
	0.725	1.04030(58)	1.0309(35)	0.99491
	0.8	1.04367(56)	1.0372(32)	0.99306
2	0.427	1.0141(12)	1.0025(31)	0.99931
	0.525	1.0172(12)	1.0059(33)	0.99859
	0.65	1.0214(12)	1.0116(37)	0.99697
	0.8	1.0275(12)	1.0204(46)	0.99367
3	0.5	1.00896(44)	1.0029(38)	0.99889
	0.65	1.01363(49)	1.0081(43)	0.99704
	0.8	1.01968(55)	1.0150(49)	0.99375
4	0.65	1.03717(47)	1.0229(29)	0.99645
	0.725	1.04037(47)	1.0285(29)	0.995
	0.8	1.04390(39)	1.0348(29)	0.99315
5	0.427	1.014(10)	1.002(10)	0.99931
	0.525	1.017(10)	1.006(11)	0.99859
	0.65	1.021(10)	1.012(11)	0.99697
	0.8	1.028(10)	1.020(11)	0.99367

3. Spin-taste operators

We implement the meson interpolator and current operators as staggered spin-taste operators. The combinations of spin-taste operators we use are given in Tables V and VI. These have been chosen so that the current operator is the local one for which the renormalization factors were computed.

C. Current renormalization

The lattice currents used require renormalization factors to match them to the continuum operators, and for the tensor current, we match to the $\overline{\mathrm{MS}}$ scheme. The axial-vector and vector current pieces, Z_A and Z_V respectively, are given in Table VII. These were computed in [8,9] for sets 1, 2, 3, and 4. On set 5, we use the values from set 2, adding a conservative 1.0% uncertainty motivated by the observed maximum change between sets 1 and 4 for a somewhat smaller difference in lattice spacings. The Z^A and Z^V values for $am_h = 0.725$ on set 1 and $am_h = 0.65$ on set 4 were obtained by interpolation from the other values for those sets, using the largest uncertainty of the other factors on that set. The tensor renormalization factors, Z_T, were computed using an intermediate RI-SMOM scheme in [42]. We use the factors computed at an intermediate scale of $\mu = 2$ GeV, and then run to $\mu = 4.8\ \mathrm{GeV} \sim m_b^{\mathrm{pole}}$, with the condensate correction applied. Since we are only interested in the $m_h = m_b$ point, we use $Z_T(4.8\ \mathrm{GeV})$ on each lattice, rather than trying to estimate a value of m_h^{pole} to run Z_T for each m_h.

TABLE VIII. $Z_T(\mu = 4.8\ \mathrm{GeV})$ factors from [42] for the tensor operators used in this work.

Set	Z_T
1	1.0029(43)
2	1.0342(43)
3	1.0476(42)
4	1.0029(43)
5	1.0342(43)

The values of Z_T are given in Table VIII. Note that the tensor renormalization factors were defined in the limit that the valence masses in lattice units are taken to zero, and as such are independent of am_h.

D. Correlator fit parameters

We perform correlator fits of our lattice data to Eqs. (12) and (13) using the CORRFITTER PYTHON package [57]. Our fits are done to all correlation functions simultaneously.

The prior values and uncertainties of the fit parameters that we use here are very similar to those used in [23], with only small differences in the heuristic forms chosen for the m_h dependance of $M_{H_{(s)}}$ and $M_{D^*_{(s)}}$. For ground-state priors we take $E_0^{D^*_{(s)}} = \sqrt{M^2_{D^*_{(s)}} + 2k^2} \times 1(0.3)$ GeV and $M_0^{H_{(s)}} = (M^{H_s}_{\mathrm{max}} + m_h - 0.8) \times 1(0.3)$ GeV. Here we use $M_{D^*_s} = M_{D^*} + m_s$, where m_s is the mass in GeV of the valence strange quark given in Table III. For $M^{H_s}_{\mathrm{max}}$ we use the value of M_{H_s} from [8] corresponding to the largest value of $am_h = 0.8$. Note that our priors for H and H_s masses have the same central value and uncertainty, and we use separate priors with equal central values and uncertainties for the energies and amplitudes of meson operators in different taste multiplets. Our priors for the lowest oscillating state energies, as well as amplitudes, are given in Table IX. For the matrix elements, $J^{ij}_{n(o)n(o)}$, we take priors 0(1) for all except those proportional to ak. For these, we first divide by ak before fitting, since ak is known exactly from the twists (Table IV). We increase the uncertainty on the corresponding priors for the oscillating state matrix

TABLE IX. Correlator fit priors. We take $\Delta E_i^{(o)} = \Lambda_{\mathrm{QCD}} \times 1.0(0.75)$ where $\Delta E_i^{(o)} = E_{i+1}^{(o)} - E_i^{(o)}, i \geq 0$ and here for our correlator fits we take $\Lambda_{\mathrm{QCD}} = 0.75$ GeV. In the Table we have defined $\Omega_{H_{(s)}} = M^{H_s}_{\mathrm{max}} + m_h - 0.8$ and $\Omega_{D^*_{(s)}} = \sqrt{M^2_{D^*_{(s)}} + 2k^2}$ following the relativistic dispersion relation.

Prior	$D^*_{(s)}(k)$	H_s
E_n^0/GeV	$\Omega_{D^*_{(s)}} \times 1.0(0.3)$	$\Omega_{H_{(s)}} \times 1(0.3)$
E_o^0/GeV	$\Omega_{D^*_{(s)}} \times 1.2(0.5)$	$\Omega_{H_{(s)}} \times 1.2(0.5)$
$A(B)_i^{n(o)}$	0.1(5.0)	0.1(5.0)

TABLE X. Details of fit parameters. ΔT indicates the number of data points at the extremities of correlation functions not included in the fit, and n_{exp} is the number of nonoscillating and time-oscillating exponentials included in our correlator fits to Eqs. (12) and (13). $\chi^2/\mathrm{d.o.f.}$ is estimated by introducing SVD and prior noise as in [57]. We use the fit parameters in bold for our subsequent analysis. δ is a label for the other fits that we will use later in Sec. IV C to investigate the sensitivity of our final results to these parameters.

Set	n_{exp}	$\Delta T_{3\mathrm{pt}}$	$\Delta T_{2\mathrm{pt}}^{D^*_{(s)}}$	$\Delta T_{2\mathrm{pt}}^{H_{(s)}}$	SVD cut	$\chi^2/\mathrm{d.o.f.}$	δ
1	**3**	**2**	**4**	**4**	**0.005**	**1.02**	0
	3	3	6	6	0.005	0.99	1
	3	2	4	4	0.001	1.04	2
2	**3**	**4**	**9**	**9**	**0.005**	**1.01**	0
	3	4	9	9	0.001	1.05	1
	3	4	8	8	0.005	1.04	2
3	**3**	**6**	**12**	**12**	**0.001**	**1.01**	0
	3	5	11	11	0.001	1.02	1
	3	6	12	12	0.0005	1.07	2
4	**3**	**2**	**4**	**4**	**0.01**	**1.02**	0
	3	2	5	5	0.01	1.03	1
	3	2	4	4	0.005	1.02	2
5	**3**	**5**	**10**	**10**	**0.001**	**1.1**	0
	3	5	10	10	0.005	1.1	1
	3	4	8	8	0.001	1.1	2

TABLE XI. D^* masses for the local spin-taste operator $\gamma_1 \otimes \gamma_1$ and one-link operators $\gamma_1 \otimes 1$ and $\gamma_1 \otimes \gamma_1\gamma_2$ used in our calculation, see Tables V and VI.

	aM_{D^*}		
Set	$\gamma_1 \otimes \gamma_1$	$\gamma_1 \otimes 1$	$\gamma_1 \otimes \gamma_1\gamma_2$
1	0.9289(26)	0.9292(31)	0.9277(34)
2	0.6110(25)	0.6110(36)	0.6108(37)
3	0.4556(14)	0.4536(21)	0.4551(18)
4	0.8949(42)	0.8954(53)	0.8953(49)
5	0.5829(49)	0.5823(73)	0.5790(75)

TABLE XII. D_s^* masses for the local spin-taste operator $\gamma_1 \otimes \gamma_1$ and one-link operators $\gamma_1 \otimes 1$ and $\gamma_1 \otimes \gamma_1\gamma_2$ used in our calculation, see Tables V and VI.

	$aM_{D_s^*}$		
Set	$\gamma_1 \otimes \gamma_1$	$\gamma_1 \otimes 1$	$\gamma_1 \otimes \gamma_1\gamma_2$
1	0.96499(76)	0.9649(11)	0.9644(13)
2	0.6349(12)	0.6348(15)	0.6346(16)
3	0.47183(68)	0.47155(85)	0.47202(75)
4	0.93970(62)	0.93952(91)	0.93964(93)
5	0.6075(12)	0.6084(13)	0.6078(13)

elements J^{ij}_{no}, J^{ij}_{oo}, and J^{ij}_{oo} by a factor of 4 relative to J^{ij}_{nn} to account for this rescaling, and take priors of 0(4).

In order to fit our data simultaneously, it is necessary to implement an singular value decomposition (SVD) cut (see Appendix D of [58]). The size of the SVD cut used on each lattice was chosen based on the values used in [23], though note that by omitting the highly correlated η_c and η_h correlator data, as well as by only partially binning over time sources as discussed in Appendix B, we are able to use smaller SVD cuts, resulting in more stable fits. We also omit correlator data points close to the source and sink operators that contain significant excited state contamination. These data points are not included when computing correlations, further helping to improve resolution of the covariance matrix for the correlator data and reducing the size of the required SVD cut. The number of data points excluded from close to the source and sink operators are given in Table X, together with the number of exponentials included in Eqs. (12) and (13). Table X also includes the value of $\chi^2/\mathrm{d.o.f.}$ estimated using prior and SVD noise as in [57], following [22,23]. In Sec. IV C we investigate the effect of using different combinations the fit parameters in Table X. We find that our results are very stable to changes in ΔT and the choice of SVD cut.

IV. RESULTS

In this section we give the numerical results from the correlator fits described in Sec. III A. We then describe our extrapolation of the form factors to the physical-continuum point. We demonstrate that our physical-continuum form factors are insensitive to reasonable changes to our fitting and extrapolation procedure, then we provide a breakdown of the sources of uncertainty entering the form factors across the kinematic range of the decay.

A. Correlator fit results

The ground state D^* and D_s^* masses resulting from our correlator fits are given in Tables XI and XII, where we see some changes compared to [23] on set 3 on the order of $\approx 1.5\sigma$. Such changes are not surprising, and are a result of the exclusion of highly correlated η_c data, as well as the inclusion of additional D_s^* polarizations and D^* data, together with the improved resolution of the covariance matrix as discussed in Appendix B. We note that our fit results for the D_s^* masses on set 3 are in good agreement with those given in [9], which included a much smaller set of correlators and so had better resolution of the data covariance matrix. The $H_{(s)}$ masses are given in Table XIII in lattice units, where we see good agreement with those in [9,23].

The full set of numerical results for the SM form factors for $B \to D^*$ are given in Tables XIX–XXIII and in Tables XXIX–XXXIII for $B_s \to D_s^*$ in Appendix C. There, the tensor form factors for $B \to D^*$ are also given in Tables XXIV–XXVIII and in Tables XXXIV–XXXVIII for $B_s \to D_s^*$. Note that h_{T_3} is particularly noisy, owing to the factor of k^2 appearing in Eq. (20). These data points are

TABLE XIII. $H_{(s)}$ masses for the local spin-taste operators $\gamma_5 \otimes \gamma_5$ and $\gamma_0\gamma_5 \otimes \gamma_0\gamma_5$ that we use in our calculation, see Tables V and VI.

		$\gamma_5 \otimes \gamma_5$		$\gamma_0\gamma_5 \otimes \gamma_0\gamma_5$	
Set	am_h	aM_H	aM_{H_s}	aM_H	aM_{H_s}
1	0.65	1.08972(80)	1.12504(26)	1.0894(13)	1.12556(46)
	0.725	1.16928(88)	1.20424(28)	1.1689(14)	1.20472(48)
	0.8	1.24659(95)	1.28127(29)	1.2462(15)	1.28172(50)
2	0.427	0.7510(13)	0.77418(55)	0.7499(22)	0.77410(70)
	0.525	0.8617(15)	0.88450(62)	0.8607(24)	0.88452(76)
	0.65	0.9969(18)	1.01962(71)	0.9962(26)	1.01976(84)
	0.8	1.1516(21)	1.17452(81)	1.1513(29)	1.17477(93)
3	0.5	0.78656(92)	0.80250(31)	0.7863(13)	0.80249(41)
	0.65	0.9482(11)	0.96383(38)	0.9479(15)	0.96372(50)
	0.8	1.1021(14)	1.11777(46)	1.1019(17)	1.11761(59)
4	0.65	1.0783(15)	1.12007(22)	1.0768(23)	1.12053(40)
	0.725	1.1578(16)	1.19923(23)	1.1564(24)	1.19966(43)
	0.8	1.2352(17)	1.27624(25)	1.2338(26)	1.27663(46)
5	0.427	0.7440(22)	0.76937(35)	0.7419(44)	0.76975(49)
	0.525	0.8548(27)	0.87950(44)	0.8527(48)	0.87994(58)
	0.65	0.9902(32)	1.01437(57)	0.9882(52)	1.01489(69)
	0.8	1.1452(37)	1.16898(74)	1.1435(56)	1.16958(82)

shown in Figs. 3 and 4, where we also show the $B \to D^*$ form factors extrapolated to the physical-continuum point.

B. Physical-continuum extrapolation

In order to determine the physical-continuum form factors we must fit our lattice form factor data to an appropriate function describing its kinematic and physical m_h dependence, as well as discretization effects and quark mass mistuning effects. At the physical-continuum point with $m_h = m_b$, the BGL parametrization is often used to describe the kinematic dependence of the form factors in the helicity basis, with the BGL coefficients guaranteed to be between -1 and 1 by unitarity constraints. However, the BGL parametrization (see Sec. IV E for details) depends on the masses of several mesons containing a b quark, as well as susceptibilities which also depend on the b quark mass and are computed perturbatively. This makes it impractical for our purposes to use it here, where we require our fit function to describe the m_h dependence of our form factors.

Instead we use a more straightforward power series in $(w-1)$, $(\Lambda_{\mathrm{QCD}}/m_h)$, and δ_{m_q} to parametrize the continuum HQET form factors. Using a power series in $(w-1)$ to describe the kinematic dependence of the form factors allows us to describe the physical m_h dependence away from the point $m_h = m_b$ as modifications to the coefficients. These appear as multiplicative corrections, in powers of $(\Lambda_{\mathrm{QCD}}/m_h)$ motivated by HQET. However, we must be careful to choose prior widths for our coefficients that do not overly constrain the shape of the form factors. In order to set our priors for the physical-continuum coefficient of each power of $(w-1)$, we make use of the physical-continuum BGL expansion [13] at $m_h = m_b$ where the masses and susceptibilities are well known. We can then compute each physical-continuum $(w-1)$ coefficient in terms of the physical-continuum BGL expansion coefficients, and use priors for the physical-continuum BGL coefficients directly, choosing prior widths motivated by the unitarity bounds.

To compute the physical-continuum $(w-1)$ coefficients of the HQET form factors, we start with the physical-continuum BGL parametrization of the helicity basis form factors at the $m_h = m_b$ point, which we then convert to the HQET basis. The BGL parametrization is given in terms of z, mapped from q^2 [see Eq. (33)]. We set $t_0 = q^2_{\mathrm{max}}$ in this mapping and then expand z, the Blaschke factors $P(z)$, and outer functions $\phi(z)$ appearing in the BGL expansion in powers of $(w-1)$. This provides a linear map, which we call $M^{\mathrm{BGL}\to\mathrm{HQET}}_{nm,YX}$, from the physical-continuum BGL coefficients for the helicity basis form factors, to each physical-continuum $(w-1)^n$ coefficient for the HQET form factors. Note that since the BGL expansion describes the form factors in the helicity basis, we must explicitly impose the kinematical constraints $F_1(w=1) = M_B(1-r)f(w=1)$ and $F_2(w_{\mathrm{max}}) = (1+r)/(M_B^2(1+w_{\mathrm{max}})(1-r)r)F_1(w_{\mathrm{max}})$ in order to convert to the HQET basis consistently. This is done by fixing the zeroth order BGL coefficient of F_1 and F_2 in terms of the remaining coefficients such that the constraints are satisfied. We follow the conventions for masses and resonances entering the BGL expansion given in [14], although we have checked that other choices do not significantly impact the mapping to $(w-1)$ coefficients. We

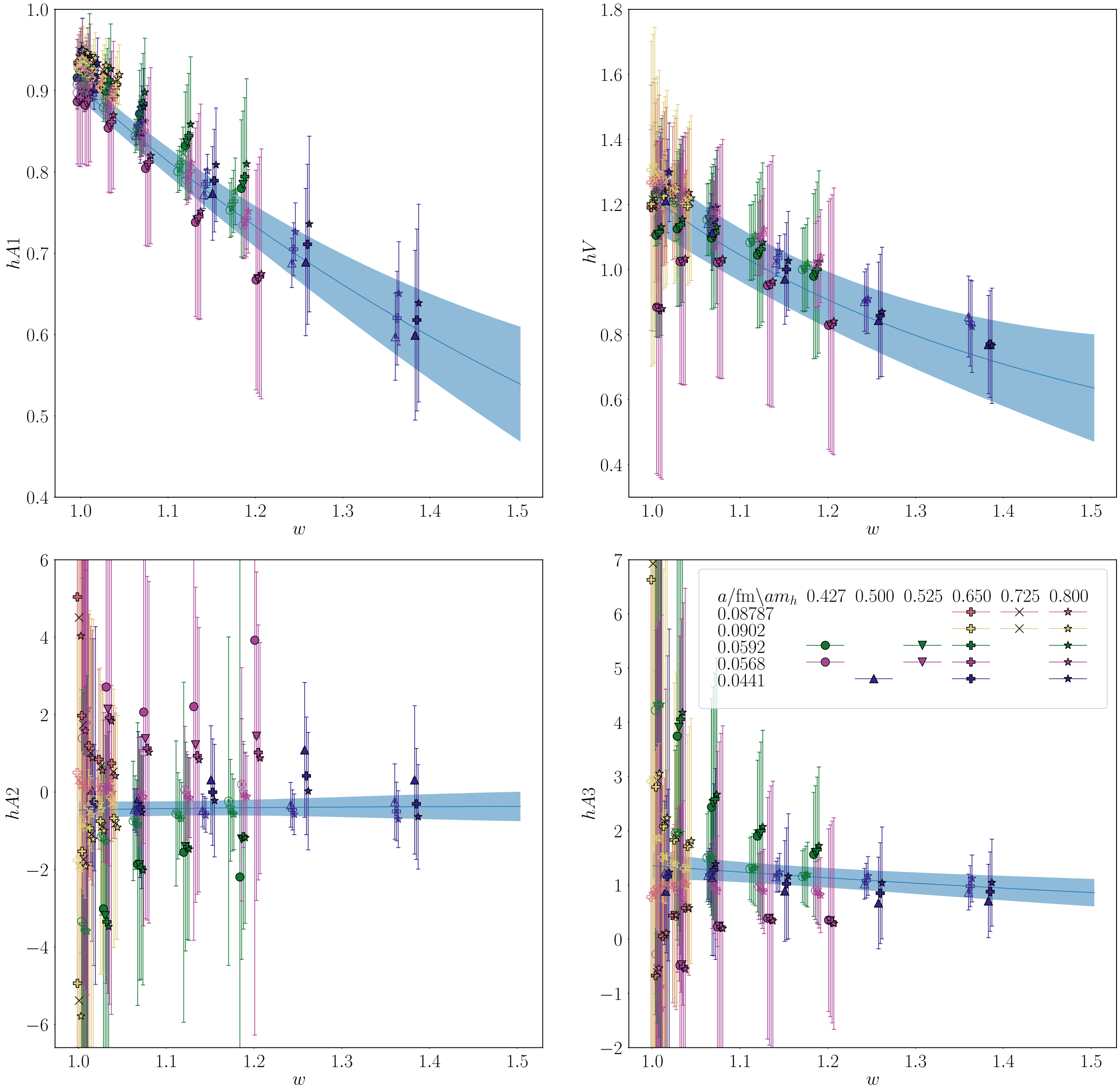

FIG. 3. The points show our lattice QCD results for each SM form factor as given in Tables XIX–XXIII for $B \to D^*$ (filled points) and Tables XXIX–XXXIII for $B_s \to D_s^*$ (empty points) as a function of the recoil parameter, w. The legend gives the mapping between symbol color and shape and the set of gluon field configurations used, as given by the lattice spacing, and the heavy quark mass in lattice units (see Tables II and III). The blue curve with error band is the result of our fit in the continuum limit and with the physical b quark mass for $B \to D^*$. Note that we include the data points for both the $B_s \to D_s^*$ and $B \to D^*$ form factors, and that for clarity data points at fixed w for different values of m_h are offset a small amount.

use Gaussian priors for the BGL coefficients of 0 ± 5, which are very conservative compared to the unitarity constraints which force them to be less than 1.

Since the z expansion converges quickly owing to the small size of z, we include only up to z^4 in the z expansion. When we look at the numerical values appearing in $M^{\mathrm{BGL}\to\mathrm{HQET}}_{nm,YX}$ we see that some are substantially greater than 1. For instance, the coefficient of $(w-1)^5$ for h_{A_1} includes a term $\approx -50a_0^{f\mathrm{BGL}}$, where $a_0^{f\mathrm{BGL}}$ is the leading (z^0) coefficient in the BGL expansion for the form factor f. For $a_0^{f\mathrm{BGL}} \sim \mathcal{O}(1)$ this would give a contribution of $\mathcal{O}(1)$ to the form factor close to w^{max} where we have lattice data. In order to ensure that we do not bias our fit to small values of the BGL coefficients, it is therefore important that we go to sufficiently high order in $(w-1)$. We find that the $(w-1)^{10}$ coefficients for any of the HQET form factors give a

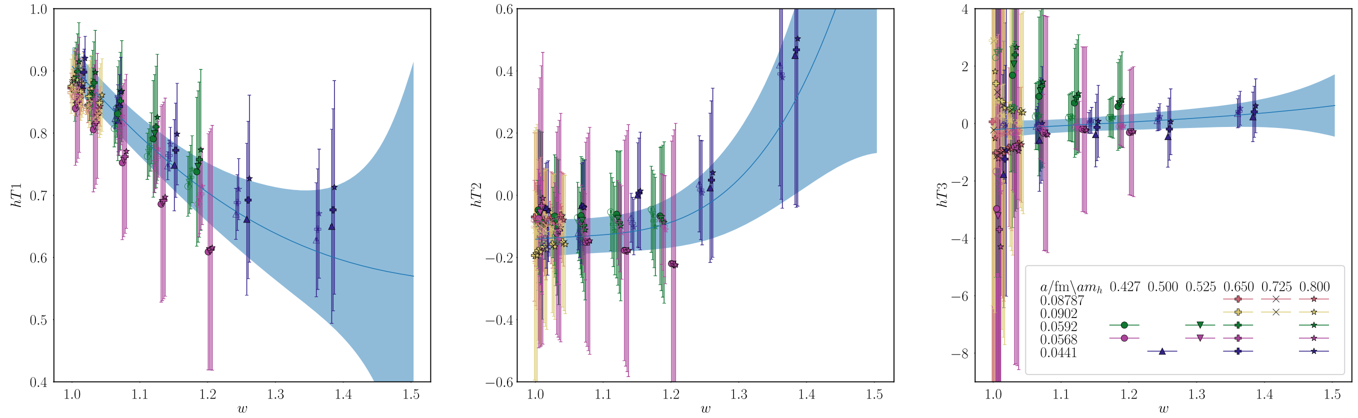

FIG. 4. The points show our lattice QCD results for each tensor form factor as given in Tables XXIV–XXVIII for $B \to D^*$ (filled points) and Tables XXXIV–XXXVIII for $B_s \to D_s^*$ (empty points) as a function of the recoil parameter, w. The legend gives the mapping between symbol color and shape and the set of gluon field configurations used, as given by the lattice spacing, and the heavy quark mass in lattice units (see Tables II and III). The blue curve with error band is the result of our fit in the continuum limit and with the physical b quark mass. Note that we include the data points for both the $B_s \to D_s^*$ and $B \to D^*$ form factors, and that for clarity data points at fixed w for different values of m_h are offset a small amount.

maximum contribution of $\mathcal{O}(0.01)$ for $\mathcal{O}(1)$ BGL coefficients close to $w^{\max}$. This is an order of magnitude smaller than the uncertainties on our lattice data points in this region, and so we truncate the power series in $(w-1)$ at order 10.

The $(\Lambda_{\rm QCD}/m_h)$, and δ_{m_q} polynomial terms are then included as modifications to the continuum $(w-1)$ coefficients. Note that for the tensor form factors, since there is currently no equivalent BGL expansion available in the literature, we instead use Gaussian priors of 0 ± 20 for each $(w-1)$ coefficient.

Additionally, our fit function must describe the pion mass dependence of our form factor data, including logarithms determined from staggered chiral perturbation theory [59,60]. The staggered chiral logarithms for the SM form factors were given in [26]. Following the methods in [59–61] we find that the staggered chiral logarithms for the tensor form factors for $B \to D^*$ are related straightforwardly to those for the SM form factors, with $\mathrm{logs}^{h_{T_1}^{(s)}}_{SU(3)} = \mathrm{logs}^{h_{A_1}^{(s)}}_{SU(3)}$, $\mathrm{logs}^{h_{T_3}^{(s)}}_{SU(3)} = \mathrm{logs}^{h_{A_2}^{(s)}}_{SU(3)}$, and $\mathrm{logs}^{h_{T_2}^{(s)}}_{SU(3)} = 0$ to one loop. For completeness, we also compute the logarithms for $B \to D$ and find that $\mathrm{logs}^{f_T}_{SU(3)} = \mathrm{logs}^{f_+}_{SU(3)}$. Full expressions for $\mathrm{logs}^{Y^{(s)}}_{SU(3)}$ are given in Appendix D. We also include polynomial terms in $(M_\pi/\Lambda_\chi)^2$ in our fit form, contained in $\delta_\chi^{(s)}$ in Eq. (22), where we take $\Lambda_\chi = 1$ GeV. We then fit our $B \to D^*$ and $B_s \to D_s^*$ data together by taking $M_\pi \to M_K$, $M_K \to M_S$, swapping $M_U \leftrightarrow M_S$ in the taste-axial-vector and taste-vector hairpin terms and suitably modifying the flavor-neutral taste-singlet terms. We label the form factors and observables corresponding to $B_s \to D_s^*$ with a superscript "s," Y^s. We use the taste splittings determined in [47] together with the relations given in [60] for the flavor-neutral pion mass eigenstates. We assume that the taste splittings behave as $M^2_{\pi_\xi} - M^2_{\pi_5} = n_\xi a^2 \delta_t$, where $n_A = 1$, $n_T = 2$, $n_V = 3$, and $n_I = 4$, and use the value for $\xi = A$ to determine δ_t. Note that on set 3 we use the observation that $\delta_t \propto a^2$ to fix the taste splitting, $a^2\delta_t$, to be 0.31 times that on set 2. We assume that the taste splittings are equal on sets 1 and 4, and on sets 2 and 5, respectively. We use the relation $\delta'_A = \delta'_V = -\delta_t$, which was found to be a good approximation for HISQ [51,62], to fix the hairpin coefficients.

Our fit function takes the explicit form

$$F^{Y^{(s)}}(w) = \sum_{n=0}^{10} a_n^{Y^{(s)}} (w-1)^n \mathcal{N}_n^{Y^{(s)}} + \frac{g^2_{D^*D\pi}}{16\pi^2 f_\pi^2}\left(\mathrm{logs}^{Y^{(s)}}_{SU(3)} - \mathrm{logs}^{Y^{(s)}}_{SU(3)\mathrm{phys}}\right), \quad (21)$$

where $g_{D^*D\pi}$ is the $D^* \to D\pi$ coupling, which is the same for $B \to D^*$ and $B_s \to D_s^*$ at the order to which we work in chiral perturbation theory. We take $f_\pi = 130$ MeV and neglect the uncertainty in f_π, since the uncertainty of the overall coefficient of the logs is dominated by that of $g_{D^*D\pi}$. Note that we subtract the physical point logarithms for $B \to D^*$ and $B_s \to D_s^*$ in each case; this ensures that at the physical point our fit function for $B \to D^*$ reduces to a polynomial in $(w-1)$. The physical chiral logs entering our fit function depend only mildly on w, as illustrated in Fig. 5, and so we expect the subtraction of the physical logs to only slightly modify the coefficients of the $(w-1)^n$ terms. We use the values of M_π computed in [2] given in Table II and M_K computed in [1] for sets 1–4. On set 5 we determine $M_K = 493$ MeV from independent correlator fits and take the physical values to be $M_\pi^{\rm phys} = 139.6$ MeV, $M_K^{\rm phys} = 493.7$ MeV, and $M_\eta^{\rm phys} = 547.9$ MeV.

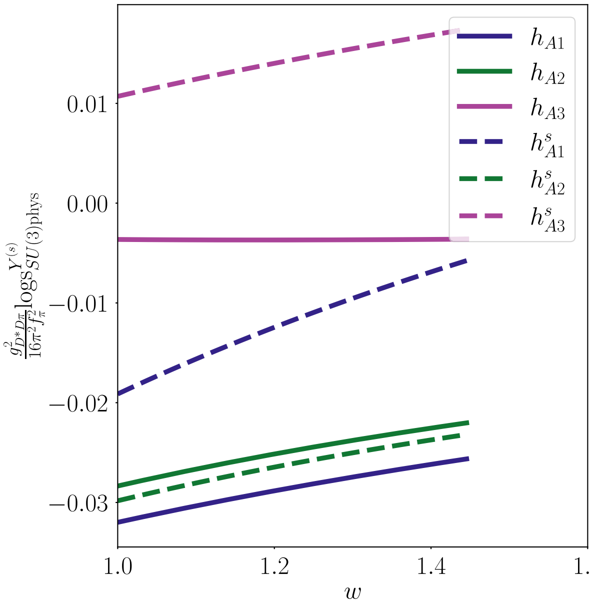

FIG. 5. The physical value of the logs in Eq. (21), $\frac{g^2_{D^*D\pi}}{16\pi^2 f_\pi^2}\mathrm{logs}^{Y^{(s)}}_{SU(3)}$, plotted for $g_{D^*D\pi} = 0.53$, illustrating the w and chiral dependence of our fit function. It can be seen that the log term varies slowly with w relative to the $(w-1)^n$ terms in our fit, and so we expect the subtraction of the physical $B \to D^*$ logs in Eq. (21) to only slightly modify the coefficients of the $(w-1)^n$ terms.

The coefficients, a_n^Y, for each form factor take the form

$$a_n^{Y^{(s)}} = \alpha_n^Y\left(1 + \sum_{j\neq 0}^{3} b_n^{Y,j}\Delta_h^{(j)} + \delta_\chi^{(s)}\sum_{j=0}^{3}\tilde{b}_n^{Y^{(s)},j}\Delta_h^{(j)}\right), \quad (22)$$

where

$$\delta_\chi^{(s)} = \left(\frac{M_{\pi(K)}}{\Lambda_\chi}\right)^2 - \left(\frac{M_\pi^{\mathrm{phys}}}{\Lambda_\chi}\right)^2 \quad (23)$$

allows for up to ≈25% difference between the $B \to D^*$ and $B_s \to D_s^*$ form factors. For $Y = h_{A_1}, h_{A_2}, h_{A_3}, h_V$ the $(w-1)^n$ coefficient, α_n^Y, is given by

$$\alpha_n^Y = \sum_{\substack{m=0,\\ X=f,F_1,F_2,g}}^{4} M_{nm,YX}^{\mathrm{BGL}\to\mathrm{HQET}}\, a_m^{X,\mathrm{BGL}} \quad (24)$$

with M the linear mapping from the continuum BGL z expansion parametrization to the expansion in powers of $(w-1)$ and $a_m^{X,\mathrm{BGL}}$ the BGL z^m coefficient for form factor X. Note that because of Luke's theorem [63] we set the coefficients $b_0^{h_{A_1},1}$ and $\tilde{b}_0^{h_{A_1}^{(s)},1}$, corresponding to the zero recoil continuum Λ/m_h term, equal to zero. The $\Delta_h^{(j)}$ allow for the dependence on the heavy quark mass. Here, we use the H_s mass as a proxy for the heavy quark mass. Note that w_0 and w_0/a, which are used to determine the lattice spacing on each set, are included as priors. We use $\Delta_h^{(0)} = 1$ and

$$\Delta_h^{(j\neq 0)} = \left(\frac{\Lambda}{M_{H_s}}\right)^j - \left(\frac{\Lambda}{M_{B_s}^{\mathrm{phys}}}\right)^j. \quad (25)$$

We take the physical value of the B_s mass to be $M_{B_s} = 5.36688$ GeV [3] and we take $\Lambda = 0.5$ GeV.

The remainder of Eq. (21), $\mathcal{N}_n^{Y^{(s)}}$, takes into account the small mistuning of the valence and sea quark masses.

$$\mathcal{N}_n^{Y^{(s)}} = 1 + A_n^{Y^{(s)}}\delta_{m_c}^{\mathrm{val}} + B_n^{Y^{(s)}}\delta_{m_c}^{\mathrm{sea}} + C_n^{Y^{(s)}}\delta_{m_s}^{\mathrm{val}} + D_n^{Y^{(s)}}\delta_{m_s}^{\mathrm{sea}} \quad (26)$$

with

$$\begin{aligned}
\delta_{m_c}^{\mathrm{val}} &= (am_c^{\mathrm{val}} - am_c^{\mathrm{tuned}})/am_c^{\mathrm{tuned}},\\
\delta_{m_c}^{\mathrm{sea}} &= (am_c^{\mathrm{sea}} - am_c^{\mathrm{tuned}})/am_c^{\mathrm{tuned}},\\
\delta_{m_s}^{\mathrm{val}} &= (am_s^{\mathrm{val}} - am_s^{\mathrm{tuned}})/(10am_s^{\mathrm{tuned}}),\\
\delta_{m_s}^{\mathrm{sea}} &= (am_s^{\mathrm{sea}} - am_s^{\mathrm{tuned}})/(10am_s^{\mathrm{tuned}}).
\end{aligned} \quad (27)$$

Note that $C_n^Y = 0$ so that the valence strange quark mistuning term is only included for the $B_s \to D_s^*$ case. The tuned values of the quark masses are given by

$$am_c^{\mathrm{tuned}} = am_c^{\mathrm{val}}\frac{M_{D_s^*}^{\mathrm{phys}}}{M_{D_s^*}}, \quad (28)$$

and

$$am_s^{\mathrm{tuned}} = am_s^{\mathrm{val}}\left(\frac{M_{\eta_s}^{\mathrm{phys}}}{M_{\eta_s}}\right)^2. \quad (29)$$

$M_{D_s^*}$ on each set is given in lattice units in Table XII and we use the values of M_{η_s} given in [9] which used the same values of am_s^{val}. We determine M_{η_s} on set 5 from independent correlator fits to be 0.19824(8). Since the η_s masses are only used to determine the strange quark mistuning, and because they are very precise, we neglect their correlations with our other data. We take priors of 0(1) for each b_n and $\tilde{b}_n$. We also use priors of 0.0(0.1) for $B_n^{Y^{(s)}}$, motivated by the results of the analysis of m_c^{sea} effects on w_0 in [53]. We take priors of 0.0(0.5) for $D_n^{Y^{(s)}}$ for each form factor, since sea quark mistuning effects enter at one loop. We take a prior for $g_{D^*D\pi}$ of 0.53(8), following [26].

Discretization effects enter our lattice calculation at the level of matrix elements. It is therefore important to account for them at this level, rather than at the level of the form factors, where cancellations may cause them to be underestimated. To do this, we convert the continuum form factors given by Eq. (21) to the matrix elements $J^{\nu,\Gamma}_{\mathrm{phys}} \equiv J^{00}_{nn(\nu,\Gamma)}$ given in Eqs. (18) and (20) and allow for discretization effects in this quantity. We then perform the fit against the matrix elements directly, simultaneously for the different combinations listed in Tables V and VI, including discretization effects using the fit form

$$\begin{aligned} J^{\nu,\Gamma(s)}_{\mathrm{latt}} &= J^{\nu,\Gamma(s)}_{\mathrm{phys}} + \sum_{j,n=0}^{3}\sum_{k,l\neq 0}^{3} c_n^{(\nu,\Gamma),jkl}\Delta_h^{(j)}(w-1)^n \\ &\quad\times\left(\frac{am_c^{\mathrm{val}}}{\pi}\right)^{2k}\left(\frac{am_h^{\mathrm{val}}}{\pi}\right)^{2l} \\ &\quad+\sum_{j,n=0}^{3}\sum_{k,l\neq 0}^{3} \tilde{c}_n^{(\nu,\Gamma)(s),jkl}\Delta_h^{(j)}(w-1)^n \\ &\quad\times\left(\frac{am_c^{\mathrm{val}}}{\pi}\right)^{2k}\left(\frac{am_h^{\mathrm{val}}}{\pi}\right)^{2l}\delta_\chi^{(s)}. \end{aligned} \tag{30}$$

We take priors of 0(1) for each c_n and $\tilde{c}_n$, multiplying terms of order $\mathcal{O}(a^2)$ by 0.5 in line with the tree level a^2 improvement of the HISQ action [24]. All of the remaining priors are taken as 0(1).

C. Tests of the stability of the analysis

Here, we demonstrate that our physical-continuum results are insensitive to variations in both the parameters chosen when fitting correlator data, as well as the parameters entering the chiral-continuum extrapolation. First, we repeat the analysis described in Sec. IV B using different combinations of the fits detailed in Table X. In order to assess the sensitivity of our results, we follow [23] and compare the values of the form factors, evaluated at $q^2 = 1$, $q^2 = 5$, and $q^2 = 10\ \mathrm{GeV}^2$. We perform this analysis in the physically important helicity basis, in which each form factor corresponds to a definite $D^*_{(s)}$ and W polarization. The SM form factors in this basis are defined via

$$\begin{aligned} g &= \frac{h_V}{M_{B_s}\sqrt{r}} \\ f &= M_{B_s}\sqrt{r}(1+w)h_{A_1} \\ F_1 &= M_{B_s}^2\sqrt{r}(1+w)((w-r)h_{A_1}-(w-1)(rh_{A_2}+h_{A_3})) \\ F_2 &= \frac{1}{\sqrt{r}}((1+w)h_{A_1}+(rw-1)h_{A_2}+(r-w)h_{A_3}). \end{aligned} \tag{31}$$

We also define definite helicity tensor form factors, related to the tensor helicity amplitudes given in Eq. (A12),

$$\begin{aligned} F_{T_1} &= (1+w)h_{T_1}+(w-1)h_{T_2}-h_{T_3}(w^2-1), \\ F_{T_2} &= h_{T_1}(1-r)(1+w)-h_{T_2}(1+r)(w-1), \\ F_{T_3} &= h_{T_1}(1+r)-h_{T_2}(1-r). \end{aligned} \tag{32}$$

These are plotted in Fig. 6 for f and g at $q^2 = 1$, $q^2 = 5$, and $q^2 = 10\ \mathrm{GeV}^2$, with $n = \delta_3 + 3\delta_2 + 9\delta_1 + 27\delta_4 + 81\delta_5$ tracking the different fit parameters, where δ_i is the value of δ given in Table X. In Fig. 6 we see that no combination of alternative correlator fit parameters listed in Table X results in a significant variation of f or g across the full kinematic range of the decay. Similar plots for the remaining form factors, including those for the tensor form factors, are given in the Supplemental Material [64], where we see that the other form factors are also stable to these variations.

We also investigate the effect of reducing the prior widths, as well as reducing the order summed to for each expansion parameter in Eq. (21). We evaluate the form factors, again at $q^2 = 1$, $q^2 = 5$, and $q^2 = 10\ \mathrm{GeV}^2$, for different combinations of these chiral-continuum extrapolation parameters. We also investigate the effect of reducing the order to which we sum in j, k, l in Eqs. (21), (22), and (30), as well as the effect of halving the prior widths of b_n^j and c_n^{jkl} defined in Eq. (22) and halving the prior widths of $\tilde{b}_n^j$, $\tilde{c}_n^{jkl}$ and $g_{D^*D\pi}$ in Eqs. (21) and (22). The resulting form factors for each modification of chiral-continuum extrapolation procedure are plotted in Fig. 7 for the form factors f and g, where we see that none of these changes to the extrapolation procedure result in a significant change to the form factors. Plots for the remaining $B \to D^*$ and $B_s \to D_s^*$ form factors are given in the Supplemental Material [64], where we see that none of our form factors are sensitive to these changes.

D. Error budget

In Fig. 8 we plot the fractional contribution of each source of uncertainty to the total variance for the form factors f and g across the full kinematic range of the decay. These are computed from the partial variance of the form factor at each w with respect to the priors, and so the size of each band represents the extent to which the corresponding terms in the chiral-continuum fit are not constrained by the data. The band labeled χ_π corresponds to the priors $\tilde{c}_n^{jkl}$, $\tilde{b}_n^j$ and $g_{D^*D\pi}$, Λ/M_h corresponds to the priors $b_n^{j\neq 0}$, am_c to $c_n^{0k\neq 00}$, am_h to $c_n^{00l\neq 0}$, δ_m to the priors entering $\mathcal{N}_n^Y$, and "mixed" corresponds to priors for b_n^j c_n^{jkl} where at least two of j, k. or l are nonzero. "Statistical" corresponds to the uncertainty from our data. Unsurprisingly, we see that close to $w = 1$ where we have data on all ensembles for all masses we have very good control over the discretization, chiral and heavy-mass dependence, whereas towards the maximum value of w, corresponding to $q^2 = 0$, where we have less coverage with our data, we see that the uncertainty coming from unconstrained terms in our fit function is larger. For the SM form factors, we generally find that control over discretization effects set by am_h, as well as control over the physical heavy mass dependence, are the dominant sources of uncertainty not constrained by the data. Plots for F_1 and F_2 as well as the tensor form factors in the helicity basis defined in Eq. (32), are given in

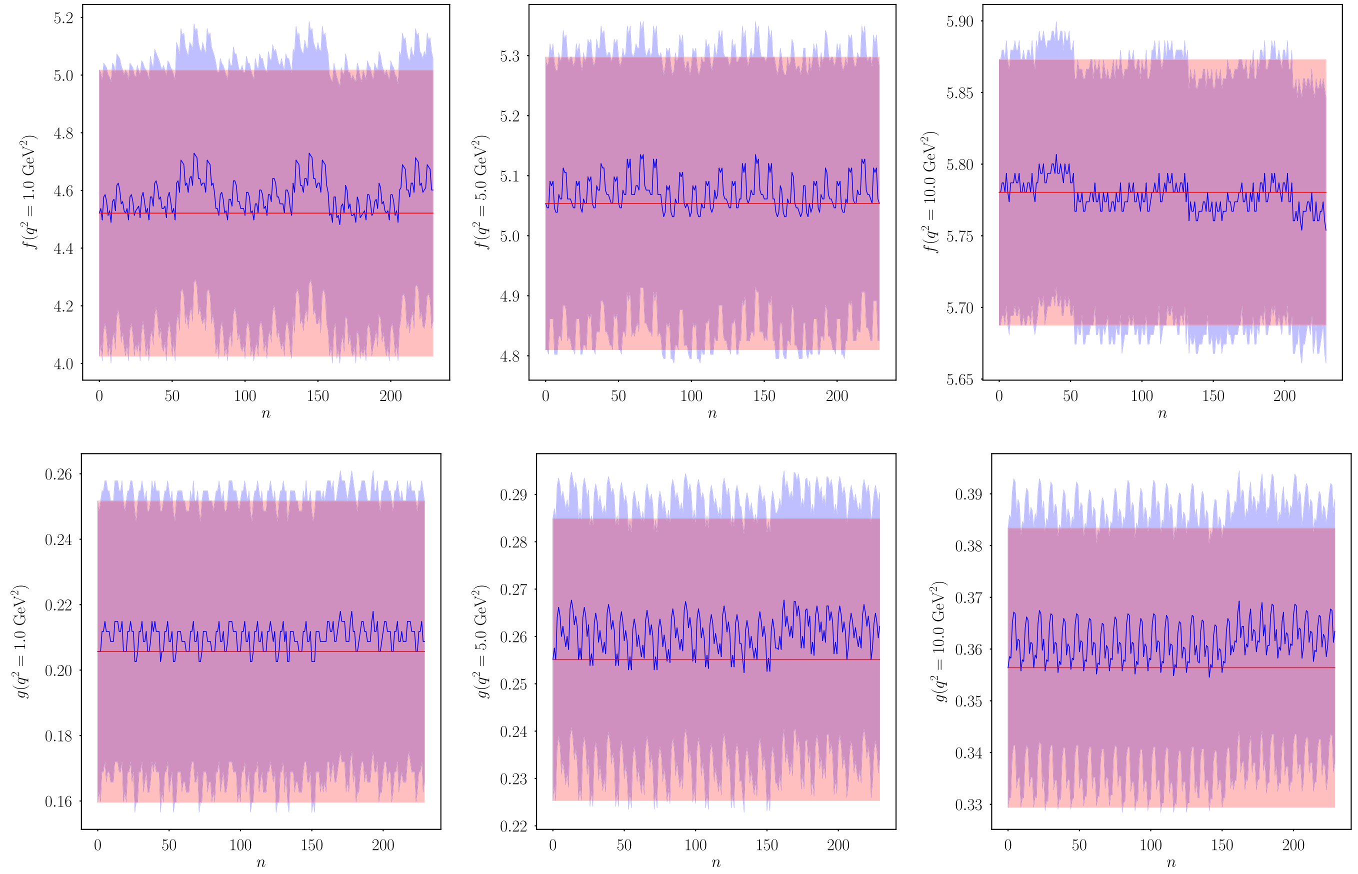

FIG. 6. Values of the form factors f and g for $B \to D^*$ evaluated at $q^2 = 1$, $q^2 = 5$, and $q^2 = 10\ \mathrm{GeV}^2$ for different combinations of correlator fits using different parameters. The red line and error band corresponds to our chosen combination and the blue line and error band corresponds to the form factors resulting from different fit combinations. Here, $n = \delta_3 + 3\delta_2 + 9\delta_1 + 27\delta_4 + 81\delta_5$ where δ_i is the value of δ for set i given in Table X. We see that no combination of correlator fits results in a significant variation of f or g.

Figs. 21 and 22 in Appendix C, where we see a similar situation for F_1, F_2, F_{T_2}, and F_{T_3}. The uncertainty in F_{T_1} is dominated by the unconstrained chiral dependence of the factor h_{T_3}, shown in Fig. 4. We also show plots for the $B_s \to D_s^*$ form factor uncertainties in Appendix C, with similar behavior to those for $B \to D^*$.

E. BGL form factor parametrization

For comparison to other lattice and experimental determinations, we fit synthetic data points generated at $w = 1.025$, $w = 1.225$, and $w = 1.425$ for each $B \to D^*$ form factor in the helicity basis, defined in Eq. (31), using the BGL parametrization [13]. The BGL parametrization expresses the form factors as

$$\mathcal{F}(t) = \frac{1}{P(z)\phi(z)} \sum_{n=0}^{\infty} a_n^{\mathcal{F}} z(t, t_0)^n. \tag{33}$$

Here we adopt the conventions for Blaschke factors $P(z)$, outer functions $\phi(z)$, $B_c^{(*)}$ resonances of [14] which were also used in [26]. We include up to quadratic order in z, though we have confirmed that going to cubic order has only a very small effect on the resulting coefficients. We also enforce the condition $F_1(w = 1) = M_B(1 - r)f(w = 1)$ by fixing $a^0_{F_1} = a^0_f(1 - r)/\sqrt{2}(1 + \sqrt{r})^2$. Note that here we take uniformly distributed priors between -1 and 1 for each $a_n^{\mathcal{F}}$. Although we do not enforce the condition at w_{max}, $F_2(w_{\mathrm{max}}) = (1+r)/(M_B^2(1+w_{\mathrm{max}})(1-r)r)F_1(w_{\mathrm{max}})$, we find that our fit satisfies this condition to within 0.07σ. The fit parameters a_i should satisfy the unitarity bounds given by

$$\sum_i^{\infty} |a_i^g|^2 \leq 1,$$

$$\sum_i^{\infty} |a_i^f|^2 + |a_i^{F_1}|^2 \leq 1,$$

$$\sum_i^{\infty} |a_i^{F_2}|^2 \leq 1. \tag{34}$$

The results of this fit are given in Table XIV, where we see that for the form factors g, f, and $F1$ we have a reasonably good agreement with [26], and comparable uncertainties (cf. Table 11 in that paper). However, for F_2 we find a tension at the level of 2σ. Table XIV includes checks of the unitarity

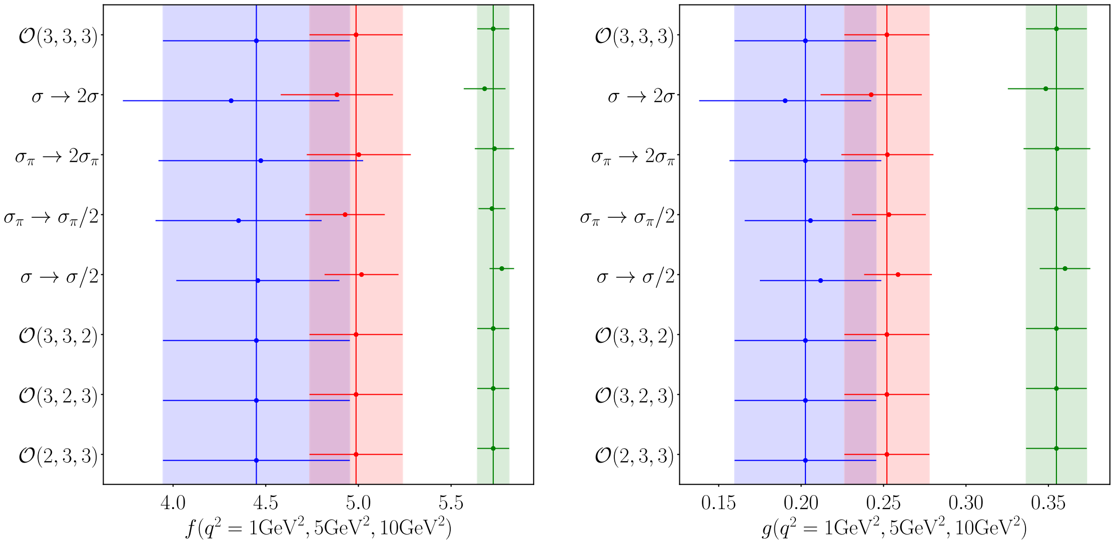

FIG. 7. Values of the form factors f and g for $B \to D^*$ evaluated at $q^2 = 1$, $q^2 = 5$, and $q^2 = 10\ \mathrm{GeV}^2$, corresponding to the blue, red, and green points respectively, for different combinations of chiral-continuum extrapolation parameters. $\sigma \to \sigma/2$ indicates that we multiply the prior widths of b_n^j and c_n^{jkl} defined in Eqs. (22) and (30) by 0.5 and $\sigma \to 2\sigma$ indicates that we multiply the prior widths of b_n^j and c_n^{jkl} defined in Eqs. (22) and (30) by 2. $\sigma_\pi \to \sigma_\pi/2$ indicates that we multiply the prior widths of $\tilde{b}_n^j$, $\tilde{c}_n^{jkl}$ and $g_{D^*D\pi}$ by 0.5 in Eqs. (21), (22), and (30), and $\sigma_\pi \to 2\sigma_\pi$ indicates that we multiply the prior widths of $\tilde{b}_n^j$, $\tilde{c}_n^{jkl}$ and $g_{D^*D\pi}$ by 2. $\mathcal{O}(n_{M_H}, n_{am_c}, n_{am_h})$ indicates the order to which we sum in j, k, l respectively in Eqs. (21), (22), and (30). For each fit going from top to bottom, the χ^2 values are 62, 55, 59, 64, 70, 62, 62, and 62, respectively, for 1224 degrees of freedom.

bounds, Eq. (34), which we find to be far from saturation for the number of coefficients we include.

F. Reconstructing our form factors

We have included in the Supplemental Material [64] a PYTHON script, LOAD_FIT.PY, that reads our physical-continuum HQET fit parameters [see Eq. (21)] and their correlations from the file hpqcd_BDstar.pydat, in order to build the $B \to D^*$ and $B_s \to D_s^*$ form factors in the HQET basis. Note that the $B_s \to D_s^*$ form factors given here supersede those given in [23]. The script also performs checks against the values of the form factors at five equally spaced values of q^2, stored in CHECKS.txt and CHECKS_s.txt. We also provide a file SYNTHETIC_DATA.PYDAT, which may be loaded into PYTHON using GVAR.GLOAD, which contains synthetic data points for the form factors in the HQET basis computed at five equally spaced values of $q^2 = i \times q^2_{\mathrm{max},(s)}/4, i \in [0, 1, 2, 3, 4]$ for the $B_{(s)} \to D^*_{(s)}$ form factors. These synthetic data points are also checked against those computed from our fit parameter text files in LOAD_FIT.PY. We have run these scripts using PYTHON-3.10.6, using the packages NUMPY-1.21.5, SCIPY-1.8.0, GVAR-11.10.1 and MATPLOTLIB-3.5.1.

V. DISCUSSION

A. Comparison to experiment, $|V_{cb}|$

We can use our form factors together with the untagged data for $B \to D^* e^- \bar{\nu}_e$ and $B \to D^* \mu^- \bar{\nu}_\mu$ from Belle [21] in order to extract $|V_{cb}|$. We use our physical-continuum form factor parameters, given in the Supplemental Material [64] as described in Sec. IV F, as priors to fit the experimental differential rate data from Belle, which has been binned in each of the variables w, θ_{D^*}, θ_W, and χ defined in Fig. 1. Note that throughout this section we assume no lepton flavor universality (LFU) violation between the light $\ell = \mu$ and $\ell = e$ modes.

The covariance matrix for the Belle data does not include the zero eigenvalues expected from the fact that the bins for a given variable must sum to the same total. In order to remedy this issue we normalize the bins for each variable so that they sum to 1. This ensures that the covariance matrix contains the expected zero eigenmodes, which we then remove explicitly using an SVD cut. Following the observation in [26] that the experimental data used to extract V_{cb} was dominated by the Belle dataset, we do not include any synthetic data points generated using fits from *BABAR* [28].

Once the fit to Belle data described above has been performed, a value of $|V_{cb}|$ can be read off by comparing the total number of events to $\Gamma/|V_{cb}\eta_{\mathrm{EW}}|^2$ computed using the form factors resulting from the joint theory/experiment fit. We fit all four variables simultaneously, though we have checked that fitting the Belle data for any single variable on its own does not change the uncertainty in the resulting value of $|V_{cb}|$, exactly as one would expect from the fact that the sum of each set of ten bins must be equal. In order to reconstruct the combined electron-muon 80×80 covariance matrix we follow the procedure described in [65] so

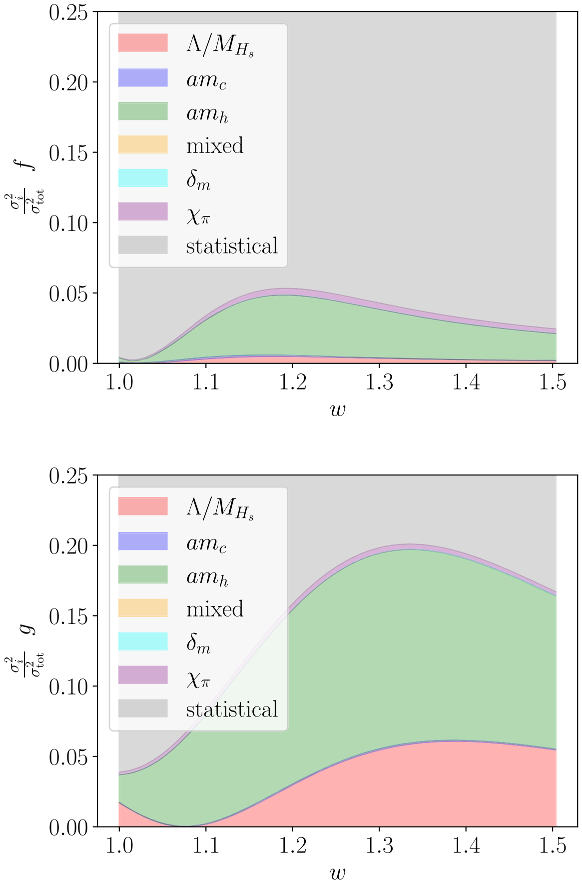

FIG. 8. Plots showing the fractional contribution of each source of uncertainty to the total variance for the form factors f and g across the full kinematic range. The vertical axis is truncated at 0.25 for clarity, with the remaining variance between 0.25 and 1 attributable to statistics.

that we may fit the $\ell = \mu$ and $\ell = e$ cases simultaneously, assuming no NP in either mode.

Since we have computed fully correlated form factors for both $B \to D^*$ and $B_s \to D_s^*$, it is possible for us to include data from LHCb [66] for $B_s \to D_s^*$ in our fits. Even though this data is more limited, it can still inform the shape of the form factors. We include the LHCb $B_s \to D_s^*$ data in our fits in the same manner as the Belle data, integrating our differential decay rate over the bins used by LHCb and then including these in our χ^2 minimization. However, since the available $B_s \to D_s^*$ experimental data is significantly less precise than that for $B \to D^*$, the inclusion of the LHCb data does not significantly change the central value or uncertainty of $|V_{cb}|$ determined in this way.

Our lattice-only normalized differential decay rates for $B \to D^*$ and $B_s \to D_s^*$ are shown in Figs. 9 and 10 respectively, together with the experimental data points for each bin. We see a difference in shape between our results and the binned data from Belle and LHCb. The fit to our results along with Belle and LHCb data gives $\chi^2/\mathrm{d.o.f.} = 0.95$ and $Q = 0.55$. The visible disagreement in shape we see here is qualitatively similar to what was seen in [26], where the authors observed a 2σ discrepancy across the full kinematic range of the decay after extrapolating their lattice results (covering $1 \leq w \leq 1.175$) to w_{max} using the BGL parametrization.

TABLE XIV. BGL fit parameters, defined in Eq. (33), for our $B \to D^*$ form factors. Here we also include the sums of squared coefficients, which we see are far from saturating the unitarity bounds in Eq. (34).

a_0^g	0.0318(25)
a_1^g	−0.114(96)
a_2^g	0.05(76)
a_0^f	0.01222(20)
a_1^f	0.014(16)
a_2^f	−0.17(45)
a_0^{F1}	0.002047(33)
a_1^{F1}	−0.0082(88)
a_2^{F1}	−0.05(27)
a_0^{F2}	0.0447(34)
a_1^{F2}	−0.22(13)
a_2^{F2}	−0.009(797)
$\sum_i^3 \lvert a_i^g \rvert^2$	0.017(86)
$\sum_i^3 \lvert a_i^f \rvert^2 + \lvert a_i^{F_1} \rvert^2$	0.03(16)
$\sum_i^3 \lvert a_i^{F_2} \rvert^2$	0.052(59)

Using our fit to our lattice results along with the experimental data enables us to determine $|V_{cb}|$. We find

$$|V_{cb}| = 39.03(56)_{\mathrm{exp}}(67)_{\mathrm{latt}} \times 10^{-3} \tag{35}$$

in good agreement with previous exclusive determinations [10]. Note that in determining V_{cb} we take $|\eta_{\mathrm{EW}}|^2 = (1.00662)^2 \times (1 + \alpha_{\mathrm{QED}}\pi)$, with an additional Coulomb factor [67,68] for the charged final states in the decay measured by Belle, $B^0 \to D^{*-}\ell^+\bar{\nu}_\ell$, and neglect the uncertainty.

For the purpose of comparison to other lattice QCD results from [26], we plot $|\mathcal{F}(w)V_{cb}\eta_{\mathrm{EW}}|^2$ in Fig. 11, where we use V_{cb} extracted from our joint theory/experiment fit, Eq. (35), to multiply $|\mathcal{F}(w)|^2$ computed using only our form factors. $\mathcal{F}(w)$ is defined according to the equation for the differential rate with respect to w:

$$\begin{aligned} \frac{d\Gamma(B_{(s)} \to D^*_{(s)}\ell\bar{\nu}_\ell)}{dw} &= \frac{G_F^2}{48\pi^3}(M_{B_{(s)}} - M_{D^*_{(s)}})^2 M^3_{D^*_{(s)}} \sqrt{w^2-1}(w+1)^2 \\ &\times \left[1 + \frac{4w}{w+1}\frac{M^2_{B_{(s)}} - 2wM_{B_{(s)}}M_{D^*_{(s)}} + M^2_{D^*_{(s)}}}{(M_{B_{(s)}} - M_{D^*_{(s)}})^2}\right] \\ &\times |\mathcal{F}^{(s)}(w)\eta_{\mathrm{EW}}V_{cb}|^2. \end{aligned} \tag{36}$$

Figure 11 confirms the disagreement in shape of $|\mathcal{F}|^2$ seen in [26] between the SM and Belle data.

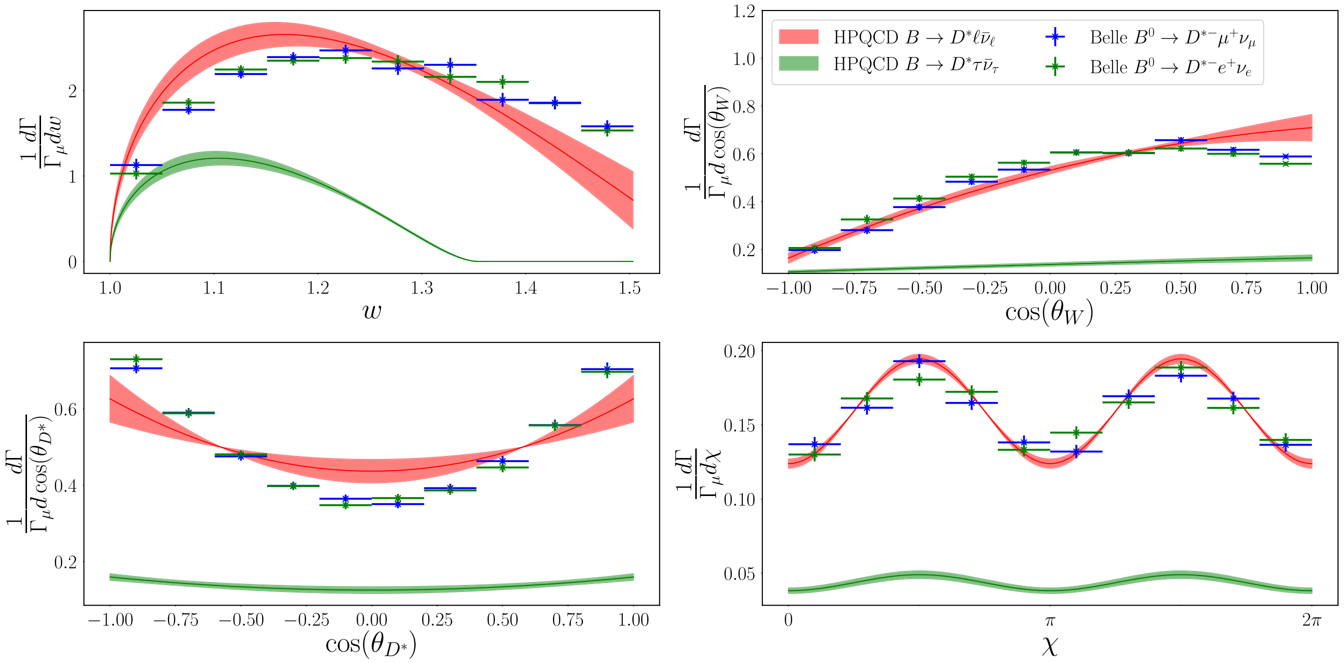

FIG. 9. Our lattice-only normalized differential decay rates for $B \to D^*\ell\bar{\nu}$, with respect to the angular variables defined in Fig. 1, are shown as the red bands. We also include binned untagged data for e/μ from Belle [21]. Note the clear difference in shape, particularly for the differential rate with respect to w. Our tauonic differential decay rates are shown in green.

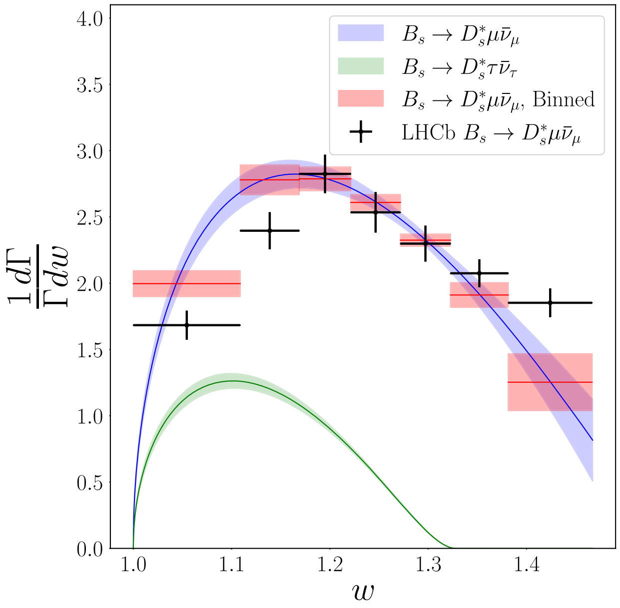

FIG. 10. Our normalized differential decay rate for $B_s \to D_s^*\ell\bar{\nu}$ with respect to w is shown as the blue band. We also include binned data from LHCb [66]. Here, as for $B \to D^*$, we see a similar difference in shape between SM theory and experiment to that seen for Belle $B \to D^*$ data in Fig. 9. The semitauonic mode is plotted as the green band.

It has been emphasized that a precise determination of the slope of $\mathcal{F}$ at $w = 1$ could significantly reduce the uncertainty in V_{cb} [18]. While it is preferable to extract V_{cb} using lattice and experimental data across the full kinematic range, it is still interesting to examine the slope at $w = 1$.

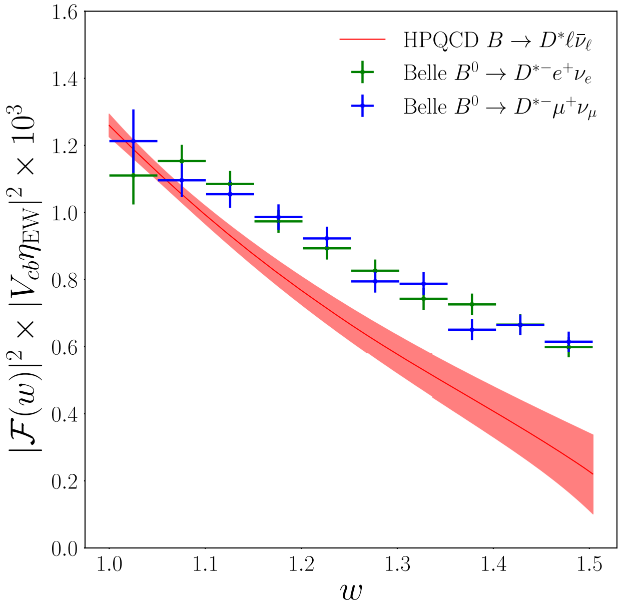

FIG. 11. $|\mathcal{F}(w)\eta_{\rm EW}V_{cb}|^2$, defined via Eq. (36), plotted against w. Our lattice-only $|\mathcal{F}(w)|^2$ is multiplied by V_{cb} extracted from the joint theory/experiment fit.

We find, for $B \to D^*$ and $B_s \to D_s^*$,

$$\left.\frac{dF}{dw}\right|_{w=1} = -0.97(15),$$
$$\left.\frac{dF^s}{dw}\right|_{w=1} = -0.94(11). \tag{37}$$

The value for dF^s/dw is in good agreement with the value of $-0.94(15)$ from our previous study [23], and we find that the slope in both light and strange spectator cases agrees well.

V_{cb} may also be computed by combining the total decay rate from our lattice form factors and the Belle total rate without using the differential rate information. Doing this, we find $V_{cb} = 42.9(0.5)_{\text{exp}}(2.2)_{\text{latt}} \times 10^{-3}$, a larger value than that in Eq. (35) and in much better agreement with the inclusive value. This value may be understood from Fig. 11, where it is apparent that our lattice results multiplied by $|V_{cb}|^2$ from Eq. (35) lie below the binned experimental data, and so give a greater value of V_{cb} when only the total rate is considered. This approach discards information about the form factors contained in the shape of the experimentally measured differential rate, that otherwise constrains the form factors, and so results in a greater uncertainty. We may also use the experimental average branching fraction, $\mathcal{B}(B^+ \to D^{*0}\ell^+\nu_\ell)$, and B^+ lifetime from the Particle Data Group [69] to calculate the total decay rate, which we can then combine with our lattice results to find $V_{cb} = 43.4(0.9)_{\text{exp}}(2.2)_{\text{latt}} \times 10^{-3}$, consistent with the value above determined using the Belle total decay rate alone. Note that the total rate for $B^+ \to D^{*0}\ell^+\nu_\ell$ does not include the additional Coulomb factor, $(1 + \alpha_{\text{QED}}\pi)$, required for $B^0 \to D^{*-}\ell^+\nu_\ell$ [67,68].

B. Γ, $R(D^*_{(s)})$ and angular observables

We can use our form factors to compute the total decay rates for the different processes, normalized by the combination $|V_{cb}\eta_{\text{EW}}|^2$. We find

$$\begin{aligned}
\Gamma(B \to D^* e\bar{\nu}_e)/|V_{cb}\eta_{\text{EW}}|^2 &= 1.13(12) \times 10^{-11}\ \text{GeV},\\
\Gamma(B \to D^* \mu\bar{\nu}_\mu)/|V_{cb}\eta_{\text{EW}}|^2 &= 1.13(11) \times 10^{-11}\ \text{GeV},\\
\Gamma(B \to D^* \tau\bar{\nu}_\tau)/|V_{cb}\eta_{\text{EW}}|^2 &= 3.10(17) \times 10^{-12}\ \text{GeV},\\
\Gamma(B_s \to D_s^* e\bar{\nu}_e)/|V_{cb}\eta_{\text{EW}}|^2 &= 1.201(63) \times 10^{-11}\ \text{GeV},\\
\Gamma(B_s \to D_s^* \mu\bar{\nu}_\mu)/|V_{cb}\eta_{\text{EW}}|^2 &= 1.197(63) \times 10^{-11}\ \text{GeV},\\
\Gamma(B_s \to D_s^* \tau\bar{\nu}_\tau)/|V_{cb}\eta_{\text{EW}}|^2 &= 3.20(10) \times 10^{-12}\ \text{GeV}.
\end{aligned} \tag{38}$$

Note that the total decay rates for $B_s \to D_s^*$ are approximately 1σ lower than those computed by us previously in [23]. This is discussed further in Appendix E, where we compare our updated form factors for $B_s \to D_s^*$ to those in [23].

TABLE XV. $R(D^*_{(s)})$ and $R^{\text{imp}}(D^*_{(s)})$ computed first using our form factors only, as well as computed using our form factors together with the joint fits to experimental data described in the text. Here we see that the inclusion of experimental data moves the values down by $\approx 2\sigma$, and reduces their uncertainties.

	Lattice-only	Lattice + experiment
$R(D^*)$	0.273(15)	0.2482(20)
$R(D_s^*)$	0.266(9)	0.2459(34)
$R^{\text{imp}}(D^*)$	0.342(6)	0.3372(23)
$R^{\text{imp}}(D_s^*)$	0.340(3)	0.3358(21)

We use our form factors to compute $R(D^*_{(s)})$, defined in Eq. (1). We compute both a lattice-only value, using only our computed form factors, as well as a lattice + experiment value where we use the form factors resulting from our fits to lattice and experimental data in Sec. V A. These are given in Table XV, together with the improved ratios in which the rates are integrated only between q^2_{max} and m_τ^2,

$$R^{\text{imp}}(D^*_{(s)}) = \frac{\int_{m_\tau^2}^{q^2_{\text{max}}} dq^2 \frac{d\Gamma}{dq^2}(B_{(s)} \to D^*_{(s)}\tau\bar{\nu}_\tau)}{\int_{m_\tau^2}^{q^2_{\text{max}}} dq^2 \frac{d\Gamma}{dq^2}(B_{(s)} \to D^*_{(s)}\mu\bar{\nu}_\mu)}. \tag{39}$$

We see that the inclusion of experimental data shifts $R(D^*)$ downwards significantly and reduces the uncertainty. Our lattice-only $R(D^*)$ is shown in Fig. 12, together with the lattice + experiment value. In that figure we also plot the lattice-only and lattice + experiment values of $R(D^*)$ computed by the Fermilab-MILC collaboration [26], where the

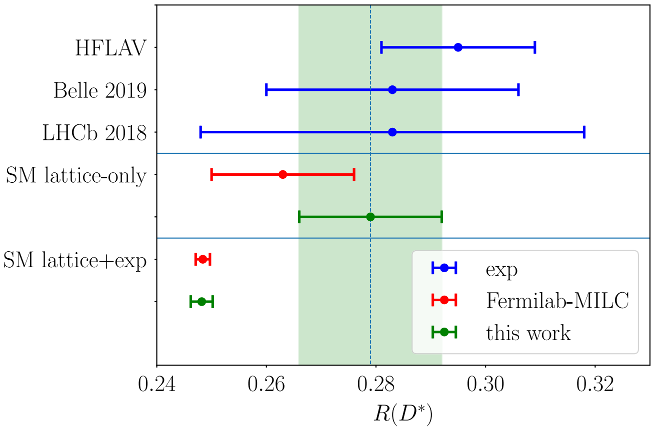

FIG. 12. "Lattice-only" and "lattice + experiment" values of $R(D^*)$. The results of this work are shown in green, while the recent results from the Fermilab-MILC collaboration [26] are shown in red. The inclusion of experimental data produces a similar downward shift in both cases. The two most recent experimental measurements of $R(D^*)$, from Belle [34] and LHCb [35], are also shown in blue, together with the HFLAV average value.

inclusion of experimental data produces a similar downward shift. The two most recent experimental measurements of $R(D^*)$, from Belle [34] and LHCb [35], are also shown, together with the heavy flavor averaging group (HFLAV) average value.

We may also use our form factors to compute observables related to the angular asymmetry of the decay. Here we compute the lepton polarization asymmetry, $\mathcal{A}_{\lambda_\ell}$, the longitudinal polarization fraction, $F_L^{D^*_{(s)}}$, and the forward-backward asymmetry, $\mathcal{A}_{FB}$. These are defined as

$$\begin{aligned}\mathcal{A}_{\lambda_\ell}(q^2) &= \frac{d\Gamma^{\lambda_\ell=-1/2}/dq^2 - d\Gamma^{\lambda_\ell=+1/2}/dq^2}{d\Gamma/dq^2},\\ F_L^{D^*_{(s)}}(q^2) &= \frac{d\Gamma^{\lambda_{D^*_{(s)}}=0}/dq^2}{d\Gamma/dq^2},\\ \mathcal{A}_{FB}(q^2) &= -\frac{1}{d\Gamma/dq^2}\frac{2}{\pi}\int_0^\pi \frac{d\Gamma}{dq^2 d\cos(\theta_W)}\cos(\theta_W)d\theta_W.\end{aligned} \tag{40}$$

The integrated observables related to these quantities are defined as in [23] with the numerators and denominators integrated over q^2 independently. We find for $B \to D^*\tau\bar{\nu}_\tau$

$$\begin{aligned}\langle\mathcal{A}_{\lambda_\tau}\rangle &= 0.547(19),\\ \langle F_L^{D^*}\rangle &= 0.395(24),\\ \langle\mathcal{A}_{\text{FB}}\rangle &= 0.100(25),\end{aligned} \tag{41}$$

and for $B_s \to D_s^*\tau\bar{\nu}_\tau$

$$\begin{aligned}\langle\mathcal{A}^s_{\lambda_\tau}\rangle &= 0.5331(91),\\ \langle F_L^{D_s^*}\rangle &= 0.420(12),\\ \langle\mathcal{A}^s_{\text{FB}}\rangle &= 0.084(12).\end{aligned} \tag{42}$$

These values are in disagreement with expectations from the heavy quark expansion (HQE) [37]. They are also in tension at the level of 2.2σ with the recent measurement of the D^* longitudinal polarization fraction by Belle [39], $F_L^{D^*\text{Belle}} = 0.60(8)_{\text{stat}}(4)_{\text{sys}}$. Our value of $\langle\mathcal{A}_{\lambda_\tau}\rangle = -P_\tau(D^*)$ is in good agreement with the measured value from Belle [38], although there is a large statistical uncertainty on the experimental measurement: $P_\tau(D^*) = -0.38 \pm 51_{(\text{stat})}{}^{+21}_{-16(\text{syst})}$.

C. $SU(3)_{\text{flav}}$

$SU(3)_{\text{flav}}$ symmetry breaking effects between $B \to D^*$ and $B_s \to D_s^*$ are expected to be small [37]. $R(D^*)$ and $R(D_s^*)$ are expected to differ by ≈1%. Here, using our lattice-only results, we find

$$R(D^*)/R(D_s^*) = 1.028(50). \tag{43}$$

This result, together with our result for $R(J/\psi)$ [45], implies the simple relation to increasing spectator quark mass $R(D^*) > R(D_s^*) > R(J/\psi)$. We also compute the ratios of the angular observables given in Sec. V B. We find

$$\begin{aligned}\langle\mathcal{A}_{\lambda_\tau}\rangle/\langle\mathcal{A}^s_{\lambda_\tau}\rangle &= 1.040(29),\\ \langle F_L^{D^*}\rangle/\langle F_L^{D_s^*}\rangle &= 0.942(46),\\ \langle\mathcal{A}_{\text{FB}}\rangle/\langle\mathcal{A}^s_{\text{FB}}\rangle &= 1.19(23).\end{aligned} \tag{44}$$

These results are in slight tension with the HQE expectation of ≈1% $SU(3)_{\text{flav}}$ symmetry breaking, though this tension is not significant for our level of uncertainty. The SM form factors for $B \to D^*$ and $B_s \to D_s^*$ are plotted in the helicity basis in Figs. 13 and 14, where we see $SU(3)_{\text{flav}}$ symmetry breaking with difference ranges from ≈1% for f and g up to ≈10% for F_2.

D. Constraining new physics in $B \to D^*\ell\bar{\nu}_\ell$

The effective Hamiltonian Eq. (3) is most commonly expressed in terms of left- and right-handed fermions as

$$\begin{aligned}\mathcal{H}_{\text{eff}} = \frac{4G_F V_{cb}}{\sqrt{2}}\big[&g_{V_L}\bar{c}_L\gamma_\mu b_L\bar{\ell}_L\gamma^\mu\nu_L + g_{V_R}\bar{c}_R\gamma_\mu b_R\bar{\ell}_L\gamma^\mu\nu_L\\ &+ g_{S_L}\bar{c}_R b_L\bar{\ell}_R\nu_L + g_{S_R}\bar{c}_L\gamma_5 b_R\bar{\ell}_R\nu_L\\ &+ g_{T_L}\bar{c}_R\sigma_{\mu\nu}b_L\bar{\ell}_R\sigma^{\mu\nu}\nu_L + \text{H.c.}\big],\end{aligned} \tag{45}$$

where $g_{T_L} = (g_T - g_{T5})/2$, $g_{V_L} = (g_V - g_A)/2$, $g_{V_R} = (g_V + g_A)/2$, $g_{S_L} = (g_S - g_P)/2$, and $g_{S_R} = (g_S + g_P)/2$. Note that there is no g_{T_R}, since the corresponding current, $\bar{c}_L\sigma_{\mu\nu}b_R\bar{\ell}_R\sigma^{\mu\nu}\nu_L$, is identically zero. Here we have given the effective Hamiltonian for only a single flavor of lepton. Unlike in Sec. V A, we will now not assume LFU between the $\ell = \mu$ and $\ell = e$ modes and instead study each case separately. The couplings for each lepton flavor will be indicated by a superscript, as in g_X^ℓ.

In [70] the authors give the patterns of couplings produced by different tree level models of NP. For the models they considered at most one of either the left- or right-handed vector coupling differed from its SM value, together with different nonzero combinations of the left- and right-handed scalar couplings and left-handed tensor coupling. Throughout this subsection we compute constraints for different combinations of the various couplings and V_{cb}. Because g_{V_L} may be absorbed into V_{cb}, it is sufficient in our case to fix $g_{V_L} = 1$. For $g_{V_L} \neq 1$ one should take $g_X \to \tilde{g}_X = g_X/g_{V_L}$ and $V_{cb} \to \tilde{V}_{cb} = V_{cb} \times g_{V_L}$ in the constraints given below. In order to compute the constraints we fit the Belle data using our lattice form factors in the same manner as described in Sec. V A, for fixed numerical values of g_X. We fit the normalized binned differential data from Belle, and only include the total rate,

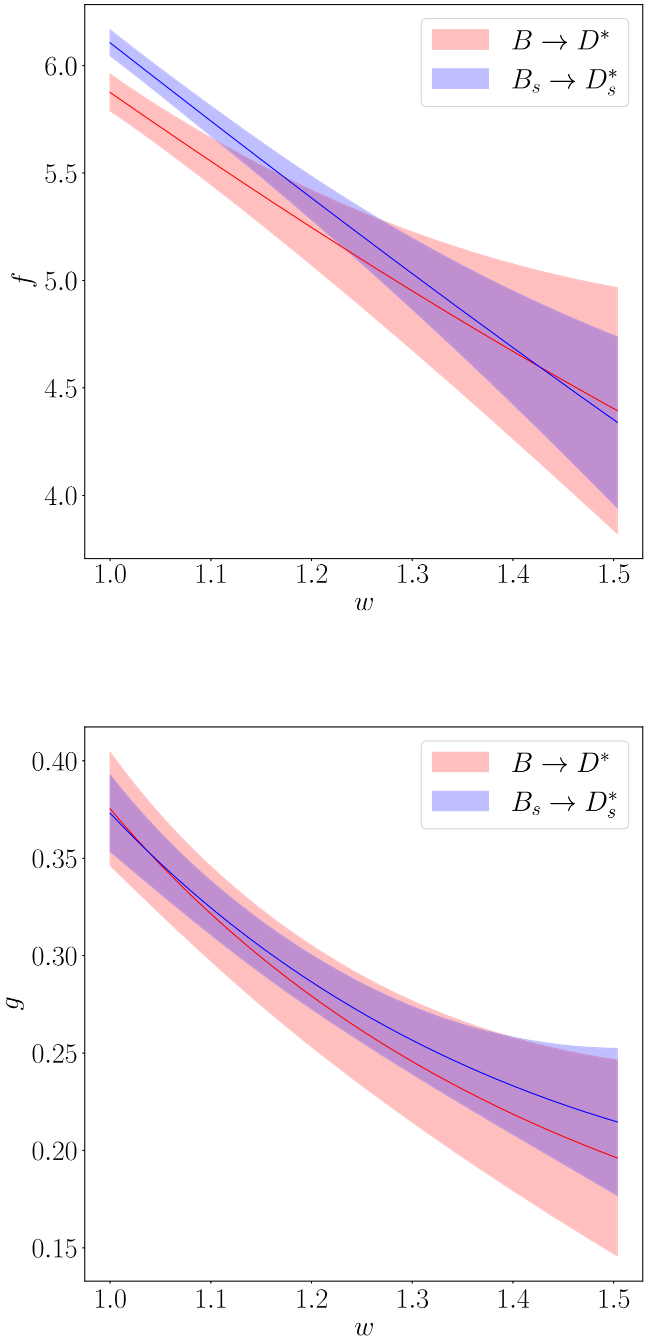

FIG. 13. $B \to D^*$ and $B_s \to D_s^*$ helicity basis form factors f and g, defined in Eq. (31).

Γ, as a single additional data point when we compute constraints including V_{cb}.

1. Scalar operators

In [70] it was found that $B \to D^*$ produces only very weak constraints on the left-handed scalar coupling. Indeed, using just $B \to D^*$ it is only possible to constrain the pseudoscalar combination $g_{S_L} - g_{S_R} = g_P$, with the QCD matrix element of the scalar current zero by parity as shown in Eq. (6). We find the constraints considering modifications to g_P alone are very weak, as shown in Fig. 15 for both $\ell = e$ and $\ell = \mu$. Note that, since $B \to D\ell\nu$ provides complementary constraints for the scalar operators, fully correlated lattice results for both $B \to D^*$ and $B \to D$ SM and NP form factors would allow for the simultaneous constraint of all NP couplings.

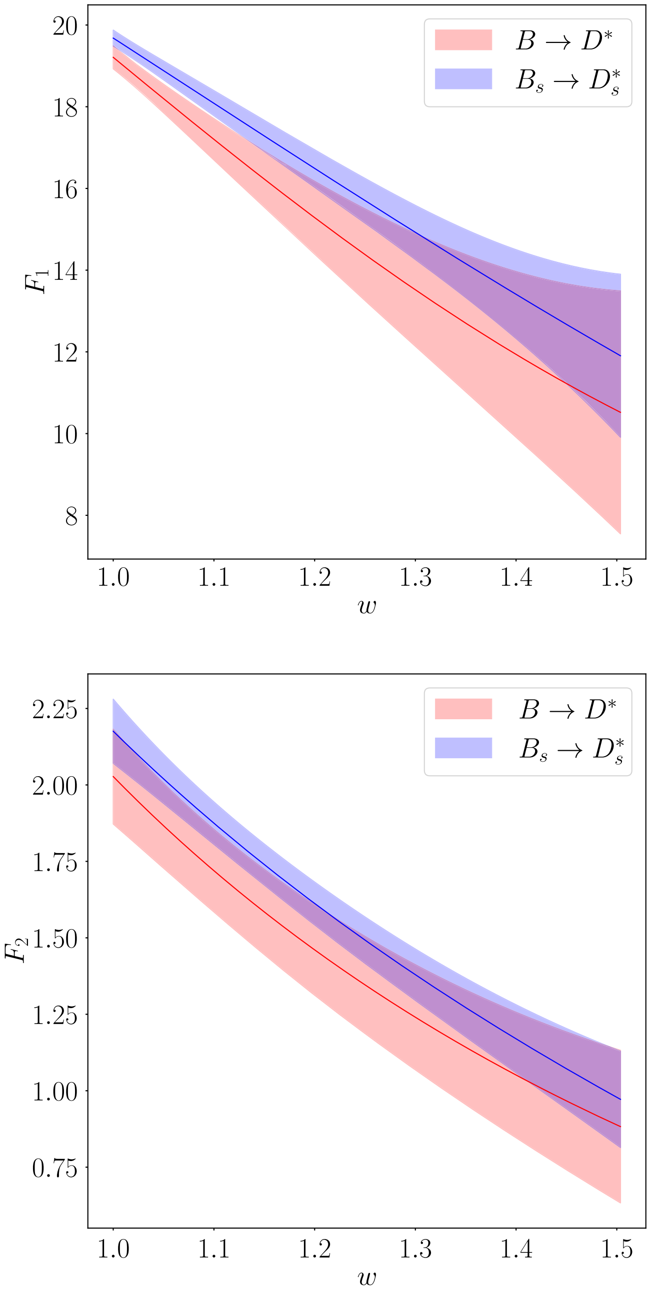

FIG. 14. $B \to D^*$ and $B_s \to D_s^*$ helicity basis form factors F_1 and F_2, defined in Eq. (31).

2. Tensor operator

Of the models considered in [70] only S_1 and R_2 produced a nonzero tensor coupling. These models also produced a

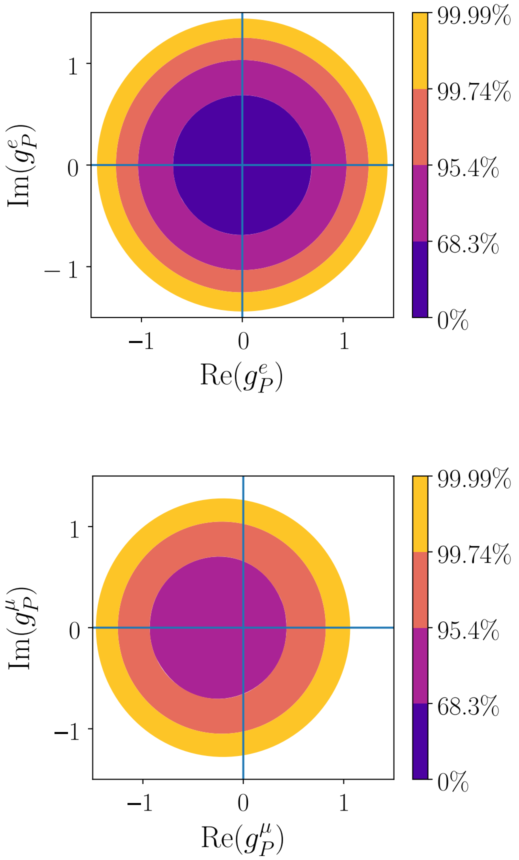

FIG. 15. The top (bottom) plot shows the constraints on $g_P^{e(\mu)}$ using our theory-only differential decay rate and the data for $B^0 \to D^{*-} e^+(\mu^+)\nu_{e(\mu)}$ from Belle [21] for different combinations of $g_P^{e(\mu)}$ and V_{cb}. The different shaded regions correspond to the confidence level to which those values are excluded with intervals of $p = 0\%, 68.3\%, 95.4\%, 99.7\%, 99.99\%$. The unshaded regions of the plot have $p > 99.99\%$. The vertical and horizontal blue lines correspond to the SM value.

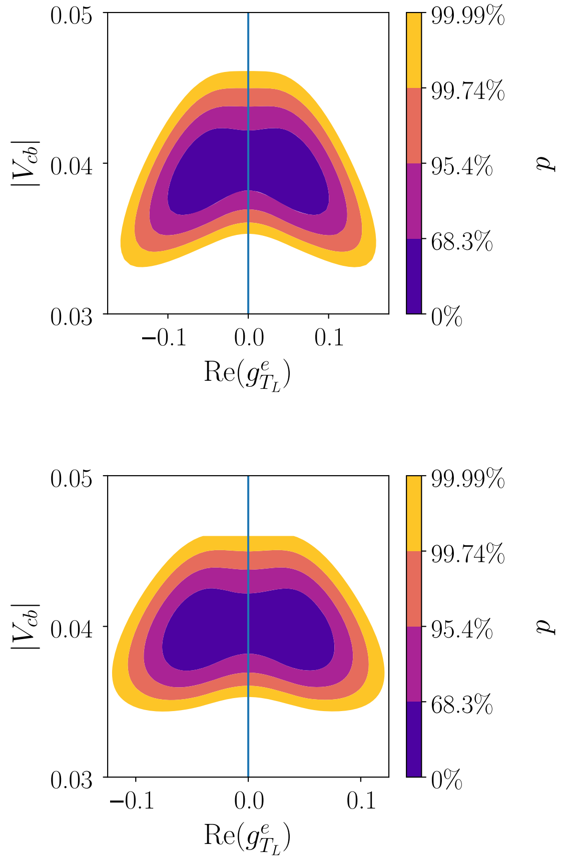

FIG. 16. Tension between our theory-only differential decay rate and the data for $B^0 \to D^{*-} e^+\nu_e$ from Belle [21] for different combinations of $\mathrm{Re}(g_{T_L}^e)$ and V_{cb}. The top (bottom) plot corresponds to the $g_P \approx +(-)4g_{T_L}$ case described in the text. The different shaded regions correspond to the confidence level to which those values are excluded with intervals of $p = 0\%, 68.3\%, 95.4\%, 99.7\%, 99.99\%$. The unshaded regions of the plot have $p > 99.99\%$. The vertical blue line corresponds to the SM value.

correlated nonzero left-handed scalar operator, with $g_{S_L} = \pm 4 g_T$. Based on the expectation that renormalization group mixing effects will leave the relations between left-handed scalar and tensor couplings approximately intact [70], we include the pseudoscalar as a Gaussian random variable with central value $\pm 4 g_T$ and uncertainty $\pm 10\%$.

For the $\ell = e$ case the terms proportional to m_ℓ^2/q^2 and $\sqrt{m_\ell^2/q^2}$ may be neglected. Then the only relevant combinations of helicity amplitudes are those appearing in Table XVI. These do not mix the tensor or pseudoscalar helicity amplitudes with the helicity amplitudes for the SM currents. For the $\ell = e$ mode we can then only determine constraints on the relative phase of g_P and g_{T_L}. Since we fix $g_P = \pm 4 g_{T_L}$, we may look at just the real part of g_{T_L}, together with the value of $|V_{cb}|$. The constraints for both $g_P = \pm 4 g_{T_L}$ cases for $\ell = e$ are shown in Fig. 16, where we see that the constraints in the $g_P = -4 g_{T_L}$ case are similar to the $g_P = +4 g_{T_L}$ case.

The situation for $\ell = \mu$ is more complicated. In the SM the lepton-mass-suppressed terms have factors m_ℓ^2/q^2 but in NP scenarios combinations of the SM and NP helicity amplitudes appear at order $\sqrt{m_\ell^2/q^2}$. This contribution can be significant for $\ell = \mu$, depending on the size of $g_{T_L}^\mu$, and so we cannot remove the overall phase and must consider both the real and imaginary parts of $g_{T_L}^\mu$. The resulting constraint, using only the normalized differential rate, which is insensitive to V_{cb}, is shown in Fig. 17, where we see that the Belle $B^0 \to D^{*-}\mu^+\nu_\mu$ data is consistent with $g_{T_L}^\mu = 0$ at the level of $\approx 1\sigma$.

3. *Right-handed vector operator*

The constraints on the right-handed vector coupling, $g_{V_R}^\ell$, computed using our lattice results and the Belle data are shown in Fig. 18 for the $\ell = e$ and $\ell = \mu$ cases, where we also see no strong preference for a nonzero value.

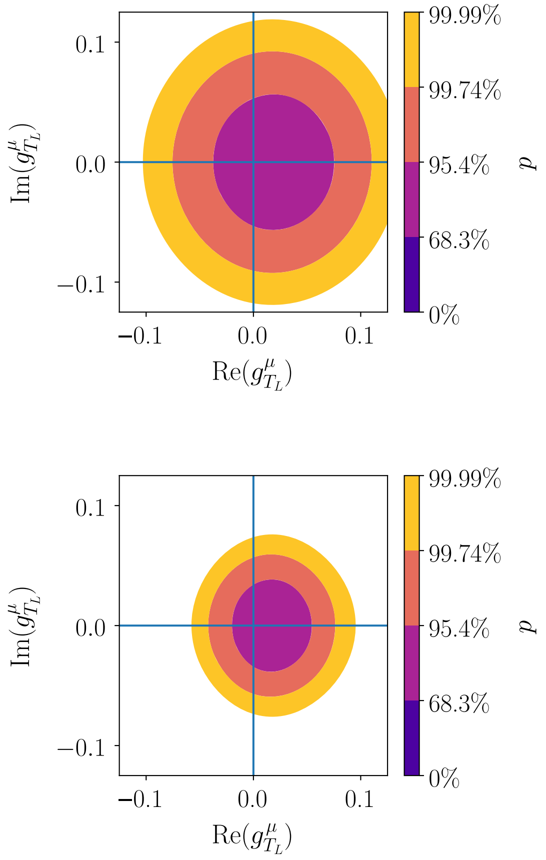

FIG. 17. Tension between our theory-only differential decay rate and the data for $B^0 \to D^{*-}\mu^+\nu_\mu$ from Belle [21] for different combinations of $\mathrm{Re}(g^{\mu}_{T_L})$ and V_{cb}. The top (bottom) plot corresponds to the $g_P \approx +(-)4g_{T_L}$ case described in the text. The different shaded regions correspond to the confidence level to which those values are excluded with intervals of $p = 0\%, 68.3\%, 95.4\%, 99.7\%, 99.99\%$. The unshaded regions of the plot have $p > 99.99\%$. The vertical and horizontal blue line corresponds to the SM value.

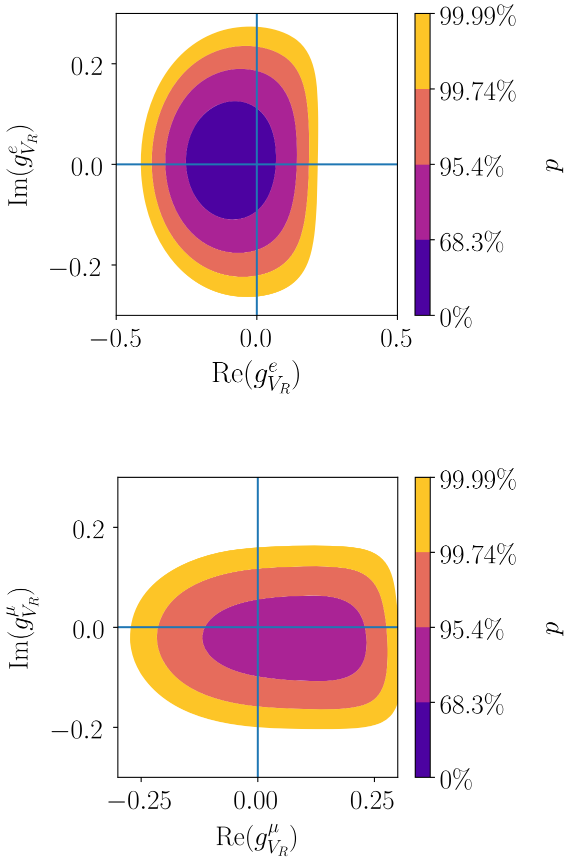

FIG. 18. The top (bottom) plot shows the constraints on $g_P^{e(\mu)}$ using our theory-only differential decay rate and the data for $B^0 \to D^{*-}e^+(\mu^+)\nu_{e(\mu)}$ from Belle [21] for different combinations of $g_{V_R}^{e(\mu)}$. The different shaded regions correspond to the confidence level to which those values are excluded with intervals of $p = 0\%, 68.3\%, 95.4\%, 99.7\%, 99.99\%$. The unshaded regions of the plot have $p > 99.99\%$. The vertical blue line corresponds to the SM value.

E. $V_{cb}^{e(\mu)}$, ΔA_{FB}

A clear feature of the constraints produced is that the $\ell = \mu$ data does not agree well with our SM predictions, compared to the $\ell = e$ case, for any values of the couplings considered. Having reconstructed the full 80×80 Belle covariance matrix as described in Sec. V A, we may compute a value of V_{cb} using $\ell = e$ and $\ell = \mu$ separately and calculate their difference including correlations. We find

$$V^{e}_{cb} = 39.26(91) \times 10^{-3},$$
$$V^{\mu}_{cb} = 38.75(96) \times 10^{-3}, \tag{46}$$

and

$$V^{e}_{cb}/V^{\mu}_{cb} = 1.013(17), \tag{47}$$

consistent with $V^{e}_{cb}/V^{\mu}_{cb} = 1$ as we would expect in the absence of NP. This is a similar level of consistency as was seen in [70].

In [65] it was found that the 2018 Belle dataset was inconsistent with the SM prediction for $\Delta A_{FB} = \langle A^{\mu}_{FB}\rangle - \langle A^{e}_{FB}\rangle$, using a combination of HQE, light-cone sum rules, and lattice QCD results for the zero recoil $B \to D^*$ form factor, h_{A_1}, and for the SM $B \to D$ form factors across the full q^2 range. Here, using our lattice-only results, we find

$$\langle A^{\mu}_{FB}\rangle = 0.266(34),$$
$$\langle A^{e}_{FB}\rangle = 0.270(33). \tag{48}$$

This is in tension at the level of $\approx 2.5\sigma$ with the SM results for both $\ell = e$ and $\ell = \mu$ in [65]. We also find

$$\Delta A_{FB} = -0.0036(10). \tag{49}$$

This result is in tension with the SM results in [65] at the level of $\approx 2\sigma$, although note that it is still much smaller than and of opposite sign to the corresponding result using fits to experimental data [65], in tension at the level of 3.5σ.

VI. CONCLUSION

We have computed the $B_{(s)} \to D^*_{(s)}$ form factors for the complete set of vector, axial-vector, and tensor currents needed to describe both SM physics and potential new physics appearing in the effective Hamiltonian, Eq. (3). These form factors include a fully relativistic treatment of both charm and bottom quarks in lattice QCD and span the full kinematic range of the decay. Our calculation includes two sets of gauge configurations with physical up/down quarks, which we use to constrain the chiral dependence in our chiral-continuum extrapolation using the full rooted staggered chiral perturbation theory (see Appendix D).

We have used our form factors to perform the first combined fit to both $B \to D^*$ data, from Belle [21], as well $B_s \to D^*_s$ data, from LHCb [66]. This gives a value of V_{cb}:

$$|V_{cb}| = 39.03(56)_{\mathrm{exp}}(67)_{\mathrm{latt}} \times 10^{-3}. \tag{50}$$

This is in good agreement with other exclusive determinations and confirms the tension seen with inclusive determinations [10]. For our result this tension is at the level of $\approx 3.6\sigma$ with the most recent inclusive value $|V_{cb}| = 42.16(51) \times 10^{-3}$ [5]. We have also determined a less precise value of $V_{cb} = 42.9(0.5)_{\mathrm{exp}}(2.2)_{\mathrm{latt}} \times 10^{-3}$, computed using only the total decay rate. This value is in good agreement with the inclusive result. The significant upward shift can be understood as a result of the observed tension between our results for the shape of the differential decay rate and the experimental data from Belle. This tension is similar to the tension seen by the Fermilab-MILC collaboration using their lattice QCD form factors, determined using a different formalism for b and c quarks [26]. A tension in the shape of the differential decay rate to light leptons is difficult to explain, since new physics is only expected to appear in the semitauonic mode. We have also computed the slope of $\mathcal{F}$, defined in Eq. (36), and plotted $|\mathcal{F} V_{cb} \eta_{\mathrm{EW}}|^2$ in Fig. 11, where the difference in shape is visible.

We have also used our form factors to compute the phenomenologically important quantities, $R^{(\mathrm{imp})}(D^*_{(s)})$, $\langle \mathcal{A}^{(s)}_{\lambda_\tau} \rangle$, $\langle F_L^{D^*_{(s)}} \rangle$, and $\langle \mathcal{A}^{(s)}_{\mathrm{FB}} \rangle$, given in Table XV and Eqs. (41) and (42), respectively. We find our value of $R(D^*) = 0.273(15)$ is in good agreement with the latest experimental measurements from Belle and LHCb [34,35], and with the most recent HFLAV average [10]. However, our value of the semitauonic D^* longitudinal polarization fraction is in tension with the recent Belle measurement [39] at the level of 2.2σ. We have also determined a lattice + experiment value of $R(D^*) = 0.2482(20)$, computed using the form factors resulting from the fit to both our lattice results and the experimental data from Belle, described in Sec. V A. The downward shift of the value of $R(D^*)$ when including the experimental differential rate data means that this lower value is in tension at the level of 3σ with the HFLAV average for $R(D^*)$. So we see that the "$R(D^*)$ anomaly," like the "V_{cb} puzzle," arises from the inclusion of the experimental differential rate data.

The inclusion of $B_s \to D^*_s$ correlators in our lattice calculation has allowed us to perform a simultaneous fit to both modes, using a parametrization allowing for $SU(3)_{\mathrm{flav}}$-breaking effects at the very conservative level of $\approx 25\%$. Using this fit, we provide updated $B_s \to D^*_s$ form factors that supersede those from our earlier calculation [23]. We find the additional data and chiral information used here, as well as changes to correlator fitting procedures and extrapolation method, result in $B_s \to D^*_s$ form factors which are compatible with our previous results for the less noisy form factors h_{A_1} and h_V but in some tension for the more noisy form factors h_{A_2} and h_{A_3}. The updated results here are substantially more precise particularly for h_{A_1} and h_V close to $w = 1$ where we see an improvement in precision by a factor of ≈ 2. We have used our updated $B_s \to D^*_s$ form factors to investigate $SU(3)_{\mathrm{flav}}$ symmetry breaking effects appearing in $R^{(\mathrm{imp})}(D^*_{(s)})$, $\langle \mathcal{A}^{(s)}_{\lambda_\tau} \rangle$, $\langle F_L^{D^*_{(s)}} \rangle$, and $\langle \mathcal{A}^{(s)}_{\mathrm{FB}} \rangle$. In each observable we find that the $B \to D^*$ differs by $+0.6(1.4)\%$, $+4.0(2.9)\%$, $-5.8(4.6)\%$, and $+19.0(23.0)\%$, respectively, from the $B_s \to D^*_s$ value.

We have used our form factors to generate synthetic data points which we fit using the popular BGL parametrization, which we found gave a good fit with the unitarity bounds far from saturation. Our fitted BGL parameters agree well with those in [26] for f, g, and F_1 but for the form factor F_2, corresponding to the pseudoscalar current, are in significant disagreement. Note that in decay rates F_2 is suppressed by the square of the lepton mass and so only contributes to the semitauonic mode.

Finally we examined the constraints on the NP couplings for the $\ell = \mu/e$ modes resulting from combining our lattice results with the 2018 untagged Belle dataset. We found that none of the couplings, when varied in the combinations described in Sec. V D, strongly preferred values different from the SM ones. We used our results to compute SM values for $\langle \mathcal{A}_{\mathrm{FB}} \rangle$ for both $\ell = \mu/e$ modes. Our values differ from the SM predictions given in [65] using a combination of light-cone sum rules, HQE, and lattice QCD results, at the level of 2.5σ. We also computed the difference, $\Delta A_{FB} = \langle A^{\mu}_{FB} \rangle - \langle A^{e}_{FB} \rangle$, and found a value different to that given in [65] by $\approx 2\sigma$, and in tension with fits to the 2018 Belle data at the level of 3.5σ. This result confirms the need for further investigation of lepton flavor universality violating effects in the $\ell = \mu/e$ modes of the decay.

This work demonstrates the feasibility of computing a complete set of fully correlated SM and NP form factors for pseudoscalar to vector semileptonic decays using the heavy-HISQ approach, across different chiral regimes. Our calculation has allowed us to perform the first simultaneous analysis of data for $B \to D^*$ together with data for $B_s \to D_s^*$, paving the way for the analysis of more precise experimental data that is expected from LHCb and Belle II in these channels in the near future.

ACKNOWLEDGMENTS

We are grateful to the MILC collaboration for the use of their configurations and code. We thank C. Bouchard, B. Colquhoun, J. Koponen, P. Lepage, E. McLean, C. McNeile, and A. Vaquero for useful discussions. Computing was done on the Cambridge service for Data Driven Discovery (CSD3), part of which is operated by the University of Cambridge Research Computing on behalf of the DIRAC HPC Facility of the Science and Technology Facilities Council (STFC). The DIRAC component of CSD3 was funded by BEIS capital funding via STFC capital Grants No. ST/P002307/1 and No. ST/R002452/1 and by STFC operations Grant No. ST/R00689X/1. DiRAC is part of the national e-infrastructure. We are grateful to the CSD3 support staff for assistance. Funding for this work came from U.K. Science and Technology Facilities Council Grant No. ST/P000746/1 and Engineering and Physical Sciences Research Council Project No. EP/W005395/1.

APPENDIX A: FULL DIFFERENTIAL DECAY RATE INCLUDING TENSOR OPERATORS

The matrix element $\mathcal{M}$ is given by

$$\mathcal{M}^{\lambda_{D^*}\lambda_\ell} = C\langle D\pi|D^*(\lambda_{D^*})\rangle\langle D^*(\lambda_{D^*})|J^{\mathrm{had}}_\alpha|B\rangle \times \langle \ell(\lambda_\ell)\bar{\nu}|J^{\mathrm{lep}\alpha}|0\rangle, \tag{A1}$$

where $C^{-1} = g_{D^*D\pi}|\vec{p}_\pi|$ is a constant normalization, with $\vec{p}_\pi$ the pion spatial momentum in the D^* rest frame, such that integrating over $D\pi$ phase space yields the rate for our choice of overall normalization $N(q^2)$ including the $D^* \to D\pi$ branching fraction in Eq. (4). The sum on α includes scalar, vector, and tensorlike currents,

$$\sum_\alpha J^{\mathrm{had}}_\alpha J^{\mathrm{lep}\alpha} = g_{S(P)} J^{\mathrm{had}_{S(P)}} J^{\mathrm{lep}_{S(P)}} + g_{V(A)} J^{\mathrm{had}_{V(A)}}_\mu J^{\mathrm{lep}_{V(A)}\mu} + g_{T(T5)} J^{\mathrm{had}_{T(T5)}}_{\mu\nu} J^{\mathrm{lep}_{T(T5)}\mu\nu}. \tag{A2}$$

It is conventional to insert off-shell vector boson polarization vectors in order to define *helicity amplitudes*. These polarization vectors, $\bar{\epsilon}(\lambda)$, possess the property that

$$\sum_\lambda \bar{\epsilon}_\mu(\lambda)^* \bar{\epsilon}_\nu(\lambda)\delta_\lambda = g_{\mu\nu} \tag{A3}$$

with $\delta_{0,\pm} = -1$ and $\delta_t = 1$. We use vector boson polarization vectors in the W rest frame,

$$\bar{\epsilon}^\mu(\lambda = t) = \begin{pmatrix} 1 \\ 0 \\ 0 \\ 0 \end{pmatrix}, \qquad \bar{\epsilon}^\mu(\lambda = 0) = \begin{pmatrix} 0 \\ 0 \\ 0 \\ -1 \end{pmatrix},$$

$$\bar{\epsilon}^\mu(\lambda = \pm) = \pm\frac{1}{\sqrt{2}}\begin{pmatrix} 0 \\ -1 \\ \pm i \\ 0 \end{pmatrix} \tag{A4}$$

and D^* polarization vectors in the D^* rest frame

$$\epsilon^\mu(\lambda = \pm) = \pm\frac{1}{\sqrt{2}}\begin{pmatrix} 0 \\ -1 \\ \mp i \\ 0 \end{pmatrix}, \quad \epsilon^\mu(\lambda = 0) = \begin{pmatrix} 0 \\ 0 \\ 0 \\ 1 \end{pmatrix}. \tag{A5}$$

In the B rest frame the polarization vectors are

$$\bar{\epsilon}^\mu(\lambda = t) = \frac{1}{\sqrt{q^2}}\begin{pmatrix} q_0 \\ 0 \\ 0 \\ -|\vec{q}| \end{pmatrix}, \quad \bar{\epsilon}^\mu(\lambda = 0) = \frac{1}{\sqrt{q^2}}\begin{pmatrix} |\vec{q}| \\ 0 \\ 0 \\ -q_0 \end{pmatrix},$$

$$\bar{\epsilon}^\mu(\lambda = \pm) = \pm\frac{1}{\sqrt{2}}\begin{pmatrix} 0 \\ -1 \\ \pm i \\ 0 \end{pmatrix}, \tag{A6}$$

and

$$\epsilon^\mu(\lambda = \pm) = \pm\frac{1}{\sqrt{2}}\begin{pmatrix} 0 \\ -1 \\ \mp i \\ 0 \end{pmatrix}, \quad \epsilon^\mu(\lambda = 0) = \frac{1}{M^2_{D^*}}\begin{pmatrix} |\vec{q}| \\ 0 \\ 0 \\ E_{D^*} \end{pmatrix}. \tag{A7}$$

We take D, π, ℓ, and ν momenta

$$p_D^\mu = \begin{pmatrix} E_D \\ k\cos(\chi)\sin(\theta_{D^*}) \\ -k\sin(\chi)\sin(\theta_{D^*}) \\ k\cos(\chi) \end{pmatrix},$$

$$p_\pi^\mu = \begin{pmatrix} k \\ -k\cos(\chi)\sin(\theta_{D^*}) \\ k\sin(\chi)\sin(\theta_{D^*}) \\ -k\cos(\chi) \end{pmatrix}, \tag{A8}$$

$$p_\ell^\mu = \begin{pmatrix} E_\ell \\ k'\sin(\theta_W) \\ 0 \\ -k'\cos(\theta_W) \end{pmatrix}, \quad p_\nu^\mu = \begin{pmatrix} k' \\ -k'\sin(\theta_W) \\ 0 \\ k'\cos(\theta_W) \end{pmatrix}. \tag{A9}$$

The leptonic and hadronic helicity amplitudes are defined by

$$\begin{aligned} & g_{V(A)}\langle D^*(\lambda_{D^*})|J_\mu^{\mathrm{had}_{V(A)}}|B\rangle\langle\ell(\lambda_\ell)\bar{\nu}|J^{\mathrm{lep}_{V-A}\mu}|0\rangle \\ &\quad = \sum_\lambda \delta_\lambda g_{V(A)}\langle D^*(\lambda_{D^*})|J_\mu^{\mathrm{had}_{V(A)}}|B\rangle\bar{\epsilon}^\mu(\lambda)^* \\ &\qquad \times \bar{\epsilon}^\nu(\lambda)\langle\ell(\lambda_\ell)\bar{\nu}|J_\nu^{\mathrm{lep}_{V-A}}|0\rangle \\ &\quad = \sum_\lambda \delta_\lambda H_{V(A)}^{\lambda_{D^*},\lambda} L_{V-A}^{\lambda_\ell,\lambda}. \end{aligned} \tag{A10}$$

The expressions for the vector and axial-vector helicity amplitudes, $H^\pm = H_V^{\pm,\pm} + H_A^{\pm,\pm}$, $H_0 = -H_A^{0,0}$, and $H_t = -H_A^{0,t}$, are given in Eq. (7). Note that for the $\lambda = 0, t$ cases, it is conventional to define the helicity amplitude with an additional factor of -1. For the tensor currents, it is conventional to also insert a factor of $i(-i)$:

$$\begin{aligned} & i g_{T(T5)}\langle D^*(\lambda_{D^*})|J_{\mu\nu}^{\mathrm{had}_{T(T5)}}|B\rangle(-i\langle\ell(\lambda_\ell)\bar{\nu}|J^{\mathrm{lep}_{T-T5}\mu\nu}|0\rangle) \\ &\quad = \sum_{\lambda\bar{\lambda}} \delta_\lambda\delta_{\bar{\lambda}} H_{T(T5)}^{\lambda_{D^*},\lambda\bar{\lambda}} L_{T-T5}^{\lambda_\ell,\lambda\bar{\lambda}}. \end{aligned} \tag{A11}$$

Note that the tensor current $J^{\mathrm{had}_{T(T5)}}$ includes a continuum $\overline{\mathrm{MS}}$ renormalization, defined at a scale μ which we take to be $\mu = 4.8$ GeV.

The nonzero tensor helicity amplitudes are, using Eq. (6),

$$\begin{aligned} H_T^{0,+-} &= -H_T^{0,-+} = -g_T\sqrt{M_B M_{D^*}}\big((1+w)h_{T_1} \\ &\qquad + (w-1)h_{T_2} - h_{T_3}(w^2-1)\big) \\ H_T^{\pm,\pm 0} &= -H_T^{\pm,0\pm} = \pm g_T M_B \frac{\sqrt{M_B M_{D^*}}}{\sqrt{q^2}} \\ &\qquad \times \big(h_{T_1}(1-r)(1+w) \\ &\qquad - h_{T_2}(1+r)(w-1)\big) \\ H_T^{\pm,\pm t} &= -H_T^{\pm,t\pm} = \pm g_T M_B \frac{\sqrt{M_B M_{D^*}(w^2-1)}}{\sqrt{q^2}} \\ &\qquad \times \big(h_{T_1}(1+r) - h_{T_2}(1-r)\big). \end{aligned} \tag{A12}$$

For the axial-tensor current, we may use the fact that $\gamma^5\sigma^{\mu\nu} = \frac{i}{2}\varepsilon^{\mu\nu\sigma\rho}\sigma_{\sigma\rho}$ to relate $\langle D^*|\bar{c}\gamma^5\sigma^{\mu\nu}b|B\rangle = \frac{i}{2}\varepsilon^{\mu\nu\sigma\rho}\langle D^*|\bar{c}\sigma_{\sigma\rho}b|B\rangle$. Inserting this into the definition of the helicity amplitudes allows us to relate the axial-tensor helicity amplitudes to the tensor helicity amplitudes:

$$\begin{aligned} H_{T5}^{\pm,\pm 0} &= -H_{T5}^{\pm,0\pm} = \mp\frac{g_{T5}}{g_T}H_T^{\pm,\pm t} \\ H_{T5}^{\pm,\pm t} &= -H_{T5}^{\pm,t\pm} = \mp\frac{g_{T5}}{g_T}H_T^{\pm,\pm 0} \\ H_{T5}^{0,0t} &= -H_{T5}^{0,t0} = -\frac{g_{T5}}{g_T}H_T^{0,+-}. \end{aligned} \tag{A13}$$

The pseudoscalar current is straightforwardly

$$g_P\langle D^*(\lambda_{D^*})|J^{\mathrm{had}_P}|B\rangle\langle\ell(\lambda_\ell)\bar{\nu}|J^{\mathrm{lep}_P}|0\rangle = H_P^{\lambda_{D^*}}L_{S-P}^{\lambda_\ell}. \tag{A14}$$

We can use the partially conserved axial current relation, $\langle D^*|q_\mu\bar{c}\gamma^\mu\gamma^5 b|\bar{B}\rangle = -(m_b+m_c)\langle D^*|\bar{c}\gamma^5 b|\bar{B}\rangle$, to write

$$H_P = H_P^{\lambda_{D^*}=0} = \frac{\sqrt{q^2}}{(m_b+m_c)}\frac{g_P}{g_A}H_t. \tag{A15}$$

Together with the parametrization of the amplitude

$$\langle D\pi|D^*(\lambda_{D^*})\rangle = g_{D^*D\pi}\epsilon_\mu(\lambda_{D^*})p_D^\mu \tag{A16}$$

this gives

$$\begin{aligned} \mathcal{M}^{\lambda_{D^*}\lambda_\ell} &= C g_{D^*D\pi}\epsilon_\mu(\lambda_{D^*})p_D^\mu\big[H_P^{\lambda_{D^*}}L_{S-P}^{\lambda_\ell} \\ &\quad + \sum_\lambda \delta_\lambda\big(H_V^{\lambda_{D^*},\lambda} + H_A^{\lambda_{D^*},\lambda}\big)L_{V-A}^{\lambda_\ell,\lambda} \\ &\quad + \sum_{\lambda\bar{\lambda}}\delta_\lambda\delta_{\bar{\lambda}}\big(H_T^{\lambda_{D^*},\lambda\bar{\lambda}} + H_{T5}^{\lambda_{D^*},\lambda\bar{\lambda}}\big)L_{T-T5}^{\lambda_\ell,\lambda\bar{\lambda}}\big]. \end{aligned} \tag{A17}$$

For the charge conjugate mode, we have

$$g^*_{V(A)}\langle \overline{D^*}(\lambda_{D^*})|J^{\mathrm{had}_{V(A)}\dagger}_{\mu}|\bar{B}\rangle\langle\overline{\ell}(\lambda_\ell)\nu|J^{\mathrm{lep}_{V-A}\mu\dagger}|0\rangle$$

$$= \sum_{\lambda}\delta_\lambda \eta \frac{g^*_{V(A)}}{g_{V(A)}} H^{\lambda_{D^*},\lambda}_{V(A)} L'^{\lambda_\ell,\lambda}_{V-A}, \tag{A18}$$

$$ig^*_{T(T5)}\langle \overline{D^*}(\lambda_{D^*})|J^{\mathrm{had}_{T(T5)}\dagger}_{\mu\nu}|\bar{B}\rangle$$

$$\times\left(-i\langle\overline{\ell}(\lambda_\ell)\nu|J^{\mathrm{lep}_{T-T5}\mu\nu\dagger}|0\rangle\right)$$

$$= \sum_{\lambda\bar{\lambda}}\delta_\lambda\delta_{\bar{\lambda}} \frac{\eta g^*_{T(T5)}}{g_{T(T5)}} H^{\lambda_{D^*},\lambda\bar{\lambda}}_{T(T5)} L'^{\lambda_\ell,\lambda\bar{\lambda}}_{T-T5}, \tag{A19}$$

and

$$g^*_P\langle \overline{D^*}(\lambda_{D^*})|J^{\mathrm{had}_P\dagger}|\bar{B}\rangle\langle\overline{\ell}(\lambda_\ell)\nu|J^{\mathrm{lep}_P\dagger}|0\rangle = \eta\frac{g^*_P}{g_P}H^{\lambda_{D^*}}_P L'^{\lambda_\ell}_{S-P}. \tag{A20}$$

$\eta = \pm 1$ is a phase dependent upon the sign of the current under combined Hermitian conjugation and charge conjugation $\mathcal{C}J^{\mathrm{had}\dagger}_\alpha\mathcal{C}^{-1} = \eta J^{\mathrm{had}}_\alpha$. Specifically for the currents defined in Eq. (3), $P, V, A, T, T5$, this phase is $-1, -1, 1, -1, 1$, respectively.

Inserting these expressions, either for the normal or conjugate mode, into Eq. (4) gives the corresponding differential decay rate in terms of lepton tensors and helicity amplitudes. The lepton tensor combinations may be evaluated straightforwardly using standard spinor identities when summing over polarizations,

$$\sum_{\lambda_\ell} L^{\lambda_\ell}_\gamma (L^{\lambda_\ell}_\Gamma)^* = \sum_{ss'}\langle\ell(s)\bar{\nu}(s')|\overline{\ell}\gamma\nu|0\rangle(\langle\ell(s)\bar{\nu}(s')|\overline{\ell}\Gamma\nu|0\rangle)^\dagger$$

$$= \sum_{ss'}\bar{u}^s(p_\ell)\gamma v^{s'}(p_{\bar{\nu}})\left(\bar{u}^s(p_\ell)\Gamma v^{s'}(p_{\bar{\nu}})\right)^\dagger$$

$$= \sum_{ss'}\bar{u}^s(p_\ell)\gamma v^{s'}(p_{\bar{\nu}})\bar{v}^{s'}(p_{\bar{\nu}})\gamma^0\Gamma^\dagger\gamma^0 u^s(p_\ell)$$

$$= \mathrm{Tr}\left[(\not{p}_\ell + m_\ell)\gamma\not{p}_{\bar{\nu}}\gamma^0\Gamma^\dagger\gamma^0\right]. \tag{A21}$$

For the conjugate mode lepton tensors

$$\sum_{\lambda_\ell} L'^{\lambda_\ell}_\gamma \left(L'^{\lambda_\ell}_\Gamma\right)^*$$

$$= \sum_{ss'}\langle\overline{\ell}(s)\nu(s')|\bar{\nu}\gamma^0\gamma^\dagger\gamma^0\ell|0\rangle$$

$$\times(\langle\overline{\ell}(s)\nu(s')|\bar{\nu}\gamma^0\Gamma^\dagger\gamma^0\ell|0\rangle)^\dagger$$

$$= \sum_{ss'}\bar{u}^{s'}(p_\nu)\gamma^0\gamma^\dagger\gamma^0 v^s(p_\ell)\left(\bar{u}^{s'}(p_\nu)\gamma^0\Gamma^\dagger\gamma^0 v^s(p_\ell)\right)^\dagger$$

$$= \sum_{ss'}\bar{u}^{s'}(p_\nu)\gamma^0\gamma^\dagger\gamma^0 v^s(p_\ell)\bar{v}^s(p_\ell)\Gamma u^{s'}(p_\nu)$$

$$= \mathrm{Tr}\left[\not{p}_\nu\gamma^0\gamma^\dagger\gamma^0\left(\not{p}_\ell - m_\ell\right)\Gamma\right]. \tag{A22}$$

TABLE XVI. The helicity amplitude combinations and coefficients for them that appear in Eq. (10) at order $(m_\ell^2/q^2)^0$ for $B^0 \to D^{*-}\ell^+\nu$.

$\mathcal{H}_i$	$k_i(\theta_W, \theta_{D^*}, \chi)$
$H_T^{0,+-}(H_T^{0,+-})^*$	$16\cos^2(\theta_W)\cos^2(\theta_{D^*})$
$H_T^{0,+-}(H_T^{+,+0})^*$	$2e^{i\chi}\sin(2\theta_W)\sin(2\theta_{D^*})$
$H_T^{0,+-}(H_T^{+,+t})^*$	$-2e^{i\chi}\sin(2\theta_W)\sin(2\theta_{D^*})$
$H_T^{0,+-}(H_T^{-,-0})^*$	$-2e^{-i\chi}\sin(2\theta_W)\sin(2\theta_{D^*})$
$H_T^{0,+-}(H_T^{-,-t})^*$	$-2e^{-i\chi}\sin(2\theta_W)\sin(2\theta_{D^*})$
$H_T^{0,+-}(H_P)^*$	$8\cos(\theta_W)\cos^2(\theta_{D^*})$
$H_T^{+,+0}(H_T^{0,+-})^*$	$2e^{-i\chi}\sin(2\theta_W)\sin(2\theta_{D^*})$
$H_T^{+,+0}(H_T^{+,+0})^*$	$4\sin^2(\theta_W)\sin^2(\theta_{D^*})$
$H_T^{+,+0}(H_T^{+,+t})^*$	$-4\sin^2(\theta_W)\sin^2(\theta_{D^*})$
$H_T^{+,+0}(H_T^{-,-0})^*$	$-4e^{-2i\chi}\sin^2(\theta_W)\sin^2(\theta_{D^*})$
$H_T^{+,+0}(H_T^{-,-t})^*$	$-4e^{-2i\chi}\sin^2(\theta_W)\sin^2(\theta_{D^*})$
$H_T^{+,+0}(H_P)^*$	$2e^{-i\chi}\sin(\theta_W)\sin(2\theta_{D^*})$
$H_T^{+,+t}(H_T^{0,+-})^*$	$-2e^{-i\chi}\sin(2\theta_W)\sin(2\theta_{D^*})$
$H_T^{+,+t}(H_T^{+,+0})^*$	$-4\sin^2(\theta_W)\sin^2(\theta_{D^*})$
$H_T^{+,+t}(H_T^{+,+t})^*$	$4\sin^2(\theta_W)\sin^2(\theta_{D^*})$
$H_T^{+,+t}(H_T^{-,-0})^*$	$4e^{-2i\chi}\sin^2(\theta_W)\sin^2(\theta_{D^*})$
$H_T^{+,+t}(H_T^{-,-t})^*$	$4e^{-2i\chi}\sin^2(\theta_W)\sin^2(\theta_{D^*})$
$H_T^{+,+t}(H_P)^*$	$-2e^{-i\chi}\sin(\theta_W)\sin(2\theta_{D^*})$
$H_T^{-,-0}(H_T^{0,+-})^*$	$-2e^{i\chi}\sin(2\theta_W)\sin(2\theta_{D^*})$
$H_T^{-,-0}(H_T^{+,+0})^*$	$-4e^{2i\chi}\sin^2(\theta_W)\sin^2(\theta_{D^*})$
$H_T^{-,-0}(H_T^{+,+t})^*$	$4e^{2i\chi}\sin^2(\theta_W)\sin^2(\theta_{D^*})$
$H_T^{-,-0}(H_T^{-,-0})^*$	$4\sin^2(\theta_W)\sin^2(\theta_{D^*})$
$H_T^{-,-0}(H_T^{-,-t})^*$	$4\sin^2(\theta_W)\sin^2(\theta_{D^*})$
$H_T^{-,-0}(H_P)^*$	$-2e^{i\chi}\sin(\theta_W)\sin(2\theta_{D^*})$
$H_T^{-,-t}(H_T^{0,+-})^*$	$-2e^{i\chi}\sin(2\theta_W)\sin(2\theta_{D^*})$
$H_T^{-,-t}(H_T^{+,+0})^*$	$-4e^{2i\chi}\sin^2(\theta_W)\sin^2(\theta_{D^*})$
$H_T^{-,-t}(H_T^{+,+t})^*$	$4e^{2i\chi}\sin^2(\theta_W)\sin^2(\theta_{D^*})$
$H_T^{-,-t}(H_T^{-,-0})^*$	$4\sin^2(\theta_W)\sin^2(\theta_{D^*})$
$H_T^{-,-t}(H_T^{-,-t})^*$	$4\sin^2(\theta_W)\sin^2(\theta_{D^*})$
$H_T^{-,-t}(H_P)^*$	$-2e^{i\chi}\sin(\theta_W)\sin(2\theta_{D^*})$
$H_+(H_+)^*$	$4\sin^4(\frac{\theta_W}{2})\sin^2(\theta_{D^*})$
$H_+(H_-)^*$	$-e^{2i\chi}\sin^2(\theta_W)\sin^2(\theta_{D^*})$
$H_+(H_0)^*$	$-2e^{i\chi}\sin^2(\frac{\theta_W}{2})\sin(\theta_W)\sin(2\theta_{D^*})$
$H_-(H_+)^*$	$-e^{-2i\chi}\sin^2(\theta_W)\sin^2(\theta_{D^*})$
$H_-(H_-)^*$	$4\cos^4(\frac{\theta_W}{2})\sin^2(\theta_{D^*})$
$H_-(H_0)^*$	$e^{-i\chi}\sin(\theta_W)(\cos(\theta_W)+1)\sin(2\theta_{D^*})$
$H_0(H_+)^*$	$-2e^{-i\chi}\sin^2(\frac{\theta_W}{2})\sin(\theta_W)\sin(2\theta_{D^*})$
$H_0(H_-)^*$	$e^{i\chi}\sin(\theta_W)(\cos(\theta_W)+1)\sin(2\theta_{D^*})$
$H_0(H_0)^*$	$4\sin^2(\theta_W)\cos^2(\theta_{D^*})$
$H_P(H_T^{0,+-})^*$	$8\cos(\theta_W)\cos^2(\theta_{D^*})$
$H_P(H_T^{+,+0})^*$	$2e^{i\chi}\sin(\theta_W)\sin(2\theta_{D^*})$
$H_P(H_T^{+,+t})^*$	$-2e^{i\chi}\sin(\theta_W)\sin(2\theta_{D^*})$
$H_P(H_T^{-,-0})^*$	$-2e^{-i\chi}\sin(\theta_W)\sin(2\theta_{D^*})$
$H_P(H_T^{-,-t})^*$	$-2e^{-i\chi}\sin(\theta_W)\sin(2\theta_{D^*})$
$H_P(H_P)^*$	$4\cos^2(\theta_{D^*})$

The combinations of helicity amplitudes and k_i factors entering the squared matrix element, Eq. (10), for general complex choices of g_X in Eq. (3), are given in Tables XVI–XVIII for the conjugate mode $B^0 \to D^{*-}\ell^+\nu$. Note that these include the factor η, and so should be used with the helicity amplitudes for $B^0 \to D^{*+}\ell^-\bar{\nu}$, just taking $g_X \to g_X^*$. We have checked explicitly that our method of constructing the differential decay rate reproduces the

TABLE XVII. The helicity amplitude combinations and coefficients for them that appear in Eq. (10) at order $(m_\ell^2/q^2)^{\frac{1}{2}}$ for $B^0 \to D^{*-}\ell^+\nu$.

$\mathcal{H}_i$	$k_i(\theta_W, \theta_{D^*}, \chi)$
$\sqrt{\frac{m_\ell^2}{q^2}} H_T^{0,+-}(H_+)^*$	$-2e^{-i\chi}\sin(\theta_W)\sin(2\theta_{D^*})$
$\sqrt{\frac{m_\ell^2}{q^2}} H_T^{0,+-}(H_-)^*$	$2e^{i\chi}\sin(\theta_W)\sin(2\theta_{D^*})$
$\sqrt{\frac{m_\ell^2}{q^2}} H_T^{0,+-}(H_0)^*$	$8\cos^2(\theta_{D^*})$
$\sqrt{\frac{m_\ell^2}{q^2}} H_T^{0,+-}(H_t)^*$	$-8\cos(\theta_W)\cos^2(\theta_{D^*})$
$\sqrt{\frac{m_\ell^2}{q^2}} H_T^{+,+0}(H_-)^*$	$-8\cos^2(\frac{\theta_W}{2})\sin^2(\theta_{D^*})$
$\sqrt{\frac{m_\ell^2}{q^2}} H_T^{+,+0}(H_0)^*$	$-2e^{-i\chi}\sin(\theta_W)\sin(2\theta_{D^*})$
$\sqrt{\frac{m_\ell^2}{q^2}} H_T^{+,+0}(H_t)^*$	$-2e^{-i\chi}\sin(\theta_W)\sin(2\theta_{D^*})$
$\sqrt{\frac{m_\ell^2}{q^2}} H_T^{+,+t}(H_-)^*$	$8\cos^2(\frac{\theta_W}{2})\sin^2(\theta_{D^*})$
$\sqrt{\frac{m_\ell^2}{q^2}} H_T^{+,+t}(H_0)^*$	$2e^{-i\chi}\sin(\theta_W)\sin(2\theta_{D^*})$
$\sqrt{\frac{m_\ell^2}{q^2}} H_T^{+,+t}(H_t)^*$	$2e^{-i\chi}\sin(\theta_W)\sin(2\theta_{D^*})$
$\sqrt{\frac{m_\ell^2}{q^2}} H_T^{-,-0}(H_+)^*$	$8\sin^2(\frac{\theta_W}{2})\sin^2(\theta_{D^*})$
$\sqrt{\frac{m_\ell^2}{q^2}} H_T^{-,-0}(H_0)^*$	$-2e^{i\chi}\sin(\theta_W)\sin(2\theta_{D^*})$
$\sqrt{\frac{m_\ell^2}{q^2}} H_T^{-,-0}(H_t)^*$	$2e^{i\chi}\sin(\theta_W)\sin(2\theta_{D^*})$
$\sqrt{\frac{m_\ell^2}{q^2}} H_T^{-,-t}(H_+)^*$	$8\sin^2(\frac{\theta_W}{2})\sin^2(\theta_{D^*})$
$\sqrt{\frac{m_\ell^2}{q^2}} H_T^{-,-t}(H_0)^*$	$-2e^{i\chi}\sin(\theta_W)\sin(2\theta_{D^*})$
$\sqrt{\frac{m_\ell^2}{q^2}} H_T^{-,-t}(H_t)^*$	$2e^{i\chi}\sin(\theta_W)\sin(2\theta_{D^*})$
$\sqrt{\frac{m_\ell^2}{q^2}} H_+(H_T^{0,+-})^*$	$-2e^{i\chi}\sin(\theta_W)\sin(2\theta_{D^*})$
$\sqrt{\frac{m_\ell^2}{q^2}} H_+(H_T^{-,-0})^*$	$8\sin^2(\frac{\theta_W}{2})\sin^2(\theta_{D^*})$
$\sqrt{\frac{m_\ell^2}{q^2}} H_+(H_T^{-,-t})^*$	$8\sin^2(\frac{\theta_W}{2})\sin^2(\theta_{D^*})$
$\sqrt{\frac{m_\ell^2}{q^2}} H_+(H_P)^*$	$-e^{i\chi}\sin(\theta_W)\sin(2\theta_{D^*})$
$\sqrt{\frac{m_\ell^2}{q^2}} H_-(H_T^{0,+-})^*$	$2e^{-i\chi}\sin(\theta_W)\sin(2\theta_{D^*})$
$\sqrt{\frac{m_\ell^2}{q^2}} H_-(H_T^{+,+0})^*$	$-8\cos^2(\frac{\theta_W}{2})\sin^2(\theta_{D^*})$
$\sqrt{\frac{m_\ell^2}{q^2}} H_-(H_T^{+,+t})^*$	$8\cos^2(\frac{\theta_W}{2})\sin^2(\theta_{D^*})$
$\sqrt{\frac{m_\ell^2}{q^2}} H_-(H_P)^*$	$-e^{-i\chi}\sin(\theta_W)\sin(2\theta_{D^*})$
$\sqrt{\frac{m_\ell^2}{q^2}} H_0(H_T^{0,+-})^*$	$8\cos^2(\theta_{D^*})$
$\sqrt{\frac{m_\ell^2}{q^2}} H_0(H_T^{+,+0})^*$	$-2e^{i\chi}\sin(\theta_W)\sin(2\theta_{D^*})$
$\sqrt{\frac{m_\ell^2}{q^2}} H_0(H_T^{+,+t})^*$	$2e^{i\chi}\sin(\theta_W)\sin(2\theta_{D^*})$
$\sqrt{\frac{m_\ell^2}{q^2}} H_0(H_T^{-,-0})^*$	$-2e^{-i\chi}\sin(\theta_W)\sin(2\theta_{D^*})$
$\sqrt{\frac{m_\ell^2}{q^2}} H_0(H_T^{-,-t})^*$	$-2e^{-i\chi}\sin(\theta_W)\sin(2\theta_{D^*})$
$\sqrt{\frac{m_\ell^2}{q^2}} H_0(H_P)^*$	$4\cos(\theta_W)\cos^2(\theta_{D^*})$
$\sqrt{\frac{m_\ell^2}{q^2}} H_t(H_T^{0,+-})^*$	$-8\cos(\theta_W)\cos^2(\theta_{D^*})$
$\sqrt{\frac{m_\ell^2}{q^2}} H_t(H_T^{+,+0})^*$	$-2e^{i\chi}\sin(\theta_W)\sin(2\theta_{D^*})$
$\sqrt{\frac{m_\ell^2}{q^2}} H_t(H_T^{+,+t})^*$	$2e^{i\chi}\sin(\theta_W)\sin(2\theta_{D^*})$
$\sqrt{\frac{m_\ell^2}{q^2}} H_t(H_T^{-,-0})^*$	$2e^{-i\chi}\sin(\theta_W)\sin(2\theta_{D^*})$
$\sqrt{\frac{m_\ell^2}{q^2}} H_t(H_T^{-,-t})^*$	$2e^{-i\chi}\sin(\theta_W)\sin(2\theta_{D^*})$
$\sqrt{\frac{m_\ell^2}{q^2}} H_t(H_P)^*$	$-4\cos^2(\theta_{D^*})$
$\sqrt{\frac{m_\ell^2}{q^2}} H_P(H_+)^*$	$-e^{-i\chi}\sin(\theta_W)\sin(2\theta_{D^*})$
$\sqrt{\frac{m_\ell^2}{q^2}} H_P(H_-)^*$	$-e^{i\chi}\sin(\theta_W)\sin(2\theta_{D^*})$
$\sqrt{\frac{m_\ell^2}{q^2}} H_P(H_0)^*$	$4\cos(\theta_W)\cos^2(\theta_{D^*})$
$\sqrt{\frac{m_\ell^2}{q^2}} H_P(H_t)^*$	$-4\cos^2(\theta_{D^*})$

TABLE XVIII. The helicity amplitude combinations and coefficients for them that appear in Eq. (10) at order m_ℓ^2/q^2 for $B^0 \to D^{*-}\ell^+\nu$.

$\mathcal{H}_i$	$k_i(\theta_W, \theta_{D^*}, \chi)$
$\frac{m_\ell^2}{q^2} H_T^{0,+-}(H_T^{0,+-})^*$	$16\sin^2(\theta_W)\cos^2(\theta_{D^*})$
$\frac{m_\ell^2}{q^2} H_T^{0,+-}(H_T^{+,+0})^*$	$-4e^{i\chi}\sin(\theta_W)(\cos(\theta_W)+1)\sin(2\theta_{D^*})$
$\frac{m_\ell^2}{q^2} H_T^{0,+-}(H_T^{+,+t})^*$	$4e^{i\chi}\sin(\theta_W)(\cos(\theta_W)+1)\sin(2\theta_{D^*})$
$\frac{m_\ell^2}{q^2} H_T^{0,+-}(H_T^{-,-0})^*$	$-8e^{-i\chi}\sin^2(\frac{\theta_W}{2})\sin(\theta_W)\sin(2\theta_{D^*})$
$\frac{m_\ell^2}{q^2} H_T^{0,+-}(H_T^{-,-t})^*$	$-8e^{-i\chi}\sin^2(\frac{\theta_W}{2})\sin(\theta_W)\sin(2\theta_{D^*})$
$\frac{m_\ell^2}{q^2} H_T^{+,+0}(H_T^{0,+-})^*$	$-4e^{-i\chi}\sin(\theta_W)(\cos(\theta_W)+1)\sin(2\theta_{D^*})$
$\frac{m_\ell^2}{q^2} H_T^{+,+0}(H_T^{+,+0})^*$	$16\cos^4(\frac{\theta_W}{2})\sin^2(\theta_{D^*})$
$\frac{m_\ell^2}{q^2} H_T^{+,+0}(H_T^{+,+t})^*$	$-16\cos^4(\frac{\theta_W}{2})\sin^2(\theta_{D^*})$
$\frac{m_\ell^2}{q^2} H_T^{+,+0}(H_T^{-,-0})^*$	$4e^{-2i\chi}\sin^2(\theta_W)\sin^2(\theta_{D^*})$
$\frac{m_\ell^2}{q^2} H_T^{+,+0}(H_T^{-,-t})^*$	$4e^{-2i\chi}\sin^2(\theta_W)\sin^2(\theta_{D^*})$
$\frac{m_\ell^2}{q^2} H_T^{+,+t}(H_T^{0,+-})^*$	$4e^{-i\chi}\sin(\theta_W)(\cos(\theta_W)+1)\sin(2\theta_{D^*})$
$\frac{m_\ell^2}{q^2} H_T^{+,+t}(H_T^{+,+0})^*$	$-16\cos^4(\frac{\theta_W}{2})\sin^2(\theta_{D^*})$

(Table continued)

TABLE XVIII. *(Continued)*

$\mathcal{H}_i$	$k_i(\theta_W, \theta_{D^*}, \chi)$
$\frac{m_\ell^2}{q^2} H_T^{+,+t}(H_T^{+,+t})^*$	$16\cos^4(\frac{\theta_W}{2})\sin^2(\theta_{D^*})$
$\frac{m_\ell^2}{q^2} H_T^{+,+t}(H_T^{-,-0})^*$	$-4e^{-2i\chi}\sin^2(\theta_W)\sin^2(\theta_{D^*})$
$\frac{m_\ell^2}{q^2} H_T^{+,+t}(H_T^{-,-t})^*$	$-4e^{-2i\chi}\sin^2(\theta_W)\sin^2(\theta_{D^*})$
$\frac{m_\ell^2}{q^2} H_T^{-,-0}(H_T^{0,+-})^*$	$-8e^{i\chi}\sin^2(\frac{\theta_W}{2})\sin(\theta_W)\sin(2\theta_{D^*})$
$\frac{m_\ell^2}{q^2} H_T^{-,-0}(H_T^{+,+0})^*$	$4e^{2i\chi}\sin^2(\theta_W)\sin^2(\theta_{D^*})$
$\frac{m_\ell^2}{q^2} H_T^{-,-0}(H_T^{+,+t})^*$	$-4e^{2i\chi}\sin^2(\theta_W)\sin^2(\theta_{D^*})$
$\frac{m_\ell^2}{q^2} H_T^{-,-0}(H_T^{-,-0})^*$	$16\sin^4(\frac{\theta_W}{2})\sin^2(\theta_{D^*})$
$\frac{m_\ell^2}{q^2} H_T^{-,-0}(H_T^{-,-t})^*$	$16\sin^4(\frac{\theta_W}{2})\sin^2(\theta_{D^*})$
$\frac{m_\ell^2}{q^2} H_T^{-,-t}(H_T^{0,+-})^*$	$-8e^{i\chi}\sin^2(\frac{\theta_W}{2})\sin(\theta_W)\sin(2\theta_{D^*})$
$\frac{m_\ell^2}{q^2} H_T^{-,-t}(H_T^{+,+0})^*$	$4e^{2i\chi}\sin^2(\theta_W)\sin^2(\theta_{D^*})$
$\frac{m_\ell^2}{q^2} H_T^{-,-t}(H_T^{+,+t})^*$	$-4e^{2i\chi}\sin^2(\theta_W)\sin^2(\theta_{D^*})$
$\frac{m_\ell^2}{q^2} H_T^{-,-t}(H_T^{-,-0})^*$	$16\sin^4(\frac{\theta_W}{2})\sin^2(\theta_{D^*})$
$\frac{m_\ell^2}{q^2} H_T^{-,-t}(H_T^{-,-t})^*$	$16\sin^4(\frac{\theta_W}{2})\sin^2(\theta_{D^*})$
$\frac{m_\ell^2}{q^2} H_+(H_+)^*$	$\sin^2(\theta_W)\sin^2(\theta_{D^*})$
$\frac{m_\ell^2}{q^2} H_+(H_-)^*$	$e^{2i\chi}\sin^2(\theta_W)\sin^2(\theta_{D^*})$
$\frac{m_\ell^2}{q^2} H_+(H_0)^*$	$-\frac{1}{2}e^{i\chi}\sin(2\theta_W)\sin(2\theta_{D^*})$
$\frac{m_\ell^2}{q^2} H_+(H_t)^*$	$e^{i\chi}\sin(\theta_W)\sin(2\theta_{D^*})$
$\frac{m_\ell^2}{q^2} H_-(H_+)^*$	$e^{-2i\chi}\sin^2(\theta_W)\sin^2(\theta_{D^*})$
$\frac{m_\ell^2}{q^2} H_-(H_-)^*$	$\sin^2(\theta_W)\sin^2(\theta_{D^*})$
$\frac{m_\ell^2}{q^2} H_-(H_0)^*$	$-\frac{1}{2}e^{-i\chi}\sin(2\theta_W)\sin(2\theta_{D^*})$
$\frac{m_\ell^2}{q^2} H_-(H_t)^*$	$e^{-i\chi}\sin(\theta_W)\sin(2\theta_{D^*})$
$\frac{m_\ell^2}{q^2} H_0(H_+)^*$	$-\frac{1}{2}e^{-i\chi}\sin(2\theta_W)\sin(2\theta_{D^*})$
$\frac{m_\ell^2}{q^2} H_0(H_-)^*$	$-\frac{1}{2}e^{i\chi}\sin(2\theta_W)\sin(2\theta_{D^*})$
$\frac{m_\ell^2}{q^2} H_0(H_0)^*$	$4\cos^2(\theta_W)\cos^2(\theta_{D^*})$
$\frac{m_\ell^2}{q^2} H_0(H_t)^*$	$-4\cos(\theta_W)\cos^2(\theta_{D^*})$
$\frac{m_\ell^2}{q^2} H_t(H_+)^*$	$e^{-i\chi}\sin(\theta_W)\sin(2\theta_{D^*})$
$\frac{m_\ell^2}{q^2} H_t(H_-)^*$	$e^{i\chi}\sin(\theta_W)\sin(2\theta_{D^*})$
$\frac{m_\ell^2}{q^2} H_t(H_0)^*$	$-4\cos(\theta_W)\cos^2(\theta_{D^*})$
$\frac{m_\ell^2}{q^2} H_t(H_t)^*$	$4\cos^2(\theta_{D^*})$

results of [36]. Note, however, that in [36] H_t and H_0 are defined without the additional (-1), and also that our angular conventions for the lepton angle are related by $\theta_W \to \pi - \theta_W$. The full differential decay rate is also available in a slightly more compact notation in [71], though the notation here makes clear which helicity amplitudes are suppressed by the lepton mass.

Because

$$(\bar{c}\gamma^5\sigma_{\mu\nu}b)(\overline{\ell}_R\sigma^{\mu\nu}\nu_L) = -(\bar{c}\sigma_{\mu\nu}b)(\overline{\ell}_R\sigma^{\mu\nu}\nu_L), \tag{A23}$$

the g_{T5} term is redundant, and it is typical to identify $(g_T - g_{T5}) \equiv 2g_{T_L}$. As such, we may replace $g_T \to 2g_{T_L}$ and $g_{T5} \to 0$ in Eqs. (A12) and (A13), respectively, and omit the helicity combinations including H_{T5}.

APPENDIX B: n_t BINNING STRATEGY

On each gauge configuration we compute multiple instances of each correlation function, with n_t sources placed at different values of $t_{\rm src}$, spaced equally across the time extent of a given configuration. The values of n_t used on each configuration are given in Table II. In previous calculations [23,45] the correlation functions with different $t_{\rm src}$ on a given configuration were binned. Both calculations included states whose correlation functions exhibited significant correlation between the n_t source times, such as the η_h. However, correlation functions that are sufficiently far apart in time are expected to be only weakly correlated and it is preferable not to bin the multiple n_t in order to improve the resolution of the covariance matrix of our data points, particularly on sets 3 and 5 where $n_{\rm cfg}$ is relatively small. On set 1, we have computed the correlations between data generated from different values of $t_{\rm src}$. We find that excluding η_h and η_c, the maximum correlation between any two data points using different $t_{\rm src}$, using four equally spaced values of $t_{\rm src}$, is ≈0.2. On set 4, the maximum correlation between data from four different, equally spaced $t_{\rm src}$ is also ≈0.2. With these findings in mind, we choose to use the B_s and D_s^* masses, instead of those of the η_h and η_c as was done in [23,45], to parametrize the physical heavy and charm quark masses. We do not then bin our data on set 2, 3 or 5, and on sets 1 and 4 we only bin every four and two adjacent source times, respectively. We have investigated the effect this has on the uncertainty of the raw correlator data points, expecting that for fully uncorrelated data the standard deviation will not change. Histogram plots of $\sigma_{\rm unbinned}/\sigma_{\rm binned}$ are shown in Figs. 19 and 20, for all correlator data points entering the correlator fits used in this work, where we see that on each set binning results in very similar uncertainties consistent with the different time sources being uncorrelated. This allows us to use a smaller SVD cut when fitting our correlation functions and results in numerically more stable fits.

We have also checked the maximum and minimum values of this ratio obtained for any combination of m_h and $D_{(s)}^*$ momentum for the three-point functions as a function of t for each ensemble. We find that for the three-point functions the maximum reduction in standard deviation is ≈5%, with the majority of data points changing by less than ∼2%. For the two-point functions, the maximum reduction in standard deviation is ≈10%, with

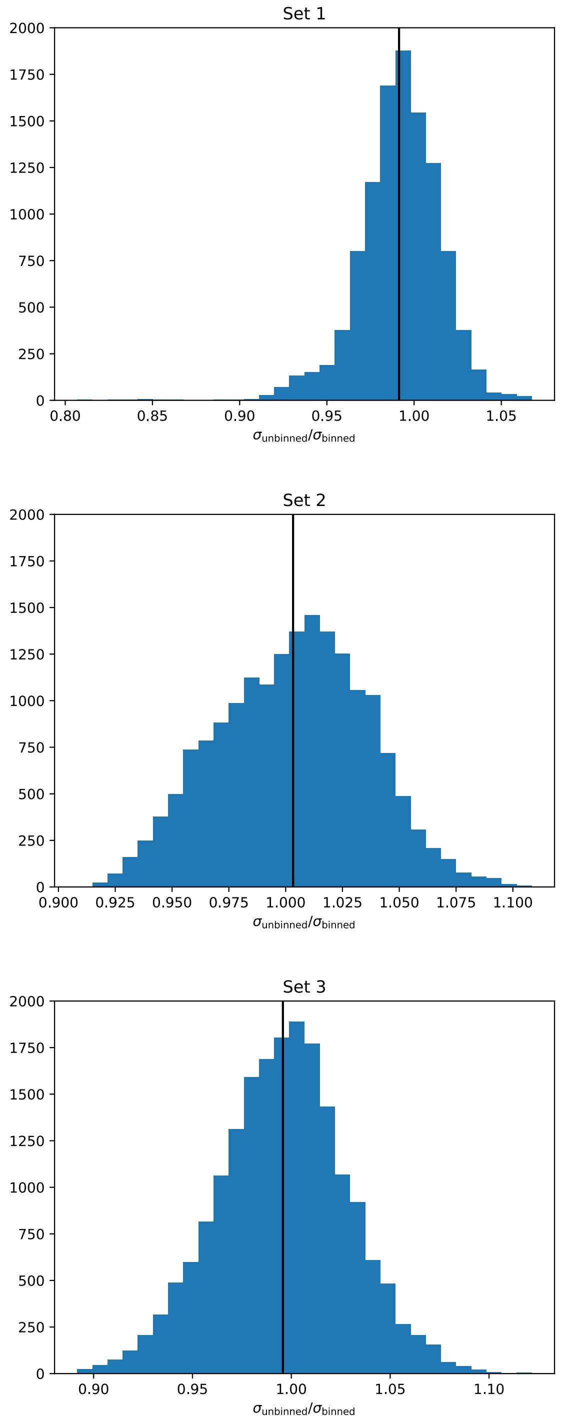

FIG. 19. Histogram plots showing the ratio of standard deviations, $\sigma_{\rm unbinned}/\sigma_{\rm binned}$, on each set for correlator data that has been only partially binned, or fully binned, as described in the text. The vertical black line corresponds to the mean. We only include data points in the range $t_{\rm min} \leq t \leq t_{\rm max}$.

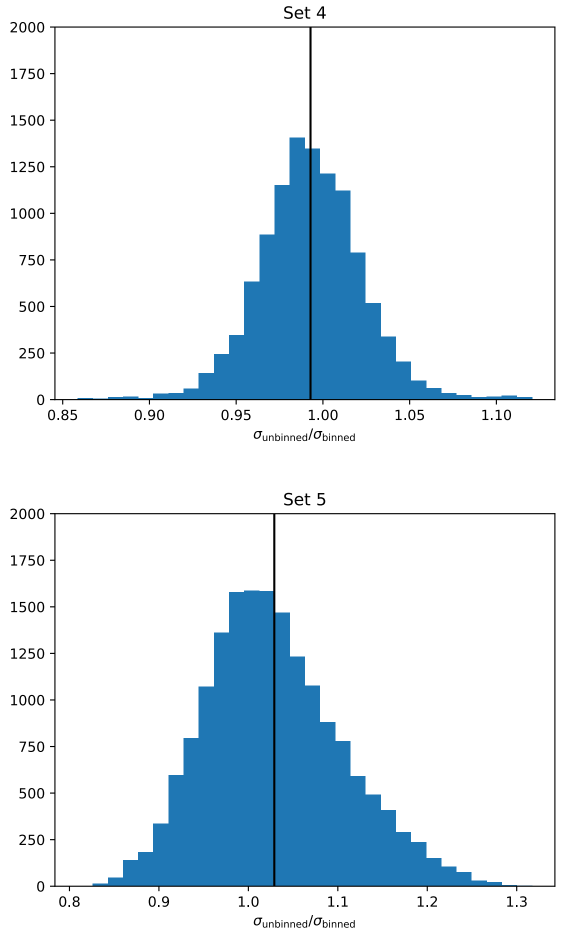

FIG. 20. Histogram plots showing the ratio of standard deviations, $\sigma_{\rm unbinned}/\sigma_{\rm binned}$, on each set for correlator data that has been only partially binned, or fully binned, as described in the text. The vertical black line corresponds to the mean. We only include data points in the range $t_{\rm min} \leq t \leq t_{\rm max}$.

the vast majority of points changing by less than ≈5%. We also see that these small changes are not strongly dependent on t. Since the statistical uncertainty of the three-point correlators is the dominant uncertainty entering the determination of the matrix elements, the observation that the three-point uncertainties remain essentially unchanged indicates that the partial binning procedure does not introduce any significant systematic under or overestimation of uncertainties in our final results.

APPENDIX C: LATTICE DATA

1. Lattice form factor results

Here we give our lattice results for the form factors extracted from correlator fits. The SM form factors for $B \to D^*$ are given in Tables XIX–XXIII and in Tables XXIX–XXXIII for $B_s \to D_s^*$. The tensor form factors for $B \to D^*$ are also given in Tables XXIV–XXVIII and in Tables XXXIV–XXXVIII for $B_s \to D_s^*$. These numbers include the renormalization factors given in Tables VII and VIII.

TABLE XIX. Lattice form factor results for set 1. ak here is the value of the x and y components of the lattice momentum for the D^*. ak is calculated from the corresponding twist in Table IV.

am_h	ak	h_{A_1}	h_{A_2}	h_{A_3}	h_V
0.65	0.0	0.933(15)	···	···	···
	0.0378853	0.932(14)	5(22)	−4(21)	1.19(38)
	0.0757705	0.926(15)	2.0(6.1)	−0.7(5.6)	1.24(28)
	0.113656	0.916(18)	1.2(3.4)	0.05(2.78)	1.24(23)
	0.151541	0.907(18)	0.8(2.3)	0.4(1.6)	1.24(20)
	0.189426	0.893(20)	0.7(2.0)	0.6(1.1)	1.22(19)
0.725	0.0	0.939(16)	···	···	···
	0.0378853	0.938(15)	5(22)	−3(22)	1.19(38)
	0.0757705	0.932(16)	1.7(6.2)	−0.6(5.8)	1.24(28)
	0.113656	0.922(18)	1.0(3.3)	0.08(2.89)	1.25(24)
	0.151541	0.913(18)	0.7(2.1)	0.4(1.7)	1.24(21)
	0.189426	0.898(21)	0.5(1.7)	0.6(1.2)	1.23(19)
0.8	0.0	0.946(16)	···	···	···
	0.0378853	0.945(15)	4(23)	−3(23)	1.20(39)
	0.0757705	0.939(16)	1.6(6.3)	−0.5(6.0)	1.25(28)
	0.113656	0.929(19)	0.9(3.3)	0.1(3.0)	1.26(24)
	0.151541	0.920(19)	0.6(2.1)	0.4(1.7)	1.25(21)
	0.189426	0.905(21)	0.4(1.6)	0.6(1.2)	1.24(20)

TABLE XX. Lattice form factor results for set 2. ak here is the value of the x and y components of the lattice momentum for the D^*. ak is calculated from the corresponding twist in Table IV.

am_h	ak	h_{A_1}	h_{A_2}	h_{A_3}	h_V
0.427	0.0	0.916(37)	···	···	···
	0.055399	0.916(42)	−9(15)	10(14)	1.11(31)
	0.110798	0.900(44)	−3.0(4.9)	3.7(3.8)	1.13(24)
	0.166197	0.872(53)	−1.9(3.7)	2.4(2.0)	1.10(22)
	0.221596	0.832(66)	−1.6(4.4)	1.9(1.4)	1.04(22)
	0.276995	0.780(84)	−2(10)	1.6(1.1)	0.98(25)
0.525	0.0	0.921(40)	···	···	···
	0.055399	0.921(44)	−10(16)	11(15)	1.11(32)
	0.110798	0.904(47)	−3.2(4.7)	3.9(4.0)	1.13(24)
	0.166197	0.876(57)	−1.9(3.0)	2.5(2.1)	1.10(22)
	0.221596	0.836(71)	−1.4(2.7)	1.9(1.5)	1.05(23)
	0.276995	0.785(90)	−1.2(3.1)	1.6(1.2)	0.99(26)
0.65	0.0	0.930(43)	···	···	···
	0.055399	0.930(48)	−11(17)	12(16)	1.12(32)
	0.110798	0.913(51)	−3.4(4.8)	4.1(4.3)	1.14(25)
	0.166197	0.884(61)	−1.9(2.9)	2.6(2.3)	1.11(23)
	0.221596	0.845(77)	−1.4(2.4)	2.0(1.6)	1.06(24)
	0.276995	0.794(97)	−1.2(2.4)	1.7(1.3)	1.00(27)
0.8	0.0	0.943(46)	···	···	···
	0.055399	0.943(51)	−11(18)	12(17)	1.13(33)
	0.110798	0.927(55)	−3.5(5.0)	4.2(4.7)	1.15(26)
	0.166197	0.898(67)	−2.0(3.0)	2.7(2.5)	1.13(24)
	0.221596	0.859(83)	−1.5(2.4)	2.1(1.8)	1.08(24)
	0.276995	0.81(10)	−1.2(2.2)	1.7(1.5)	1.02(28)

TABLE XXI. Lattice form factor results for set 3. ak here is the value of the x and y components of the lattice momentum for the D^*. ak is calculated from the corresponding twist in Table IV.

am_h	ak	h_{A_1}	h_{A_2}	h_{A_3}	h_V
0.5	0.0	0.916(22)	···	···	···
	0.061831	0.902(25)	0.05(3.91)	0.9(3.7)	1.21(14)
	0.123662	0.850(39)	−0.2(1.7)	1.1(1.4)	1.11(12)
	0.185493	0.774(58)	0.3(1.4)	0.89(93)	0.97(14)
	0.247324	0.689(91)	1.1(1.7)	0.67(85)	0.84(18)
	0.309155	0.60(10)	0.3(1.9)	0.70(68)	0.77(15)
0.65	0.0	0.932(24)	···	···	···
	0.061831	0.917(28)	−0.3(4.2)	1.2(4.1)	1.26(14)
	0.123662	0.863(43)	−0.4(1.8)	1.3(1.6)	1.15(12)
	0.185493	0.789(63)	−0.002(1.375)	1.0(1.0)	1.00(14)
	0.247324	0.711(98)	0.4(1.5)	0.85(93)	0.86(19)
	0.309155	0.62(11)	−0.3(1.4)	0.88(73)	0.77(16)
0.8	0.0	0.950(26)	···	···	···
	0.061831	0.934(31)	−0.3(4.6)	1.2(4.5)	1.30(15)
	0.123662	0.880(47)	−0.5(2.0)	1.4(1.8)	1.19(13)
	0.185493	0.809(70)	−0.2(1.5)	1.2(1.2)	1.03(15)
	0.247324	0.74(11)	0.02(1.52)	1.0(1.0)	0.87(20)
	0.309155	0.64(12)	−0.6(1.3)	1.04(80)	0.77(18)

TABLE XXII. Lattice form factor results for set 4. ak here is the value of the x and y components of the lattice momentum for the D^*. ak is calculated from the corresponding twist in Table IV.

am_h	ak	h_{A_1}	h_{A_2}	h_{A_3}	h_V
0.65	0.0	0.935(29)	···	···	···
	0.0376581	0.937(27)	−5(40)	7(40)	1.20(50)
	0.0753162	0.934(27)	−2(11)	3(10)	1.23(35)
	0.112974	0.927(28)	−0.9(5.6)	2.1(4.7)	1.23(29)
	0.150632	0.919(31)	−0.7(4.0)	1.8(2.9)	1.21(26)
	0.188291	0.907(34)	−0.7(3.3)	1.7(2.1)	1.19(24)
0.725	0.0	0.941(30)	···	···	···
	0.0376581	0.943(28)	−5(42)	7(42)	1.21(51)
	0.0753162	0.939(28)	−2(11)	3(11)	1.24(35)
	0.112974	0.933(30)	−1.1(5.6)	2.2(5.0)	1.24(29)
	0.150632	0.924(32)	−0.9(3.7)	1.9(3.0)	1.23(26)
	0.188291	0.913(35)	−0.8(3.0)	1.8(2.2)	1.21(25)
0.8	0.0	0.948(31)	···	···	···
	0.0376581	0.950(29)	−6(44)	7(43)	1.23(52)
	0.0753162	0.947(30)	−2(12)	3(11)	1.25(36)
	0.112974	0.940(31)	−1.2(5.7)	2.2(5.2)	1.25(30)
	0.150632	0.931(33)	−1.0(3.7)	1.9(3.2)	1.24(27)
	0.188291	0.920(37)	−0.9(2.9)	1.8(2.3)	1.22(25)

2. Error band plots

Here we show plots for the fractional contribution of each source of uncertainty to the total variance for the $B \to D^*$ form factors F_1 and F_2, as well as the tensor form

TABLE XXIII. Lattice form factor results for set 5. ak here is the value of the x and y components of the lattice momentum for the D^*. ak is calculated from the corresponding twist in Table IV.

am_h	ak	h_{A_1}	h_{A_2}	h_{A_3}	h_V
0.427	0.0	0.886(77)	· · ·	· · ·	· · ·
	0.055399	0.882(73)	7(24)	−4(23)	0.88(51)
	0.110798	0.854(79)	2.7(7.7)	−0.5(6.1)	1.03(38)
	0.166197	0.804(95)	2.1(5.5)	0.2(3.2)	1.02(35)
	0.221596	0.74(12)	2.2(6.0)	0.4(2.2)	0.95(37)
	0.276995	0.67(14)	4(10)	0.4(1.7)	0.83(38)
0.525	0.0	0.888(81)	· · ·	· · ·	· · ·
	0.055399	0.884(77)	6(25)	−4(24)	0.88(51)
	0.110798	0.857(83)	2.1(7.3)	−0.5(6.4)	1.02(38)
	0.166197	0.807(99)	1.4(4.7)	0.2(3.4)	1.02(36)
	0.221596	0.74(12)	1.2(4.1)	0.4(2.3)	0.95(37)
	0.276995	0.67(14)	1.4(4.2)	0.3(1.8)	0.83(39)
0.65	0.0	0.892(86)	· · ·	· · ·	· · ·
	0.055399	0.889(81)	6(26)	−5(25)	0.88(52)
	0.110798	0.862(87)	1.9(7.4)	−0.5(6.7)	1.03(38)
	0.166197	0.81(10)	1.1(4.4)	0.2(3.6)	1.02(36)
	0.221596	0.75(13)	0.9(3.6)	0.4(2.5)	0.95(38)
	0.276995	0.67(15)	1.0(3.3)	0.3(1.9)	0.83(40)
0.8	0.0	0.899(90)	· · ·	· · ·	· · ·
	0.055399	0.897(85)	6(27)	−5(26)	0.88(52)
	0.110798	0.870(91)	1.8(7.6)	−0.6(7.0)	1.03(39)
	0.166197	0.82(11)	1.0(4.4)	0.2(3.7)	1.03(37)
	0.221596	0.75(13)	0.8(3.4)	0.3(2.6)	0.96(39)
	0.276995	0.67(15)	0.9(3.0)	0.3(2.0)	0.84(41)

TABLE XXIV. Lattice tensor form factor results for set 1. ak here is the value of the x and y components of the lattice momentum for the D^*. ak is calculated from the corresponding twist in Table IV.

am_h	ak	h_{T_1}	h_{T_2}	h_{T_3}
0.65	0.0	· · ·	· · ·	· · ·
	0.0378853	0.873(24)	−0.07(27)	0.06(38.61)
	0.0757705	0.867(25)	−0.08(20)	−1(10)
	0.113656	0.858(28)	−0.08(17)	−0.9(5.1)
	0.151541	0.845(28)	−0.07(15)	−0.8(2.8)
	0.189426	0.831(31)	−0.06(14)	−0.7(2.0)
0.725	0.0	· · ·	· · ·	· · ·
	0.0378853	0.878(24)	−0.08(28)	−0.2(38.9)
	0.0757705	0.873(26)	−0.09(20)	−1(10)
	0.113656	0.863(29)	−0.09(17)	−1.0(5.1)
	0.151541	0.850(28)	−0.08(15)	−0.9(2.8)
	0.189426	0.836(31)	−0.07(14)	−0.7(2.0)
0.8	0.0	· · ·	· · ·	· · ·
	0.0378853	0.885(24)	−0.08(28)	−0.5(39.2)
	0.0757705	0.880(26)	−0.10(21)	−1(10)
	0.113656	0.870(29)	−0.10(18)	−1.0(5.1)
	0.151541	0.857(29)	−0.09(16)	−0.9(2.8)
	0.189426	0.843(32)	−0.08(15)	−0.7(2.0)

TABLE XXV. Lattice tensor form factor results for set 2. ak here is the value of the x and y components of the lattice momentum for the D^*. ak is calculated from the corresponding twist in Table IV.

am_h	ak	h_{T_1}	h_{T_2}	h_{T_3}
0.427	0.0	· · ·	· · ·	· · ·
	0.055399	0.878(59)	−0.05(26)	6(20)
	0.110798	0.860(63)	−0.07(20)	1.7(5.3)
	0.166197	0.831(76)	−0.07(19)	0.9(2.8)
	0.221596	0.791(94)	−0.06(20)	0.7(1.9)
	0.276995	0.74(12)	−0.07(22)	0.6(1.5)
0.525	0.0	· · ·	· · ·	· · ·
	0.055399	0.887(59)	−0.06(27)	7(20)
	0.110798	0.869(64)	−0.08(21)	2.1(5.3)
	0.166197	0.840(76)	−0.08(20)	1.1(2.8)
	0.221596	0.799(95)	−0.07(21)	0.8(1.9)
	0.276995	0.75(12)	−0.08(23)	0.7(1.6)
0.65	0.0	· · ·	· · ·	· · ·
	0.055399	0.899(61)	−0.08(29)	8(21)
	0.110798	0.881(65)	−0.10(22)	2.4(5.4)
	0.166197	0.851(78)	−0.10(21)	1.3(2.9)
	0.221596	0.810(98)	−0.09(23)	0.9(2.0)
	0.276995	0.76(12)	−0.08(24)	0.8(1.6)
0.8	0.0	· · ·	· · ·	· · ·
	0.055399	0.915(63)	−0.10(30)	9(21)
	0.110798	0.898(68)	−0.12(23)	2.7(5.6)
	0.166197	0.867(81)	−0.11(23)	1.4(3.0)
	0.221596	0.83(10)	−0.10(24)	1.0(2.1)
	0.276995	0.77(13)	−0.09(26)	0.8(1.7)

TABLE XXVI. Lattice tensor form factor results for set 3. ak here is the value of the x and y components of the lattice momentum for the D^*. ak is calculated from the corresponding twist in Table IV.

am_h	ak	h_{T_1}	h_{T_2}	h_{T_3}
0.5	0.0	· · ·	· · ·	· · ·
	0.061831	0.877(32)	−0.04(14)	−1.8(4.6)
	0.123662	0.820(50)	−0.03(13)	−0.6(1.8)
	0.185493	0.748(73)	0.001(168)	−0.4(1.1)
	0.247324	0.66(12)	0.02(24)	−0.5(1.1)
	0.309155	0.65(16)	0.45(48)	0.23(86)
0.65	0.0	· · ·	· · ·	· · ·
	0.061831	0.898(33)	−0.04(15)	−1.2(4.7)
	0.123662	0.843(52)	−0.04(14)	−0.2(1.8)
	0.185493	0.772(76)	0.007(177)	−0.1(1.2)
	0.247324	0.69(13)	0.05(25)	−0.2(1.1)
	0.309155	0.68(16)	0.47(51)	0.41(89)
0.8	0.0	· · ·	· · ·	· · ·
	0.061831	0.920(35)	−0.05(16)	−0.9(5.1)
	0.123662	0.866(56)	−0.04(15)	0.0004(1.9847)
	0.185493	0.798(82)	0.01(19)	0.08(1.25)
	0.247324	0.73(13)	0.07(27)	0.06(1.14)
	0.309155	0.71(17)	0.50(54)	0.61(94)

TABLE XXVII. Lattice tensor form factor results for set 4. ak here is the value of the x and y components of the lattice momentum for the D^*. ak is calculated from the corresponding twist in Table IV.

am_h	ak	h_{T_1}	h_{T_2}	h_{T_3}
0.65	0.0	…	…	…
	0.0376581	0.875(44)	−0.19(40)	4(67)
	0.0753162	0.872(44)	−0.18(29)	1(17)
	0.1129 74	0.867(47)	−0.17(24)	0.8(7.9)
	0.150632	0.859(51)	−0.16(22)	0.5(4.8)
	0.188291	0.849(56)	−0.15(21)	0.4(3.4)
0.725	0.0	…	…	…
	0.0376581	0.881(44)	−0.19(41)	3(68)
	0.0753162	0.878(45)	−0.18(30)	1(17)
	0.112974	0.873(48)	−0.17(25)	0.6(8.1)
	0.150632	0.865(52)	−0.16(23)	0.5(4.9)
	0.188291	0.855(57)	−0.15(22)	0.4(3.4)
0.8	0.0	…	…	…
	0.0376581	0.888(45)	−0.19(42)	2(70)
	0.0753162	0.885(46)	−0.18(30)	0.8(17.7)
	0.112974	0.880(49)	−0.17(26)	0.5(8.2)
	0.150632	0.872(53)	−0.17(23)	0.4(5.0)
	0.188291	0.861(58)	−0.16(22)	0.4(3.5)

TABLE XXVIII. Lattice tensor form factor results for set 5. ak here is the value of the x and y components of the lattice momentum for the D^*. ak is calculated from the corresponding twist in Table IV.

am_h	ak	h_{T_1}	h_{T_2}	h_{T_3}
0.427	0.0	…	…	…
	0.055399	0.840(92)	−0.07(42)	−3(28)
	0.110798	0.81(10)	−0.12(33)	−0.8(7.6)
	0.166197	0.75(12)	−0.15(32)	−0.3(4.1)
	0.221596	0.69(16)	−0.18(35)	−0.2(2.9)
	0.276995	0.61(19)	−0.22(39)	−0.3(2.2)
0.525	0.0	…	…	…
	0.055399	0.845(91)	−0.06(43)	−3(28)
	0.110798	0.81(10)	−0.12(34)	−0.8(7.6)
	0.166197	0.76(12)	−0.15(34)	−0.3(4.1)
	0.221596	0.69(16)	−0.18(37)	−0.2(2.9)
	0.276995	0.61(19)	−0.22(41)	−0.3(2.2)
0.65	0.0	…	…	…
	0.055399	0.851(92)	−0.03(45)	−4(28)
	0.110798	0.82(10)	−0.11(35)	−0.9(7.6)
	0.166197	0.76(12)	−0.15(35)	−0.4(4.1)
	0.221596	0.69(16)	−0.18(39)	−0.2(2.9)
	0.276995	0.61(19)	−0.22(43)	−0.3(2.2)
0.8	0.0	…	…	…
	0.055399	0.861(92)	−0.01(47)	−4(28)
	0.110798	0.83(10)	−0.10(37)	−1.0(7.6)
	0.166197	0.77(12)	−0.15(37)	−0.4(4.1)
	0.221596	0.70(16)	−0.18(41)	−0.2(2.9)
	0.276995	0.62(20)	−0.22(46)	−0.3(2.3)

TABLE XXIX. Lattice form factor results for set 1. ak here is the value of the x and y components of the lattice momentum for the D_s^*. ak is calculated from the corresponding twist in Table IV.

am_h	ak	$h^s_{A_1}$	$h^s_{A_2}$	$h^s_{A_3}$	h^s_V
0.65	0.0	0.9293(50)	…	…	…
	0.0378853	0.9281(48)	0.5(7.1)	0.8(6.9)	1.27(16)
	0.0757705	0.9231(53)	0.3(2.1)	0.9(1.9)	1.27(11)
	0.113656	0.9152(58)	0.2(1.1)	0.99(93)	1.258(87)
	0.151541	0.9040(64)	0.25(82)	1.02(58)	1.241(74)
	0.189426	0.8900(72)	0.30(69)	1.02(41)	1.219(67)
0.725	0.0	0.9342(51)	…	…	…
	0.0378853	0.9330(50)	0.3(7.2)	0.8(7.1)	1.27(17)
	0.0757705	0.9280(55)	0.2(2.1)	0.9(2.0)	1.27(11)
	0.113656	0.9200(59)	0.1(1.1)	0.97(96)	1.264(89)
	0.151541	0.9088(66)	0.08(74)	1.00(60)	1.248(76)
	0.189426	0.8947(74)	0.08(59)	1.01(42)	1.226(69)
0.8	0.0	0.9404(52)	…	…	…
	0.0378853	0.9392(51)	0.2(7.4)	0.9(7.3)	1.28(17)
	0.0757705	0.9341(56)	0.1(2.1)	0.9(2.0)	1.28(11)
	0.113656	0.9261(61)	0.02(1.09)	0.97(99)	1.274(91)
	0.151541	0.9148(68)	−0.005(722)	1.00(61)	1.257(78)
	0.189426	0.9006(76)	−0.01(56)	1.01(44)	1.235(70)

TABLE XXX. Lattice form factor results for set 2. ak here is the value of the x and y components of the lattice momentum for the D_s^*. ak is calculated from the corresponding twist in Table IV.

am_h	ak	$h^s_{A_1}$	$h^s_{A_2}$	$h^s_{A_3}$	h^s_V
0.427	0.0	0.908(15)	…	…	…
	0.055399	0.902(16)	−3.3(6.0)	4.2(5.6)	1.23(16)
	0.110798	0.879(17)	−1.1(2.0)	2.0(1.5)	1.21(12)
	0.166197	0.844(21)	−0.7(1.5)	1.50(81)	1.15(11)
	0.221596	0.801(26)	−0.6(1.9)	1.30(57)	1.08(12)
	0.276995	0.753(34)	−0.2(4.2)	1.15(48)	1.00(13)
0.525	0.0	0.913(15)	…	…	…
	0.055399	0.907(17)	−3.5(6.1)	4.3(5.8)	1.23(16)
	0.110798	0.884(18)	−1.2(1.9)	2.0(1.6)	1.21(12)
	0.166197	0.849(22)	−0.8(1.2)	1.50(86)	1.15(11)
	0.221596	0.804(27)	−0.6(1.1)	1.29(61)	1.08(12)
	0.276995	0.756(36)	−0.5(1.3)	1.15(51)	1.00(13)
0.65	0.0	0.922(16)	…	…	…
	0.055399	0.916(18)	−3.6(6.3)	4.3(6.1)	1.24(16)
	0.110798	0.893(19)	−1.2(1.9)	2.0(1.7)	1.21(12)
	0.166197	0.856(23)	−0.8(1.1)	1.50(91)	1.16(11)
	0.221596	0.812(29)	−0.65(96)	1.30(65)	1.09(12)
	0.276995	0.764(38)	−0.53(99)	1.17(55)	1.01(13)
0.8	0.0	0.936(17)	…	…	…
	0.055399	0.930(19)	−3.6(6.6)	4.3(6.5)	1.26(16)
	0.110798	0.906(21)	−1.3(2.0)	2.0(1.8)	1.23(13)
	0.166197	0.869(25)	−0.9(1.2)	1.51(97)	1.18(12)
	0.221596	0.824(31)	−0.69(93)	1.32(70)	1.11(12)
	0.276995	0.776(41)	−0.57(92)	1.19(60)	1.02(14)

TABLE XXXI. Lattice form factor results for set 3. ak here is the value of the x and y components of the lattice momentum for the D_s^*. ak is calculated from the corresponding twist in Table IV.

am_h	ak	$h^s_{A_1}$	$h^s_{A_2}$	$h^s_{A_3}$	h^s_V
0.5	0.0	0.9169(92)	⋯	⋯	⋯
	0.061831	0.8984(90)	−0.4(1.4)	1.2(1.3)	1.247(58)
	0.123662	0.845(12)	−0.45(53)	1.18(44)	1.142(38)
	0.185493	0.772(17)	−0.48(42)	1.15(28)	1.021(41)
	0.247324	0.688(30)	−0.33(58)	1.02(28)	0.901(92)
	0.309155	0.597(54)	−0.25(97)	0.87(33)	0.86(12)
0.65	0.0	0.931(10)	⋯	⋯	⋯
	0.061831	0.9117(99)	−0.4(1.5)	1.2(1.4)	1.272(64)
	0.123662	0.857(13)	−0.48(56)	1.19(49)	1.162(43)
	0.185493	0.785(19)	−0.54(42)	1.18(31)	1.035(46)
	0.247324	0.705(33)	−0.46(52)	1.08(32)	0.902(99)
	0.309155	0.620(58)	−0.50(76)	0.98(38)	0.84(13)
0.8	0.0	0.948(11)	⋯	⋯	⋯
	0.061831	0.928(11)	−0.4(1.6)	1.2(1.6)	1.300(69)
	0.123662	0.872(14)	−0.52(60)	1.21(54)	1.186(48)
	0.185493	0.801(20)	−0.60(44)	1.23(35)	1.054(51)
	0.247324	0.726(36)	−0.58(52)	1.17(36)	0.91(11)
	0.309155	0.651(64)	−0.70(74)	1.12(43)	0.82(14)

factors in the helicity basis defined in Eq. (32) (plots for g and f for $B \to D^*$ are given in Fig. 8 in the main text). Plots for the full set of $B_s \to D_s^*$ form factors are given in Figs. 23–25.

TABLE XXXII. Lattice form factor results for set 4. ak here is the value of the x and y components of the lattice momentum for the D_s^*. ak is calculated from the corresponding twist in Table IV.

am_h	ak	$h^s_{A_1}$	$h^s_{A_2}$	$h^s_{A_3}$	h^s_V
0.65	0.0	0.9271(42)	⋯	⋯	⋯
	0.0376581	0.9269(41)	−1.8(5.7)	2.9(5.6)	1.31(14)
	0.0753162	0.9222(46)	−0.7(1.8)	1.8(1.6)	1.284(95)
	0.112974	0.9148(51)	−0.39(96)	1.51(80)	1.262(77)
	0.150632	0.9043(56)	−0.23(68)	1.38(50)	1.237(68)
	0.188291	0.8911(62)	−0.12(57)	1.31(35)	1.207(64)
0.725	0.0	0.9323(43)	⋯	⋯	⋯
	0.0376581	0.9321(42)	−1.9(5.9)	2.9(5.8)	1.31(14)
	0.0753162	0.9274(48)	−0.8(1.8)	1.9(1.7)	1.290(97)
	0.112974	0.9199(52)	−0.51(94)	1.51(83)	1.268(79)
	0.150632	0.9093(58)	−0.36(64)	1.38(52)	1.242(70)
	0.188291	0.8960(64)	−0.28(50)	1.31(37)	1.212(65)
0.8	0.0	0.9387(44)	⋯	⋯	⋯
	0.0376581	0.9384(43)	−2.0(6.0)	3.0(6.0)	1.32(15)
	0.0753162	0.9337(49)	−0.9(1.8)	1.9(1.7)	1.30(10)
	0.112974	0.9261(54)	−0.58(94)	1.52(86)	1.276(81)
	0.150632	0.9155(60)	−0.44(63)	1.39(54)	1.250(72)
	0.188291	0.9021(66)	−0.36(49)	1.31(38)	1.220(67)

TABLE XXXIII. Lattice form factor results for set 5. ak here is the value of the x and y components of the lattice momentum for the D_s^*. ak is calculated from the corresponding twist in Table IV.

am_h	ak	$h^s_{A_1}$	$h^s_{A_2}$	$h^s_{A_3}$	h^s_V
0.427	0.0	0.898(22)	⋯	⋯	⋯
	0.055399	0.894(21)	1.4(6.3)	−0.3(6.0)	1.24(15)
	0.110798	0.874(21)	0.1(1.9)	0.9(1.5)	1.22(11)
	0.166197	0.838(24)	0.002(1.409)	1.01(80)	1.16(11)
	0.221596	0.790(31)	0.05(1.65)	0.97(61)	1.09(11)
	0.276995	0.734(42)	0.2(3.0)	0.90(53)	1.01(13)
0.525	0.0	0.903(23)	⋯	⋯	⋯
	0.055399	0.900(22)	1.5(6.5)	−0.5(6.3)	1.24(15)
	0.110798	0.880(22)	0.06(1.86)	0.8(1.6)	1.22(11)
	0.166197	0.843(25)	−0.1(1.2)	0.97(86)	1.17(11)
	0.221596	0.794(33)	−0.1(1.1)	0.94(65)	1.10(12)
	0.276995	0.737(44)	−0.06(1.37)	0.87(58)	1.02(13)
0.65	0.0	0.912(24)	⋯	⋯	⋯
	0.055399	0.909(23)	1.8(6.9)	−0.9(6.7)	1.25(16)
	0.110798	0.889(23)	0.08(1.92)	0.8(1.7)	1.23(12)
	0.166197	0.851(27)	−0.1(1.2)	0.93(94)	1.18(11)
	0.221596	0.801(35)	−0.1(1.0)	0.91(71)	1.11(12)
	0.276995	0.743(48)	−0.1(1.1)	0.84(63)	1.03(14)
0.8	0.0	0.926(26)	⋯	⋯	⋯
	0.055399	0.922(25)	2.1(7.4)	−1.3(7.3)	1.27(16)
	0.110798	0.901(25)	0.1(2.0)	0.7(1.9)	1.25(12)
	0.166197	0.862(29)	−0.1(1.2)	0.9(1.0)	1.19(12)
	0.221596	0.811(38)	−0.1(1.0)	0.88(78)	1.12(13)
	0.276995	0.752(52)	−0.1(1.0)	0.81(69)	1.04(14)

TABLE XXXIV. Lattice tensor form factor results for set 1. ak here is the value of the x and y components of the lattice momentum for the D_s^*. ak is calculated from the corresponding twist in Table IV.

am_h	ak	$h^s_{T_1}$	$h^s_{T_2}$	$h^s_{T_3}$
0.65	0.0	⋯	⋯	⋯
	0.0378853	0.8654(76)	−0.08(13)	0.06(10.90)
	0.0757705	0.8597(75)	−0.083(82)	−0.4(2.7)
	0.113656	0.8506(79)	−0.079(64)	−0.3(1.3)
	0.151541	0.8383(84)	−0.075(56)	−0.29(76)
	0.189426	0.8231(93)	−0.070(53)	−0.25(53)
0.725	0.0	⋯	⋯	⋯
	0.0378853	0.8712(77)	−0.09(13)	0.08(10.96)
	0.0757705	0.8654(76)	−0.095(84)	−0.4(2.7)
	0.113656	0.8563(80)	−0.091(65)	−0.4(1.3)
	0.151541	0.8440(85)	−0.086(57)	−0.30(77)
	0.189426	0.8286(94)	−0.081(54)	−0.26(54)
0.8	0.0	⋯	⋯	⋯
	0.0378853	0.8778(78)	−0.10(14)	0.1(11.1)
	0.0757705	0.8720(77)	−0.106(86)	−0.4(2.7)
	0.113656	0.8629(81)	−0.101(67)	−0.4(1.3)
	0.151541	0.8504(87)	−0.097(58)	−0.32(78)
	0.189426	0.8349(95)	−0.091(55)	−0.27(55)

TABLE XXXV. Lattice tensor form factor results for set 2. ak here is the value of the x and y components of the lattice momentum for the D_s^*. ak is calculated from the corresponding twist in Table IV.

am_h	ak	$h^s_{T_1}$	$h^s_{T_2}$	$h^s_{T_3}$
0.427	0.0	⋯	⋯	⋯
	0.055399	0.870(22)	−0.09(14)	2.3(7.7)
	0.110798	0.845(25)	−0.09(11)	0.5(2.2)
	0.166197	0.807(30)	−0.07(11)	0.2(1.2)
	0.221596	0.763(37)	−0.05(12)	0.20(80)
	0.276995	0.714(48)	−0.05(14)	0.19(65)
0.525	0.0	⋯	⋯	⋯
	0.055399	0.878(22)	−0.11(14)	2.5(7.7)
	0.110798	0.852(25)	−0.11(12)	0.5(2.2)
	0.166197	0.814(30)	−0.09(12)	0.3(1.2)
	0.221596	0.769(38)	−0.07(13)	0.21(82)
	0.276995	0.720(49)	−0.06(14)	0.20(67)
0.65	0.0	⋯	⋯	⋯
	0.055399	0.889(22)	−0.13(15)	2.5(7.7)
	0.110798	0.863(25)	−0.13(12)	0.6(2.2)
	0.166197	0.824(31)	−0.11(12)	0.3(1.2)
	0.221596	0.778(39)	−0.09(14)	0.22(84)
	0.276995	0.729(51)	−0.08(15)	0.21(69)
0.8	0.0	⋯	⋯	⋯
	0.055399	0.904(23)	−0.16(16)	2.6(7.9)
	0.110798	0.877(26)	−0.15(13)	0.6(2.3)
	0.166197	0.838(32)	−0.13(13)	0.3(1.2)
	0.221596	0.791(41)	−0.11(14)	0.23(88)
	0.276995	0.742(54)	−0.10(16)	0.22(73)

TABLE XXXVI. Lattice tensor form factor results for set 3. ak here is the value of the x and y components of the lattice momentum for the D_s^*. ak is calculated from the corresponding twist in Table IV.

am_h	ak	$h^s_{T_1}$	$h^s_{T_2}$	$h^s_{T_3}$
0.5	0.0	⋯	⋯	⋯
	0.061831	0.883(12)	−0.135(70)	−0.04(1.74)
	0.123662	0.823(16)	−0.120(56)	−0.10(59)
	0.185493	0.747(23)	−0.072(79)	0.02(36)
	0.247324	0.670(41)	0.04(15)	0.11(36)
	0.309155	0.628(92)	0.42(39)	0.36(51)
0.65	0.0	⋯	⋯	⋯
	0.061831	0.902(13)	−0.159(75)	−0.04(1.90)
	0.123662	0.841(17)	−0.140(60)	−0.06(65)
	0.185493	0.764(25)	−0.091(84)	0.06(41)
	0.247324	0.688(45)	0.02(16)	0.16(40)
	0.309155	0.645(97)	0.39(40)	0.42(55)
0.8	0.0	⋯	⋯	⋯
	0.061831	0.921(14)	−0.176(81)	−0.03(2.05)
	0.123662	0.859(19)	−0.154(65)	−0.009(705)
	0.185493	0.782(27)	−0.102(89)	0.11(45)
	0.247324	0.710(49)	0.008(167)	0.24(45)
	0.309155	0.67(10)	0.38(42)	0.53(59)

TABLE XXXVII. Lattice tensor form factor results for set 4. ak here is the value of the x and y components of the lattice momentum for the D_s^*. ak is calculated from the corresponding twist in Table IV.

am_h	ak	$h^s_{T_1}$	$h^s_{T_2}$	$h^s_{T_3}$
0.65	0.0	⋯	⋯	⋯
	0.0376581	0.8644(69)	−0.10(12)	2.9(9.2)
	0.0753162	0.8586(68)	−0.102(72)	0.7(2.2)
	0.112974	0.8498(70)	−0.099(55)	0.3(1.1)
	0.150632	0.8377(74)	−0.096(48)	0.10(63)
	0.188291	0.8226(79)	−0.093(45)	0.02(44)
0.725	0.0	⋯	⋯	⋯
	0.0376581	0.8703(70)	−0.11(12)	2.9(9.3)
	0.0753162	0.8644(69)	−0.112(73)	0.8(2.3)
	0.112974	0.8556(71)	−0.109(57)	0.3(1.1)
	0.150632	0.8434(75)	−0.107(50)	0.10(64)
	0.188291	0.8282(80)	−0.104(46)	0.03(44)
0.8	0.0	⋯	⋯	⋯
	0.0376581	0.8770(71)	−0.12(12)	2.9(9.5)
	0.0753162	0.8711(70)	−0.122(75)	0.8(2.3)
	0.112974	0.8622(73)	−0.119(58)	0.3(1.1)
	0.150632	0.8499(76)	−0.116(51)	0.11(65)
	0.188291	0.8346(82)	−0.113(48)	0.03(45)

TABLE XXXVIII. Lattice tensor form factor results for set 5. ak here is the value of the x and y components of the lattice momentum for the D_s^*. ak is calculated from the corresponding twist in Table IV.

am_h	ak	$h^s_{T_1}$	$h^s_{T_2}$	$h^s_{T_3}$
0.427	0.0	⋯	⋯	⋯
	0.055399	0.858(24)	−0.08(16)	−1.7(7.6)
	0.110798	0.835(25)	−0.09(13)	−0.3(2.0)
	0.166197	0.794(30)	−0.09(12)	−0.2(1.0)
	0.221596	0.743(39)	−0.08(13)	−0.13(76)
	0.276995	0.686(53)	−0.08(15)	−0.10(64)
0.525	0.0	⋯	⋯	⋯
	0.055399	0.866(25)	−0.09(17)	−1.9(7.7)
	0.110798	0.843(26)	−0.10(13)	−0.3(2.1)
	0.166197	0.802(31)	−0.10(12)	−0.2(1.1)
	0.221596	0.751(40)	−0.09(13)	−0.12(79)
	0.276995	0.693(55)	−0.09(15)	−0.10(67)
0.65	0.0	⋯	⋯	⋯
	0.055399	0.878(26)	−0.11(17)	−2.1(8.0)
	0.110798	0.854(27)	−0.12(14)	−0.4(2.1)
	0.166197	0.813(32)	−0.12(13)	−0.2(1.1)
	0.221596	0.761(42)	−0.11(14)	−0.12(83)
	0.276995	0.702(57)	−0.10(16)	−0.09(70)
0.8	0.0	⋯	⋯	⋯
	0.055399	0.893(27)	−0.14(18)	−2.4(8.3)
	0.110798	0.869(28)	−0.14(15)	−0.4(2.2)
	0.166197	0.827(34)	−0.13(14)	−0.2(1.2)
	0.221596	0.774(45)	−0.12(15)	−0.11(89)
	0.276995	0.714(61)	−0.11(17)	−0.09(76)

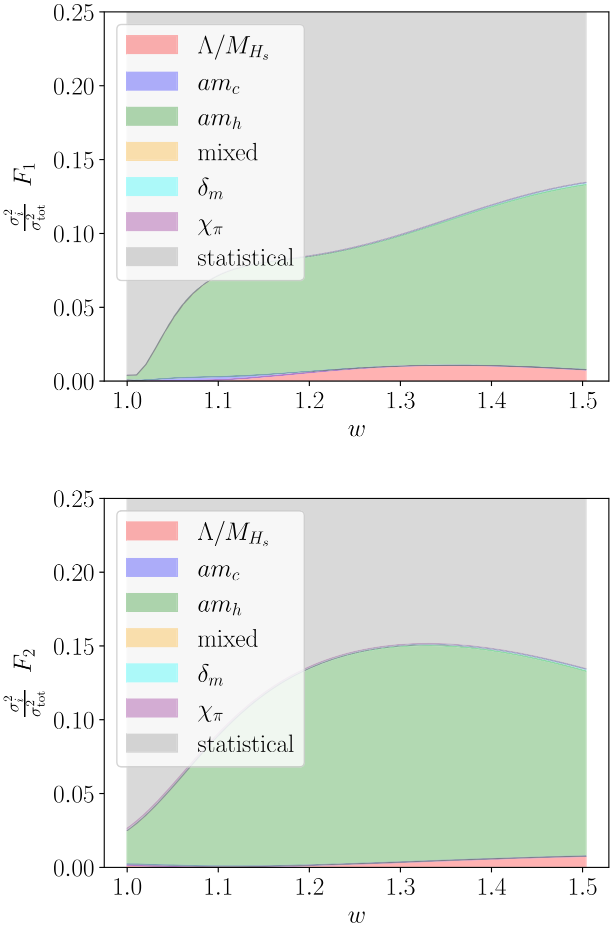

FIG. 21. Plots showing the fractional contribution of each source of uncertainty to the total variance for the $B \to D^*$ form factors F_1 and F_2 across the full kinematic range. The vertical axis is truncated at 0.25 for clarity, with the remaining variance between 0.25 and 1 attributable to statistics.

APPENDIX D: STAGGERED CHIRAL PERTURBATION THEORY

To compute the chiral logarithms for the $B \to D^{(*)}$ tensor form factors we use heavy-meson chiral perturbation theory, modified to account for the multiple tastes present when using staggered quarks [72]. The heavy meson fields are given by

$$H_a = \frac{1+\slashed{v}}{2}[\gamma^\mu B^*_{a\mu} + i\gamma^5 B_a]$$

$$\bar{H}_a = \gamma_0 H_a^\dagger \gamma_0 = [\gamma^\mu B^{*\dagger}_{a\mu} + i\gamma^5 B_a^\dagger]\frac{1+\slashed{v}}{2}, \qquad \text{(D1)}$$

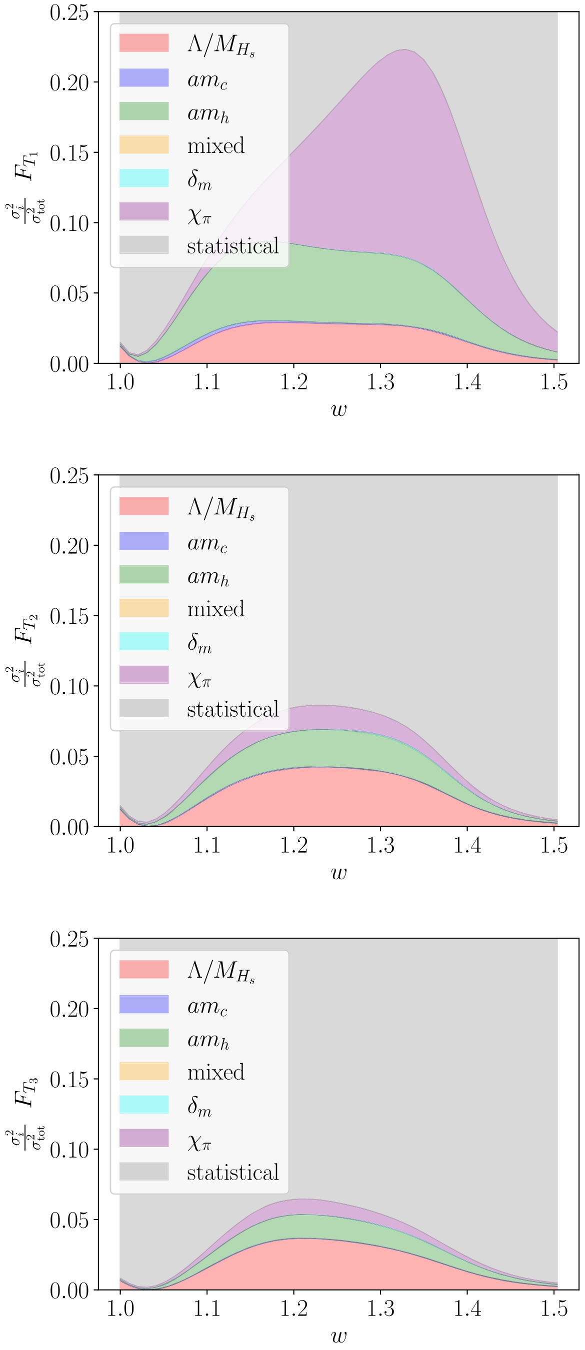

FIG. 22. Plots showing the fractional contribution of each source of uncertainty to the total variance for the $B \to D^*$ tensor form factors in the helicity basis defined in Eq. (32), across the full kinematic range. The vertical axis is truncated at 0.25 for clarity, with the remaining variance between 0.25 and 1 attributable to statistics. Note the large contribution of the unconstrained chiral dependence entering F_{T_1} that originates from h_{T_3}.

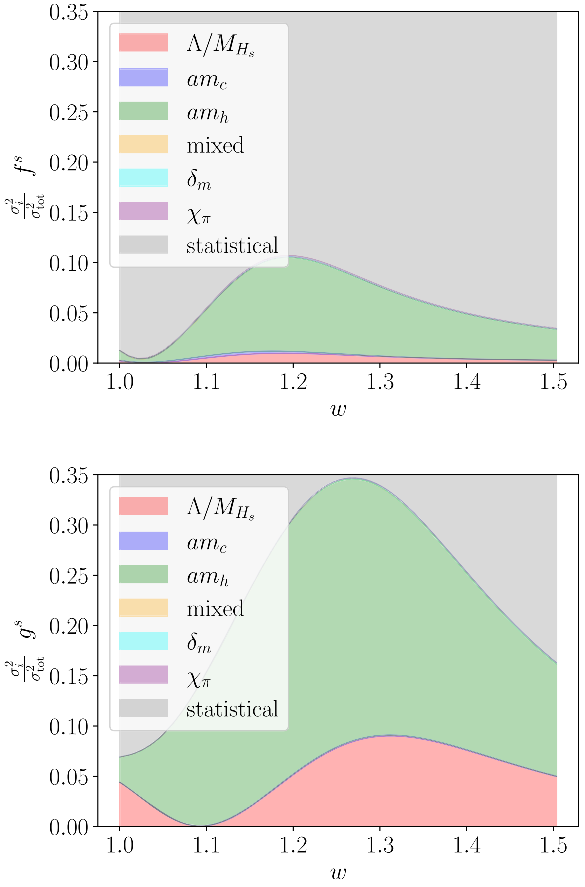

FIG. 23. Plots showing the fractional contribution of each source of uncertainty to the total variance for the $B_s \to D_s^*$ form factors f^s and g^s across the full kinematic range. The vertical axis is truncated at 0.35 for clarity, with the remaining variance between 0.35 and 1 attributable to statistics.

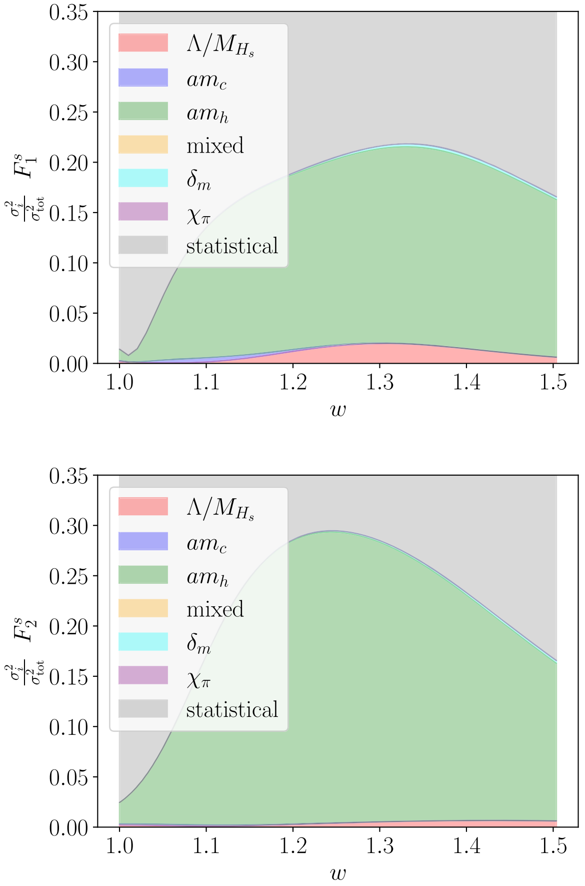

FIG. 24. Plots showing the fractional contribution of each source of uncertainty to the total variance for the $B_s \to D_s^*$ form factors F_1^s and F_2^s across the full kinematic range. The vertical axis is truncated at 0.35 for clarity, with the remaining variance between 0.35 and 1 attributable to statistics.

where a labels taste and flavor. The pion fields are

$$\Sigma = \exp\left(i\Phi/f\right), \tag{D2}$$

where

$$\Phi_{ab} = \Phi_{i\alpha,j\beta} = \pi_{ij,\Xi}\tilde{T}^{\Xi}_{\alpha\beta}, \tag{D3}$$

with Ξ labeling the taste of the pion and the $SU(4)$ taste generators $\tilde{T}^{\Xi} = \{\xi_5, i\xi_{\mu5}, i\xi_{\mu\nu}, \xi_\mu, \xi_I\}$. ξ_μ are the Euclidean gamma matrices, with $\xi_I = 1$, $\xi_{\mu\nu} = \frac{1}{2}[\xi_\mu, \xi_\nu]$, and $\xi_{\mu5} = \xi_\mu\xi_5$.

The leading order Minkowski staggered chiral Lagrangian for three flavors of light quarks is given by [72], including heavy quarks,

$$\begin{aligned}\mathcal{L}_\Sigma = {}& \frac{f^2}{8}\mathrm{STr}[\partial_\mu\Sigma\partial^\mu\Sigma^\dagger] + \frac{1}{4}\mu f^2\mathrm{STr}[\mathcal{M}\Sigma + \mathcal{M}\Sigma^\dagger] \\ & - \frac{2m_0}{3}(U_I + D_I + S_I)^2 - a^2\mathcal{V} \\ & - i\mathrm{tr}[\bar{H}_a v^\mu \partial_\mu H_a] + \mathrm{tr}[\bar{H}_a H_b] v^\mu V_\mu^{ba} \\ & + g_\pi \mathrm{tr}[\bar{H}_a H_b \gamma^\nu \gamma^5] A_\nu^{ba} + \frac{\lambda_2}{m_Q}\mathrm{tr}[\bar{H}_a \sigma^{\mu\nu} H_a \sigma_{\mu\nu}], \end{aligned} \tag{D4}$$

where U_I, D_I, and S_I are the diagonal elements of Φ. We use these rather than the physical basis in order to simplify the quark flow analysis. We will take $m_0 \to \infty$ at the end. We use "tr" to indicate a trace over dirac indices, and "STr" to indicate a trace over SU(4n) indices. The final term generates a mass splitting for the D^* and D,

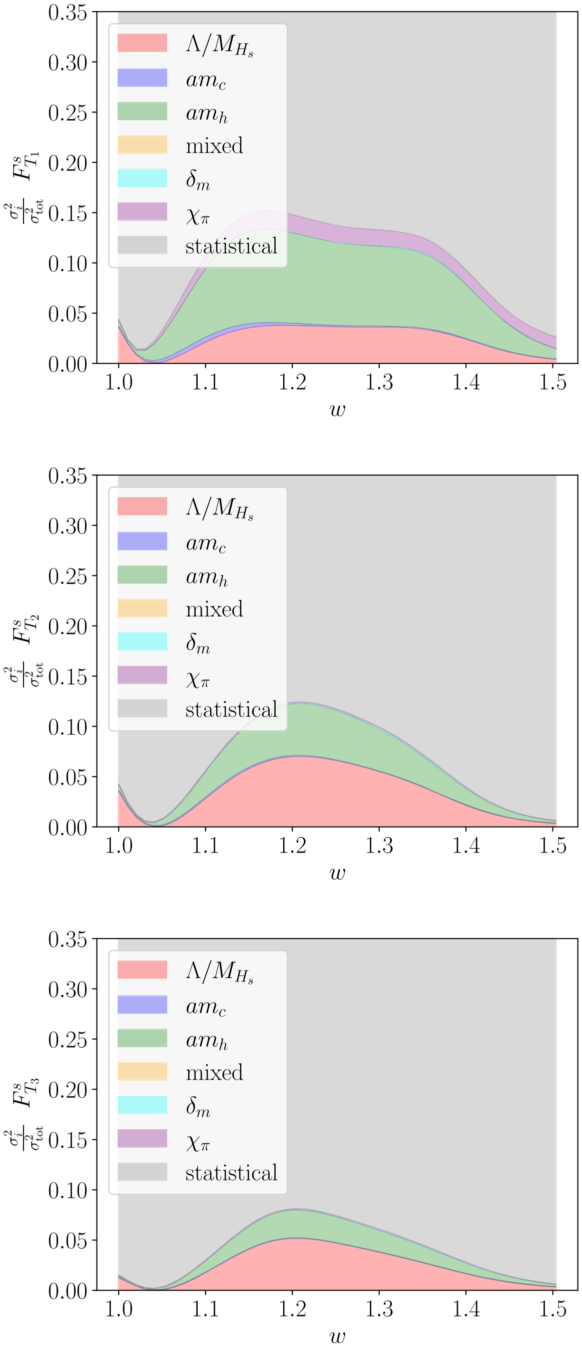

FIG. 25. Plots showing the fractional contribution of each source of uncertainty to the total variance for the $B_s \to D_s^*$ tensor form factors in the helicity basis defined in Eq. (32), across the full kinematic range. The vertical axis is truncated at 0.35 for clarity, with the remaining variance between 0.35 and 1 attributable to statistics. Note the large contribution of the unconstrained chiral dependence entering F_{T_1} that originates from h_{T_3}.

$\Delta^c = (m_{D^*} - m_D) = -\lambda_2/8m_c$. $\mathcal{V}$ contains operators that generate the taste splittings, as well as operators that mix the taste-(axial-)vector, flavor-neutral mesons. In Eq. (D4), A_μ and V_μ are constructed from the pion fields and couple to the heavy-meson fields. They are given by

$$V_\mu = \frac{i}{2}[\sigma^\dagger \partial_\mu \sigma + \sigma \partial_\mu \sigma^\dagger],$$
$$A_\mu = \frac{i}{2}[\sigma^\dagger \partial_\mu \sigma - \sigma \partial_\mu \sigma^\dagger], \tag{D5}$$

where $\sigma = \sqrt{\Sigma}$. At first order in the pion fields, these are

$$V_\mu^{i\alpha,j\beta} = 0 + \mathcal{O}(\pi^2),$$
$$A_\mu^{i\alpha,j\beta} = -\frac{1}{2f}\partial_\mu \pi_{ij,\Xi}\tilde{T}^\Xi_{\alpha\beta}.$$

Expanding Eq. (D4) to first order in the pion fields we find

$$\begin{aligned}\mathcal{L}^1_\Sigma = {}& \frac{1}{2}\partial_\mu \pi_{ij,\Xi}\partial^\mu \pi_{ji,\Xi} + \frac{1}{2}M^2_{ij,\Xi}\pi_{ij,\Xi}\pi_{ji,\Xi} \\ & - \frac{2m_0}{3}(U_I + D_I + S_I)^2 - a^2\mathcal{V}' - i\mathrm{tr}[\bar{H}_a v^\mu \partial_\mu H_a] \\ & - g_\pi \mathrm{tr}[\bar{H}_{j\beta} H_{i\alpha} \gamma^\nu \gamma^5]\frac{1}{2f}\partial_\mu \pi_{ij,\Xi}\tilde{T}^\Xi_{\alpha\beta} \\ & + \frac{\lambda_2}{m_Q}\mathrm{tr}[\bar{H}_a \sigma^{\mu\nu} H_a \sigma_{\mu\nu}],\end{aligned} \tag{D6}$$

where $M^2_{ij,\Xi} = \mu(m_i + m_j) + a^2\Delta_\Xi$ and $a^2\mathcal{V}'$ contains the remaining hairpin vertices mixing flavor-neutral taste vector and axial-vector pions. The pion propagator for flavor non-neutral pions is then

$$\{\pi_{ij,\Xi}\pi_{j'i',\Xi'}\}_{\rm con} = \frac{i\delta_{ii'}\delta_{jj'}\delta_{\Xi\Xi'}}{p^2 - M^2_{ij,\Xi} + i\varepsilon}. \tag{D7}$$

For vector, axial-vector, and singlet taste, flavor-neutral pions there is an additional disconnected hairpin contribution. In Minkowski space this is given by [72]

$$\{\pi_{ij,\Xi}\pi_{j'i',\Xi'}\}_{\rm disc} = \delta_{ij}\delta_{j'i'}\delta_{\Xi\Xi'}\mathcal{D}^\Xi_{ii,i'i'}, \tag{D8}$$

where

$$\mathcal{D}^{\Xi}_{ii,i'i'} = ia^2\delta'_{\Xi}\frac{(p^2 - m^2_{U\Xi})(p^2 - m^2_{D\Xi})(p^2 - m^2_{S\Xi})}{(p^2 - m^2_{ii\Xi})(p^2 - m^2_{i'i'\Xi})(p^2 - m^2_{\pi^0\Xi})(p^2 - m^2_{\eta\Xi})(p^2 - m^2_{\eta'\Xi})} \tag{D9}$$

such that

$$\{\pi_{ij,\Xi}\pi_{j'i',\Xi'}\} = \frac{i\delta_{ii'}\delta_{jj'}\delta_{\Xi\Xi'}}{p^2 - M^2_{ij,\Xi} + i\varepsilon} + \delta_{ij}\delta_{j'i'}\delta_{\Xi\Xi'}\mathcal{D}^{\Xi}_{ii,i'i'}. \tag{D10}$$

For $m_u = m_d$ relevant to $2 + 1 + 1$ simulations for $B \to D^*$ where the spectator quark is either a u or a d, the flavor-neutral disconnected propagator is

$$\begin{aligned}
\mathcal{D}^{\Xi}_{ii,i'i'} &= ia^2\delta'_{\Xi}\frac{(p^2 - m^2_{S\Xi})}{(p^2 - m^2_{\pi^0\Xi})(p^2 - m^2_{\eta\Xi})(p^2 - m^2_{\eta'\Xi})} \\
&= ia^2\delta'_{\Xi}\frac{m^2_{\pi^0\Xi} - m^2_{S\Xi}}{(m^2_{\pi^0\Xi} - m^2_{\eta\Xi})(m^2_{\pi^0\Xi} - m^2_{\eta'\Xi})}\frac{1}{p^2 - m^2_{\pi^0\Xi}} + ia^2\delta'_{\Xi}\frac{m^2_{\eta\Xi} - m^2_{S\Xi}}{(m^2_{\eta\Xi} - m^2_{\pi^0\Xi})(m^2_{\eta\Xi} - m^2_{\eta'\Xi})}\frac{1}{p^2 - m^2_{\eta\Xi}} \\
&\quad + ia^2\delta'_{\Xi}\frac{m^2_{\eta'\Xi} - m^2_{S\Xi}}{(m^2_{\eta'\Xi} - m^2_{\pi^0\Xi})(m^2_{\eta'\Xi} - m^2_{\eta\Xi})}\frac{1}{p^2 - m^2_{\eta'\Xi}} \\
&= ia^2\delta'_{\Xi}\left[A_{\Xi}\frac{1}{p^2 - m^2_{\pi^0\Xi} + i\varepsilon} + B_{\Xi}\frac{1}{p^2 - m^2_{\eta\Xi} + i\varepsilon} + C_{\Xi}\frac{1}{p^2 - m^2_{\eta'\Xi} + i\varepsilon}\right]
\end{aligned} \tag{D11}$$

for $i, i' = u, d$. For $B_s \to D_s^*$ we are interested in the case $i, i' = s$. In this case, using the fact that $M_{\pi_\Xi} = M_{U_\Xi} = M_{D_\Xi}$, we just swap $M_{\pi_\Xi} \leftrightarrow M_{S_\Xi}$ in Eq. (D11). We write the pion propagator as

$$\{\pi_{ij,\Xi}\pi_{j'i',\Xi'}\} = \delta_{\Xi\Xi'}\sum_n P^{\Xi,n}_{ii'jj'}\frac{i}{p^2 - M^2_{ij,\Xi,n} + i\varepsilon}, \tag{D12}$$

where

$$M^2_{ij,\Xi,n} = \begin{pmatrix} M^2_{ij,\Xi} \\ m^2_{\pi^0\Xi} \\ m^2_{\eta\Xi} \\ m^2_{\eta'\Xi} \end{pmatrix}_n \tag{D13}$$

and

$$P^{\Xi,n}_{ii'jj'} = \begin{pmatrix} \delta_{ii'}\delta_{jj'} \\ a^2\delta'_{\Xi}A_{\Xi}\delta_{ij}\delta_{j'i'} \\ a^2\delta'_{\Xi}B_{\Xi}\delta_{ij}\delta_{j'i'} \\ a^2\delta'_{\Xi}C_{\Xi}\delta_{ij}\delta_{j'i'} \end{pmatrix}_n. \tag{D14}$$

Here δ'_V, δ'_A are the parameters determined from $\mathcal{V}'$, $a^2\delta'_I = 4m_0^2/3$, and $\delta'_5 = \delta'_T = 0$.

The heavy meson propagators for the B, B^*, D, and D^* are given by

$$\begin{aligned}
\{B_a B_b^\dagger\} &= \{B_{i\alpha}B^\dagger_{j\beta}\} = \frac{i\delta_{ij}\delta_{\alpha\beta}}{2(v\cdot k + i\varepsilon)} \\
\{B^*_{a,\mu}B^{*\dagger}_{b,\nu}\} &= \{B^*_{i\alpha,\mu}B^{*\dagger}_{j\beta,\nu}\} = -\frac{i\delta_{ij}\delta_{\alpha\beta}(g_{\mu\nu} - v_\mu v_\nu)}{2(v\cdot k - \Delta^b + i\varepsilon)} \\
\{D_a D_b^\dagger\} &= \{D_{i\alpha}D^\dagger_{j\beta}\} = \frac{i\delta_{ij}\delta_{\alpha\beta}}{2(v\cdot k + i\varepsilon)} \\
\{D^*_{a,\mu}D^{*\dagger}_{b,\mu}\} &= \{D^*_{i\alpha,\mu}D^{*\dagger}_{j\beta,\nu}\} = -\frac{i\delta_{ij}\delta_{\alpha\beta}(g_{\mu\nu} - v_\mu v_\nu)}{2(v\cdot k - \Delta^c + i\varepsilon)}.
\end{aligned} \tag{D15}$$

Throughout the remainder of this section we will assume $\Delta^b = 0$ and write $\Delta^c = \Delta$. We can expand the $\bar{H}H\pi$ interaction from Eq. (D4):

$$\begin{aligned}
g_\pi \mathrm{tr}[\bar{H}_a H_b \gamma^\nu\gamma^5]A^{ba}_\nu &= i\frac{g_\pi}{f}\varepsilon^{\mu\kappa\lambda\nu}B^{*\dagger}_{i\alpha,\mu}B^*_{j\beta,\lambda}v_\kappa T^{\Xi}_{\beta\alpha}\partial_\nu\pi_{ji,\Xi} \\
&\quad + i\frac{g_\pi}{f}(B^{*\dagger}_{i\alpha,\lambda}B_{j\beta} - B^\dagger_{i\alpha}B^*_{j\beta,\lambda})T^{\Xi}_{\beta\alpha}\partial^\lambda\pi_{ji,\Xi}.
\end{aligned} \tag{D16}$$

Finally, we must add terms corresponding to the electroweak $b \to c$ current whose matrix elements we are interested in computing. These will take the form

$$-\epsilon(w)\mathrm{tr}[\bar{H}^{(c,v')}_a \Gamma H^{(b,v)}_a], \tag{D17}$$

where $w = v' \cdot v$ and $\epsilon(w)$ is the Isgur-Wise function. We define

$$-\epsilon(w)\mathrm{tr}[\bar{H}_a^{(c,v')}\Gamma H_a^{(b,v)}] = D_{a,\mu}^{*\dagger}\mathcal{J}^{\Gamma,\mu}B_a - D_a^{\dagger}\mathcal{J}^{\Gamma,\mu}B_{a,\mu}^{*} + D_{a,\mu}^{*\dagger}\mathcal{K}^{\Gamma,\mu\nu}B_{a,\nu}^{*} + D_a^{\dagger}\mathcal{P}^{\Gamma}B_a, \tag{D18}$$

where $\mathcal{J}$, $\mathcal{P}$, and $\mathcal{K}$ depend on v, v', and Γ. Note that $\mathcal{P}$ does not contribute at one-loop to the current corrections, since there is no $BB\pi$ coupling. $\mathcal{P}$ will only enter for $B \to D$ at tree level and multiplied by the wave function and current renormalization. $\mathcal{J}$, $\mathcal{P}$, and $\mathcal{K}$ maybe be computed straightforwardly for the currents of interest from standard γ-matrix trace methods.

1. Current renormalization

We will follow the conventions in Manohar and Wise [73] and write the renormalized operator of which we wish to compute the matrix elements as

$$\mathcal{O}_{\Gamma}^{R} = \frac{\sqrt{Z^B Z^{D^*}}}{Z_{\mathcal{O}}}\mathcal{O}_{\Gamma}. \tag{D19}$$

Here $\mathcal{O}_{\Gamma}$ is the local composite operator built from renormalized fields $\sqrt{Z^q}H_R^q = H_0^q$. We write this as

$$\mathcal{O}_{[\bar{H}^c\Gamma H^b]}^{R} = -\epsilon(w)\left(1 + \frac{1}{2}(\delta_{Z^B} + \delta_{Z^{D^*}}) - \delta_{Z_{\mathcal{O}}}\right) \times \mathrm{tr}[\bar{H}_a^{c,v'}\Gamma H_a^{b,v}]. \tag{D20}$$

Here we have defined $\delta_{Z_{\mathcal{O}}} = Z_{\mathcal{O}} - 1$ and, for the charm and bottom fields, $\delta_{Z^q} = Z^q - 1$.

The wave function renormalization of the B may be computed from the self-energy [72] $(1/2)\partial_{v\cdot p}\Sigma^B(v\cdot p)|_{v\cdot p=0} = \delta_{Z^B}$, where $-i\Sigma(p\cdot v)$ is the 1PI diagram with two external lines and with the overall identity in taste and flavor space removed. For the D^*, $(1/2)\partial_{v\cdot p}\Sigma^{D^*}(v\cdot p)|_{v\cdot p=\Delta} = \delta_{Z^{D^*}}$. Evaluating the Feynman diagram for the B self-energy we have

$$\Sigma^B = -i\left[\frac{g_\pi}{f}\right]^2 \int \frac{d^4k}{(2\pi)^4}\sum_{\Xi,\mathrm{in}} P_{uu,ii}^{\Xi,n}\frac{1}{k^2 - M_{ui,\Xi,n}^2 + i\varepsilon} \times \frac{k^\nu(g_{\mu\nu} - v_\mu v_\mu)k^\mu}{2(v\cdot(k+p) + i\varepsilon)}. \tag{D21}$$

We look just at the contribution of a single mass of pion, as the sum can be reinserted straightforwardly:

$$\Sigma_m^B = -i\left[\frac{g_\pi}{f}\right]^2 \int \frac{d^4k}{(2\pi)^4}\frac{1}{k^2 - m^2 + i\varepsilon}\frac{k^\nu(g_{\mu\nu} - v_\mu v_\mu)k^\mu}{2(v\cdot(k+p) + i\varepsilon)}. \tag{D22}$$

Following the notation of [59], we denote

$$\mathcal{I}_3(w,m,\Delta) = \int_0^\infty d\alpha \int \frac{d^4k}{(2\pi)^4}\frac{\alpha k^2}{[k^2 - (\alpha^2 + 2\alpha\Delta + m^2) + i\varepsilon]^3}, \tag{D23}$$

and find $\delta_{Z^B}^m = \frac{3}{2}i(g_\pi/f)^2\mathcal{I}_3(w,m,0)$. A similar calculation yields $\delta_{Z^{D^*}}^m = \frac{i}{2}(g_\pi/f)^2[\mathcal{I}_3(w,m,-\Delta) + 2\mathcal{I}_3(w,m,0)]$. The combination appearing in the current renormalization is then given by

$$\frac{1}{2}(\delta_{Z^B}^m + \delta_{Z^{D^*}}^m) = i\frac{1}{2}\left[\frac{g_\pi}{f}\right]^2 \times \left(\frac{1}{2}\mathcal{I}_3(w,m,-\Delta) + \frac{5}{2}\mathcal{I}_3(w,m,0)\right). \tag{D24}$$

2. One-loop matrix element contribution

The one-loop contribution to the matrix elements of $-\epsilon(w)\mathrm{tr}[H\bar{\Gamma}H]$ are given by the amputated on-shell two-point correlation functions in momentum space, contracted with the appropriate D^* polarization vector, $\epsilon_{\lambda'}(v')$, for which $\epsilon_{\lambda'}(v')v'^{\lambda'} = 0$. For $B \to D^*$ the current correction is given by

$$\left[\frac{g_\pi}{f}\right]^2 \int \frac{d^4k}{(2\pi)^4}\sum_{\Xi,\mathrm{in}} P_{uu,ii}^{\Xi,n}\frac{i}{k^2 - M_{ui,\Xi,n}^2 + i\varepsilon}\epsilon_{\lambda'}^{*} \times \left[\frac{i\epsilon_{\kappa\gamma\nu}^{\lambda'}v'^{\kappa}k^{\nu}}{2(v'\cdot k + i\varepsilon)}\mathcal{K}^{\Gamma,\gamma\rho}\frac{i(k_\rho - (k\cdot v)v_\rho)}{2(v\cdot k + i\varepsilon)} + \frac{ik^{\lambda'}}{2(v'\cdot k + \Delta + i\varepsilon)}\mathcal{J}^{\Gamma,\rho}\frac{i(k_\rho - (k\cdot v)v_\rho)}{2(v\cdot k + i\varepsilon)}\right]. \tag{D25}$$

Here we have left implicit that we will divide sea quark loops by a factor of 4 to reduce the number of tastes from 4 to 1. Noting that the sum over tastes and hairpin terms may be straightforwardly reinserted, we evaluate the contribution of a single mass,

$$\left[\frac{g_\pi}{f}\right]^2 \int \frac{d^4k}{(2\pi)^4}\frac{i}{k^2 - m^2 + i\varepsilon}\epsilon_{\lambda'}^{*} \times \left[\frac{i\epsilon_{\kappa\gamma\nu}^{\lambda'}v'^{\kappa}k^{\nu}}{2(v'\cdot k + i\varepsilon)}\mathcal{K}^{\Gamma,\gamma\rho}\frac{i(k_\rho - (k\cdot v)v_\rho)}{2(v\cdot k + i\varepsilon)} + \frac{ik^{\lambda'}}{2(v'\cdot k + \Delta + i\varepsilon)}\mathcal{J}^{\Gamma,\rho}\frac{i(k_\rho - (k\cdot v)v_\rho)}{2(v\cdot k + i\varepsilon)}\right]. \tag{D26}$$

For the currents considered here, these may all be expressed in terms of the integral

$$\int \frac{d^4k}{(2\pi)^4} \frac{1}{2(v' \cdot k - \Delta + i\varepsilon)} \frac{1}{2(v \cdot k + i\varepsilon)} \frac{k^\delta k^\nu}{k^2 - m^2 + i\varepsilon} = \frac{1}{2}\mathcal{I}_1(w,m,\Delta) g^{\delta\nu} + \frac{1}{2}\mathcal{I}_2(w,m,\Delta) v'^\delta v^\nu + \cdots, \tag{D27}$$

where only the $\mathcal{I}_1$ contains a UV divergence and the … indicate terms which give zero when summing over Lorentz indices. These definitions for the integrals match those given by Chow *et al.* [59]. They include a factor of $i/16\pi^2$ that has been removed from the definitions used in Appendix A of [26] that has $I = \mathcal{I}^{\mathrm{FNAL}} = i16\pi^2 \times \mathcal{I}^{\mathrm{Chow}}$. We will adopt the conventions in Appendix A of [26]. With these conventions we have

$$\frac{1}{2}(\delta^m_{Z^B} + \delta^m_{Z^{D^*}}) = \frac{1}{2}\left[\frac{g_\pi}{4\pi f}\right]^2 \times \left(\frac{1}{2} I_3(w,m,-\Delta/m) + \frac{5}{2} I_3(w,m,0)\right). \tag{D28}$$

This yields a total one-loop current correction for $B \to D^*$, for a single pion mass,

$$\begin{aligned} &\frac{-1}{2}\left[\frac{g_\pi}{4\pi f}\right]^2 \epsilon^*_{\lambda'} \big[I_1(w,m,0)\epsilon^{\lambda'}_{\kappa\gamma\nu} v'^\kappa (\mathcal{K}^{\Gamma,\gamma\nu} - \mathcal{K}^{\Gamma,\gamma\rho} v_\rho v^\nu) \\ &\quad + I_1(w,m,-\Delta/m)(\mathcal{J}^{\Gamma,\lambda'} - \mathcal{J}^{\Gamma,\rho} v_\rho v^{\lambda'}) \\ &\quad + I_2(w,m,0)\epsilon^{\lambda'}_{\kappa\gamma\nu} v'^\kappa v^\nu (\mathcal{K}^{\Gamma,\gamma\rho} v'_\rho - w\mathcal{K}^{\Gamma,\gamma\rho} v_\rho) \\ &\quad + I_2(w,m,-\Delta/m) v^{\lambda'} (\mathcal{J}^{\Gamma,\rho} v'_\rho - w\mathcal{J}^{\Gamma,\rho} v_\rho)\big]. \end{aligned} \tag{D29}$$

For $B \to D$ this procedure gives the one-loop current correction for a single pion mass

$$\begin{aligned} &\frac{1}{2}\left[\frac{g_\pi}{4\pi f}\right]^2 \big[I_1(w,m,\Delta)\mathcal{K}^{\Gamma,\gamma\rho}(g_{\gamma\rho}/2 + w v_\rho v'_\gamma) \\ &\quad + I_2(w,m,\Delta)\mathcal{K}^{\Gamma,\gamma\rho}(v'_\rho - w v_\rho)(v_\gamma - w v'_\gamma)\big]. \end{aligned} \tag{D30}$$

We evaluate $\mathcal{K}$, $\mathcal{J}$, and $\mathcal{P}$ for $\Gamma = \gamma^i, \gamma^5\gamma^i$, and $\sigma^{\alpha\beta}$ corresponding to the vector, axial-vector, and tensor currents, respectively. Defining $\delta^m_{h_X}$ as the deviation from the tree level value resulting from loops including a pion m, we find, dropping $\delta_{Z_\mathcal{O}}$ and including only the finite parts of the integrals regularized using dimensional regularization,

$$\begin{aligned} \delta^m_{h_{A_1}}/\varepsilon(w) &= \frac{1}{2}(\delta^m_{Z^c} + \delta^m_{Z^b}) - \frac{1}{2}\left[\frac{g_\pi}{4\pi f}\right]^2 \big((1+w)I_1(w,m,0) + I_1(w,m,-\Delta/m) + (w^2-1)I_2(w,m,0)\big) \\ &= -\frac{1}{2}\left[\frac{g_\pi}{4\pi f}\right]^2 \bigg(-\frac{1}{2}I_3(w,m,-\Delta/m) - \frac{5}{2}I_3(w,m,0) + (1+w)I_1(w,m,0) + I_1(w,m,-\Delta/m) \\ &\qquad + (w^2-1)I_2(w,m,0)\bigg) \\ &= \frac{1}{4}\frac{g_\pi^2}{16\pi^2 f^2} F^{h_{A_1}}(w,m,-\Delta/m), \end{aligned} \tag{D31}$$

$$\begin{aligned} \delta^m_{h_{A_2}}/\varepsilon(w) &= -\frac{1}{2}\left[\frac{g_\pi}{4\pi f}\right]^2 \big(I_1(w,m,-\Delta/m) - I_1(w,m,0) + (w+1)I_2(w,m,-\Delta/m) - (1+w)I_2(w,m,0)\big) \\ &= \frac{1}{4}\frac{g_\pi^2}{16\pi^2 f^2} F^{h_{A_2}}(w,m,-\Delta/m) \\ \delta^m_{h_{A_3}} &= \delta^m_{h_{A_1}} - \delta^m_{h_{A_2}} \\ \delta^m_{h_V} &= \delta^m_{h_{A_1}} \end{aligned} \tag{D32}$$

and for the tensor current

$$\begin{aligned}
\delta^m_{h_{T_1}}/\varepsilon(w) &= \frac{1}{2}(\delta^m_{Z^c}+\delta^m_{Z^b}) - \frac{1}{2}\left[\frac{g_\pi}{4\pi f}\right]^2\big((1+w)I_1(w,m,0)+I_1(w,m,-\Delta/m)+(w^2-1)I_2(w,m,0)\big) \\
&= -\frac{1}{2}\left[\frac{g_\pi}{4\pi f}\right]^2\left(-\frac{1}{2}I_3(w,m,-\Delta/m)-\frac{5}{2}I_3(w,m,0)+(1+w)I_1(w,m,0)+I_1(w,m,-\Delta/m)+(w^2-1)I_2(w,m,0)\right) \\
&= \delta^m_{h_{A_1}}/\varepsilon(w) \\
\delta^m_{h_{T_2}}/\varepsilon(w) &= 0 \\
\delta^m_{h_{T_3}}/\varepsilon(w) &= -\frac{1}{2}\left[\frac{g_\pi}{4\pi f}\right]^2\Big((I_1(w,m,-\Delta/m)-I_1(w,m,0))-(w+1)I_2(w,m,0)+(1+w)I_2(w,m,-\Delta/m)\Big) \\
&= \delta^m_{h_{A_2}}/\varepsilon(w).
\end{aligned} \tag{D33}$$

Here we have defined the quantities $F^{h_{A_i}}(w,m,-\Delta/m)$ to match those given in [26]:

$$\begin{aligned}
F^{h_{A_1}}(w,m,x) &= -2\left[I_1(w,m,x)-\frac{1}{2}I_3(w,m,x)+(w+1)I_1(w,m,0)+(w^2-1)I_2(w,m,0)-\frac{5}{2}I_3(w,m,0)\right], \\
F^{h_{A_2}}(w,m,x) &= -2\big[I_1(w,m,x)+(w+1)I_2(w,m,x)-I_1(w,m,0)-(w+1)I_2(w,m,0)\big], \\
F^{h_{A_3}}(w,m,x) &= F^{h_{A_1}}(w,m,x)-F^{h_{A_2}}(w,m,x).
\end{aligned} \tag{D34}$$

We also have the tree level values $h^{\rm tree}_{A_1} = h^{\rm tree}_{A_3} = h^{\rm tree}_{V} = h^{\rm tree}_{T_1} = \varepsilon(w)$ and $h^{\rm tree}_{A_2} = h^{\rm tree}_{T_2} = h^{\rm tree}_{T_3} = 0$. With these definitions we have

$$h_X = \left(h^{\rm tree}_X + \sum_{\Xi,{\rm in}} P^{\Xi,n}_{uu,ii}\delta^{M_{ui,\Xi,n}}_{h_X}\right). \tag{D35}$$

Since the sum over tastes acts in the same way for different form factors, we find

$$\begin{aligned}
h_{T_1} &= h_{A_1} \\
h_{T_2} &= 0 \\
h_{T_3} &= h_{A_2}.
\end{aligned} \tag{D36}$$

We also find for $B \to D$ that $f_T = f_+$ and confirm the one-loop relation $h_{A_1} = h_V$ and $f_- = 0$.

3. Chiral logarithms

Denoting $F^{h_Y}(w,m_j,-\Delta/m_j) = \bar{F}^Y_j$ as in [26], the sum in Eq. (D35) over n and i gives

$$\begin{aligned}
\delta_{h_X} &= \frac{g_\pi^2}{16\pi^2 f^2}\sum_{\Xi,{\rm in}} P^{\Xi,n}_{uu,ii}\frac{1}{4}\bar{F}^Y_{ui,\Xi,n} \\
&= \frac{g_\pi^2}{16\pi^2 f^2}\times\left(\frac{1}{4}\sum_{\Xi}(2\bar{F}^Y_{\pi_\Xi}+\bar{F}^Y_{K_\Xi})\right)+\frac{1}{4}\sum_{\Xi}a^2\delta'_\Xi\left[A_\Xi\bar{F}^Y_{\pi^0_\Xi}+B_\Xi\bar{F}^Y_{\eta_\Xi}+C_\Xi\bar{F}^Y_{\eta'_\Xi}\right] \\
&= \frac{g_\pi^2}{16\pi^2 f^2}\times\left(\frac{1}{4}\sum_{\Xi}(2\bar{F}^Y_{\pi_\Xi}+\bar{F}^Y_{K_\Xi})\right)+\sum_{\Xi=A,V}a^2\delta'_\Xi\left[A_\Xi\bar{F}^Y_{\pi^0_\Xi}+B_\Xi\bar{F}^Y_{\eta_\Xi}+C_\Xi\bar{F}^Y_{\eta'_\Xi}\right]+\frac{m_0^2}{3}\left[A_I\bar{F}^Y_{\pi^0_I}+B_I\bar{F}^Y_{\eta_I}+C_I\bar{F}^Y_{\eta'_I}\right],
\end{aligned} \tag{D37}$$

where A, B, and C are defined as in Eq. (D11). Following [61] to move from $4+4+4$ to $1+1+1$ flavor tastes of light quark, we find after taking $m_0 \to \infty$,

$$\delta_{h_X} = \left(\frac{g_\pi^2}{16\pi^2 f^2}\right)\left[\frac{1}{16}\sum_{\Xi}(2\bar{F}^Y_{\pi_\Xi} + \bar{F}^Y_{K_\Xi}) - \frac{1}{2}\bar{F}^Y_{\pi_I} + \frac{1}{6}\bar{F}^Y_{\eta_I} + \sum_{\Xi=V,A} a^2\delta_\Xi\left(\frac{m^2_{S_\Xi} - m^2_{\pi^0_\Xi}}{(m^2_{\eta_\Xi} - m^2_{\pi^0_\Xi})(m^2_{\pi^0_\Xi} - m^2_{\eta'_\Xi})}\bar{F}^Y_{\pi_\Xi} + \frac{m^2_{\eta_\Xi} - m^2_{S_\Xi}}{(m^2_{\eta_\Xi} - m^2_{\pi^0_\Xi})(m^2_{\eta_\Xi} - m^2_{\eta'_\Xi})}\bar{F}^Y_{\eta_\Xi} + \frac{m^2_{S_\Xi} - m^2_{\eta'_\Xi}}{(m^2_{\pi^0_\Xi} - m^2_{\eta'_\Xi})(m^2_{\eta'_\Xi} - m^2_{\eta_\Xi})}\bar{F}^Y_{\eta'_\Xi}\right)\right], \tag{D38}$$

where we have used the relations given in [60] for the flavor-neutral pion mass eigenstates. Note that our results here differ from those given in [26] by an overall factor of 3. We have checked that our results match those in [59] for h_{A_1}, h_{A_2}, and h_{A_3}, and we have also checked that our zero recoil results match those in [60]. The chiral logarithms, $\mathrm{logs}^Y_{SU(3)}$, in Eq. (21), for $B \to D^*$ thus take the form

$$\mathrm{logs}^Y_{SU(3)} = \frac{1}{16}\sum_{\Xi}(2\bar{F}^Y_{\pi_\Xi} + \bar{F}^Y_{K_\Xi}) - \frac{1}{2}\bar{F}^Y_{\pi_I} + \frac{1}{6}\bar{F}^Y_{\eta_I} + \sum_{\Xi=V,A} a^2\delta_\Xi\left(\frac{m^2_{S_\Xi} - m^2_{\pi^0_\Xi}}{(m^2_{\eta_\Xi} - m^2_{\pi^0_\Xi})(m^2_{\pi^0_\Xi} - m^2_{\eta'_\Xi})}\bar{F}^Y_{\pi_\Xi} + \frac{m^2_{\eta_\Xi} - m^2_{S_\Xi}}{(m^2_{\eta_\Xi} - m^2_{\pi^0_\Xi})(m^2_{\eta_\Xi} - m^2_{\eta'_\Xi})}\bar{F}^Y_{\eta_\Xi} + \frac{m^2_{S_\Xi} - m^2_{\eta'_\Xi}}{(m^2_{\pi^0_\Xi} - m^2_{\eta'_\Xi})(m^2_{\eta'_\Xi} - m^2_{\eta_\Xi})}\bar{F}^Y_{\eta'_\Xi}\right) \tag{D39}$$

and for $B_s \to D_s^*$ a similar calculation gives the logs

$$\mathrm{logs}^{Y^s}_{SU(3)} = \frac{1}{16}\sum_{\Xi}(2\bar{F}^Y_{K_\Xi} + \bar{F}^Y_{S_\Xi}) - \bar{F}^Y_{S_I} + \frac{2}{3}\bar{F}^Y_{\eta_I} + \sum_{\Xi=V,A} a^2\delta_\Xi\left(\frac{m^2_{S_\Xi} - m^2_{\pi^0_\Xi}}{(m^2_{S_\Xi} - m^2_{\eta_\Xi})(m^2_{S_\Xi} - m^2_{\eta'_\Xi})}\bar{F}^Y_{S_\Xi} + \frac{m^2_{\eta_\Xi} - m^2_{\pi_\Xi}}{(m^2_{\eta_\Xi} - m^2_{S_\Xi})(m^2_{\eta_\Xi} - m^2_{\eta'_\Xi})}\bar{F}^Y_{\eta_\Xi} + \frac{m^2_{\eta'_\Xi} - m^2_{\pi_\Xi}}{(m^2_{\eta'_\Xi} - m^2_{S_\Xi})(m^2_{\eta'_\Xi} - m^2_{\eta_\Xi})}\bar{F}^Y_{\eta'_\Xi}\right). \tag{D40}$$

The chiral logarithms are most sensitive to variation of the pion and $\eta_{V,A}$ masses, and the effect of the taste splittings and hairpin contributions is most pronounced near the "cusp" $m_\pi \approx \Delta$, which roughly coincides with the physical pion mass. The sum over tastes appearing in Eq. (D39) acts to wash out the cusp, averaging over the masses of the different tastes [60]. This effect is somewhat mitigated for HISQ quarks by the fact that the taste splittings are all approximately proportional [47], with $M^2_{\pi_\xi} - M^2_{\pi_5} \approx n_\xi a^2 \delta_t$, where $n_A = 1$, $n_T = 2$, $n_V = 3$, and $n_I = 4$.

We can analyze the effect of taste splittings by expanding the pion log terms to first order in a^2, and dropping terms proportional to $a^2\bar{F}^Y_{\pi_5}$ that produce only normal discretization effects. This gives

$$\mathrm{logs}^Y_{SU(3)} \approx a^2(2\delta_t + \delta'_V + \delta'_A)\frac{\partial \bar{F}^Y_{\pi_5}}{\partial m^2_{\pi_5}}. \tag{D41}$$

Together with the approximate relation, $\delta'_V + \delta'_A \approx -2\delta_t$, for HISQ [51,62], this leading order correction is suppressed so there is no nonanalytic behavior in a. This matches what was seen in [62], where a similar approximate cancellation of leading order taste splitting and hairpin terms was seen. Note, however, that in our fits we use the full expressions given in Eqs. (D39) and (D40).

APPENDIX E: COMPARISON TO PREVIOUS HPQCD $B_s \to D_s^*$ FORM FACTORS

In Figs. 26 and 27 we plot our previous results for $B_s \to D_s^*$ from [23] together with the updated form factors given in this work. We see good agreement for the form factors h_{A_1} and h_V and some differences for the form factors h_{A_2} and h_{A_3}. The improved calculation presented here has the addition of a physical ensemble with $a \approx 0.06$ fm, set 5, and includes the additional $B \to D^*$ correlator data that informs the $B_s \to D_s^*$ form factors through our chiral extrapolation. Additionally, in this work we adopt the time source binning strategy described in Appendix B, providing improved resolution of the correlator covariance matrices. Reference [23] also used a BGL-like parametrization to describe the kinematic dependence of the form factors, compared to the simpler expression in powers of $(w - 1)$ used here. Plots showing form factor results for $B \to D^*$ resulting from both separate and simultaneous fit results are included in the Supplemental Material, where we see that fitting $B \to D^*$ separately produces very similar form factor results for $B \to D^*$ to the simultaneous fit described in Sec. IV B. We have also confirmed that fitting the $B_s \to D_s^*$ in isolation produces very similar form factor results to the simultaneous fit.

Further investigation of the differences for $B_s \to D_s^*$ between this work and [23] found that the choice of ΔT_{2pt} in that work, for correlator fits on set 3, was too small, and that this resulted in excited state contamination which shifted the extracted matrix elements on set 3 upwards by $\approx 1\sigma$. However, this had little impact on the final form factors. Instead the differences seen in h_{A_2} and h_{A_3} arise from the differences in the fit forms used for the

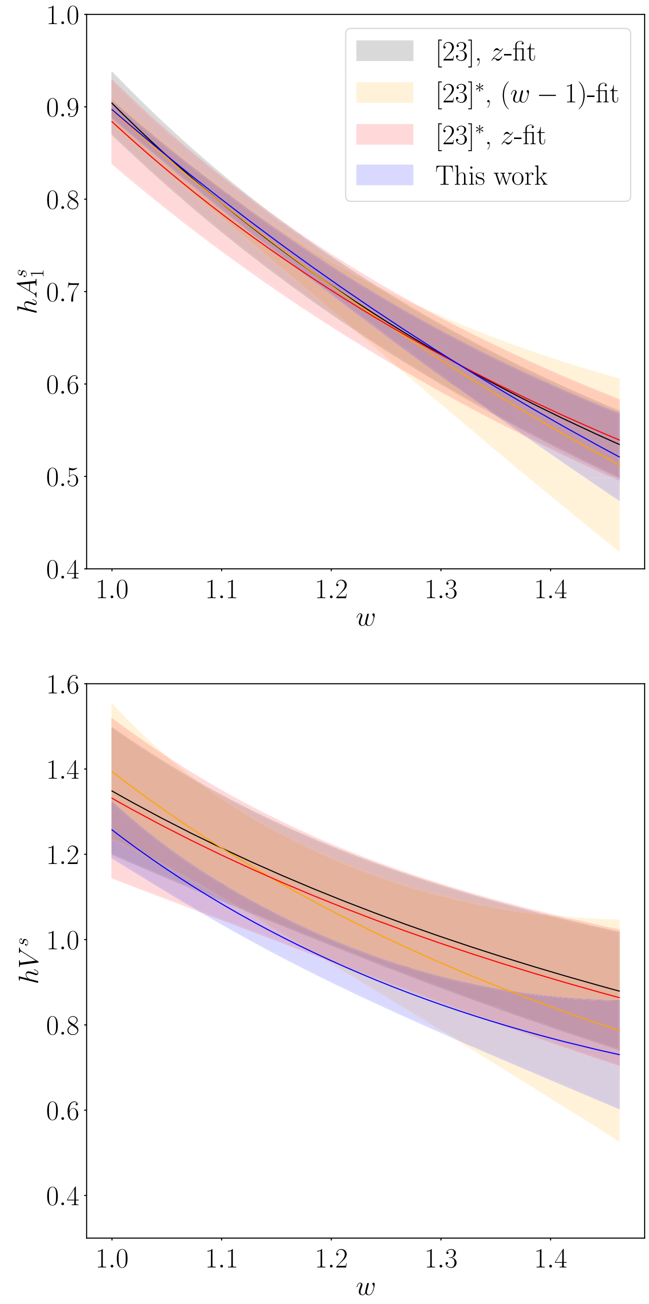

FIG. 26. $B_s \to D_s^*$ HQET basis form factors h_{A_1} and h_V. We show the results of this work as a blue band, compared to the results of [23] given as a gray hatched band. We also include a red band, labeled [23]*, showing the result that would have been obtained in [23] if $\Delta T_{2\mathrm{pt}} = 12$ had been used on set 3 of that work. Finally, in yellow, we include the result of fitting the form factor data of [23], with larger $\Delta T_{2\mathrm{pt}}$ on set 3, using the fit function Eq. (21). Here, we see that both datasets produce consistent results for each chiral-continuum fit function.

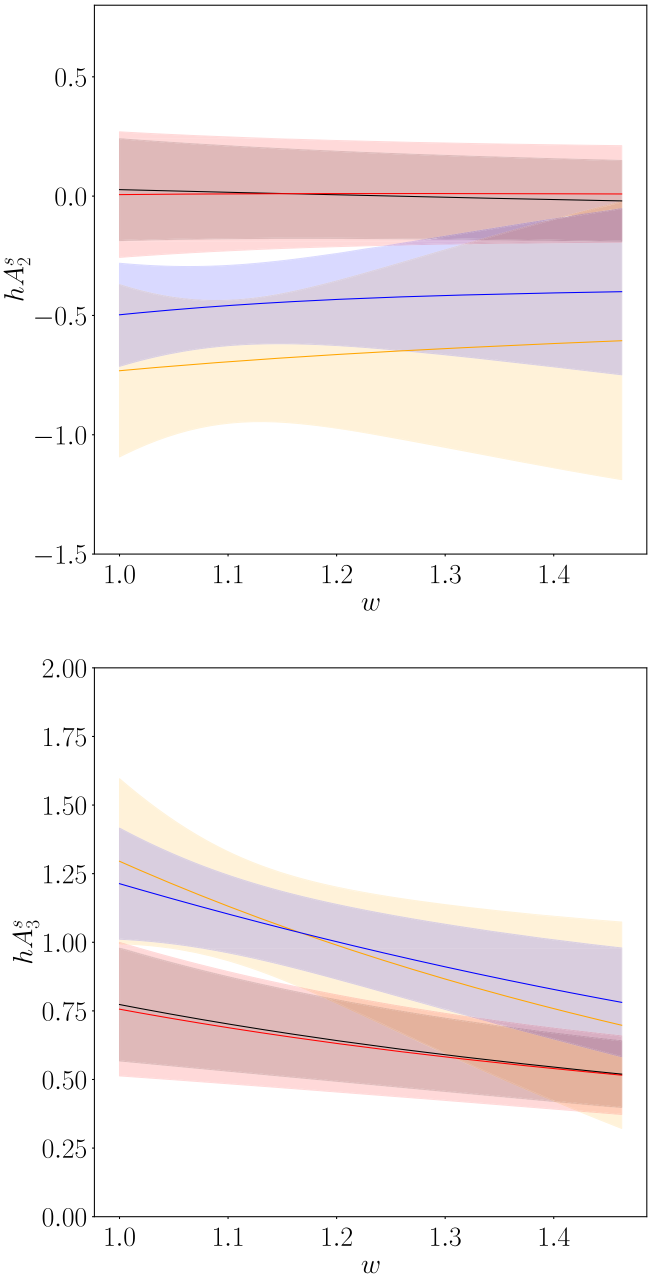

FIG. 27. $B_s \to D_s^*$ HQET basis form factors h_{A_2} and h_{A_3}. We show the results of this work as a blue band, compared to the results of [23] given as a gray band. We also include a red band, labeled [23]*, showing the result that would have been obtained in [23] if $\Delta T_{2\mathrm{pt}} = 12$ had been used on set 3 of that work. Finally, in yellow, we include the result of fitting the form factor data of [23], with larger $\Delta T_{2\mathrm{pt}}$ on set 3, using the fit function Eq. (21). Here, we see that both datasets produce consistent results for each chiral continuum fit function and the differences arise from the differences in the fit functions.

chiral-continuum extrapolation. We see that applying the chiral-continuum extrapolation used in [23] to the $B_s \to D_s^*$ dataset used in this work, excluding set 5, results in similar form factors to those given in this work, except for h_{A_2} and h_{A_3}, where ≈1–2σ differences are seen. The same picture emerges if we apply the chiral-continuum fit used here to the dataset used in [23]. We include in Figs. 26 and 27 the results that would have been obtained in [23] if $\Delta T_{2\mathrm{pt}} = 12$

had been used on set 3 of that work, as well as the result of fitting that corrected data using the chiral continuum fit function given in Eq. (21). We see that the results for h_{A_1} and h_V are largely insensitive to the fitting scheme, but the noisier form factors h_{A_2} and h_{A_3} are sensitive to the choice of fit function at the level of a few σ relative to the statistical and systematic uncertainties.

We conclude that the $\approx$1–2σ differences between this work and [23] seen for h_{A_2} and h_{A_3} are a result of the much more conservative description of kinematic dependence of the form factors used in this work (Sec. IV B) and the use of a z expansion in [23] whose form led to some bias in the shape of the continuum form factors and an underestimation of some uncertainties.

[1] B. Chakraborty, W. G. Parrott, C. Bouchard, C. T. H. Davies, J. Koponen, and G. P. Lepage, Phys. Rev. D **104**, 034505 (2021).
[2] A. Bazavov *et al.*, Phys. Rev. D **98**, 074512 (2018).
[3] P. Zyla *et al.* (Particle Data Group), Prog. Theor. Exp. Phys. **2020**, 083C01 (2020).
[4] P. Gambino, Int. J. Mod. Phys. A **30**, 1543002 (2015).
[5] M. Bordone, B. Capdevila, and P. Gambino, Phys. Lett. B **822**, 136679 (2021).
[6] J. A. Bailey *et al.* (Fermilab Lattice, MILC Collaborations), Phys. Rev. D **89**, 114504 (2014).
[7] J. Harrison, C. Davies, and M. Wingate (HPQCD Collaboration), Phys. Rev. D **97**, 054502 (2018).
[8] E. McLean, C. Davies, J. Koponen, and A. Lytle, Phys. Rev. D **101**, 074513 (2020).
[9] E. McLean, C. T. H. Davies, A. T. Lytle, and J. Koponen, Phys. Rev. D **99**, 114512 (2019).
[10] Y. Amhis *et al.* (HFLAV Collaboration), Phys. Rev. D **107**, 052008 (2023).
[11] J. A. Bailey *et al.* (MILC Collaboration), Phys. Rev. D **92**, 034506 (2015).
[12] I. Caprini, L. Lellouch, and M. Neubert, Nucl. Phys. **B530**, 153 (1998).
[13] C. Boyd, B. Grinstein, and R. F. Lebed, Phys. Rev. D **56**, 6895 (1997).
[14] D. Bigi, P. Gambino, and S. Schacht, J. High Energy Phys. 11 (2017) 061.
[15] B. Grinstein and A. Kobach, Phys. Lett. B **771**, 359 (2017).
[16] D. Bigi and P. Gambino, Phys. Rev. D **94**, 094008 (2016).
[17] A. Abdesselam *et al.* (Belle Collaboration), arXiv:1702.01521.
[18] D. Bigi, P. Gambino, and S. Schacht, Phys. Lett. B **769**, 441 (2017).
[19] M. Bordone, M. Jung, and D. van Dyk, Eur. Phys. J. C **80**, 74 (2020).
[20] S. Jaiswal, S. Nandi, and S. K. Patra, J. High Energy Phys. 12 (2017) 060.
[21] E. Waheed *et al.* (Belle Collaboration), Phys. Rev. D **100**, 052007 (2019); **103**, 079901(E) (2021).
[22] J. Harrison, C. T. H. Davies, and A. Lytle (HPQCD Collaboration), Phys. Rev. D **102**, 094518 (2020).
[23] J. Harrison and C. T. H. Davies (HPQCD Collaboration), Phys. Rev. D **105**, 094506 (2022).
[24] E. Follana, Q. Mason, C. Davies, K. Hornbostel, G. P. Lepage, J. Shigemitsu, H. Trottier, and K. Wong (HPQCD, UKQCD Collaborations), Phys. Rev. D **75**, 054502 (2007).
[25] R. Aaij *et al.* (LHCb Collaboration), Phys. Rev. D **101**, 072004 (2020).
[26] A. Bazavov *et al.* (Fermilab Lattice, MILC, Fermilab Lattice, MILC Collaborations), Eur. Phys. J. C **82**, 1141 (2022); **83**, 21(E) (2023).
[27] A. X. El-Khadra, A. S. Kronfeld, and P. B. Mackenzie, Phys. Rev. D **55**, 3933 (1997).
[28] J. P. Lees *et al.* (*BABAR* Collaboration), Phys. Rev. Lett. **123**, 091801 (2019).
[29] T. Kaneko, Y. Aoki, G. Bailas, B. Colquhoun, H. Fukaya, S. Hashimoto, and J. Koponen (JLQCD Collaboration), Proc. Sci. LATTICE2019 (**2019**) 139.
[30] T. Kaneko, Y. Aoki, B. Colquhoun, M. Faur, H. Fukaya, S. Hashimoto, J. Koponen, and E. Kou, Proc. Sci. LATTICE2021 (**2022**) 561.
[31] G. Martinelli, S. Simula, and L. Vittorio, Phys. Rev. D **105**, 034503 (2022).
[32] P. Gambino, M. Jung, and S. Schacht, Phys. Lett. B **795**, 386 (2019).
[33] J. P. Lees *et al.* (*BABAR* Collaboration), Phys. Rev. D **88**, 072012 (2013).
[34] G. Caria *et al.* (Belle Collaboration), Phys. Rev. Lett. **124**, 161803 (2020).
[35] R. Aaij *et al.* (LHCb Collaboration), Phys. Rev. D **97**, 072013 (2018).
[36] D. Bečirević, M. Fedele, I. Nišandžić, and A. Tayduganov, arXiv:1907.02257.
[37] M. Bordone, N. Gubernari, D. van Dyk, and M. Jung, Eur. Phys. J. C **80**, 347 (2020).
[38] S. Hirose *et al.* (Belle Collaboration), Phys. Rev. D **97**, 012004 (2018).
[39] A. Abdesselam *et al.* (Belle Collaboration), in *10th International Workshop on the CKM Unitarity Triangle* (2019), arXiv:1903.03102.
[40] L. J. Cooper, C. T. H. Davies, and M. Wingate (HPQCD Collaboration), Phys. Rev. D **105**, 014503 (2022).
[41] W. G. Parrott, C. Bouchard, and C. T. H. Davies, Phys. Rev. D **107**, 014511 (2023).
[42] D. Hatton, C. T. H. Davies, G. P. Lepage, and A. T. Lytle (HPQCD Collaboration), Phys. Rev. D **102**, 094509 (2020).
[43] F. U. Bernlochner, Z. Ligeti, M. Papucci, and D. J. Robinson, Phys. Rev. D **95**, 115008 (2017); **97**, 059902 (E) (2018).
[44] T. D. Cohen, H. Lamm, and R. F. Lebed, Phys. Rev. D **98**, 034022 (2018).

[45] J. Harrison, C. T. H. Davies, and A. Lytle (LATTICE-HPQCD Collaboration), Phys. Rev. Lett. **125**, 222003 (2020).

[46] A. Bazavov *et al.* (MILC Collaboration), Phys. Rev. D **82**, 074501 (2010).

[47] A. Bazavov *et al.* (MILC Collaboration), Phys. Rev. D **87**, 054505 (2013).

[48] D. Hatton, C. T. H. Davies, B. Galloway, J. Koponen, G. P. Lepage, and A. T. Lytle (HPQCD Collaboration), Phys. Rev. D **102**, 054511 (2020).

[49] L. Randall and M. B. Wise, Phys. Lett. B **303**, 135 (1993).

[50] S. Borsanyi *et al.*, J. High Energy Phys. 09 (2012) 010.

[51] R. J. Dowdall, C. T. H. Davies, G. P. Lepage, and C. McNeile, Phys. Rev. D **88**, 074504 (2013).

[52] B. Chakraborty, C. T. H. Davies, P. G. de Oliviera, J. Koponen, G. P. Lepage, and R. S. Van de Water, Phys. Rev. D **96**, 034516 (2017).

[53] B. Chakraborty, C. T. H. Davies, B. Galloway, P. Knecht, J. Koponen, G. C. Donald, R. J. Dowdall, G. P. Lepage, and C. McNeile, Phys. Rev. D **91**, 054508 (2015).

[54] C. T. Sachrajda and G. Villadoro, Phys. Lett. B **609**, 73 (2005).

[55] D. Guadagnoli, F. Mescia, and S. Simula, Phys. Rev. D **73**, 114504 (2006).

[56] L. J. Cooper, C. T. Davies, J. Harrison, J. Komijani, and M. Wingate (HPQCD Collaboration), Phys. Rev. D **102**, 014513 (2020).

[57] G. P. Lepage, CORRFITTER Version 8.0.2 (https://github.com/gplepage/corrfitter).

[58] R. Dowdall, C. Davies, R. Horgan, G. Lepage, C. Monahan, J. Shigemitsu, and M. Wingate, Phys. Rev. D **100**, 094508 (2019).

[59] C.-K. Chow and M. B. Wise, Phys. Rev. D **48**, 5202 (1993).

[60] J. Laiho and R. S. Van de Water, Phys. Rev. D **73**, 054501 (2006).

[61] C. Aubin and C. Bernard, Phys. Rev. D **68**, 034014 (2003).

[62] B. Colquhoun, R. J. Dowdall, J. Koponen, C. T. H. Davies, and G. P. Lepage, Phys. Rev. D **93**, 034502 (2016).

[63] M. E. Luke, Phys. Lett. B **252**, 447 (1990).

[64] See Supplemental Material at http://link.aps.org/supplemental/10.1103/PhysRevD.109.094515 for numerical form factor results and additional plots.

[65] C. Bobeth, M. Bordone, N. Gubernari, M. Jung, and D. van Dyk, Eur. Phys. J. C **81**, 984 (2021).

[66] R. Aaij *et al.* (LHCb Collaboration), J. High Energy Phys. 12 (2020) 144.

[67] A. Sirlin, Nucl. Phys. **B196**, 83 (1982).

[68] D. Atwood and W. J. Marciano, Phys. Rev. D **41**, 1736 (1990).

[69] R. L. Workman *et al.* (Particle Data Group), Prog. Theor. Exp. Phys. **2022**, 083C01 (2022).

[70] M. Jung and D. M. Straub, J. High Energy Phys. 01 (2019) 009.

[71] M. Duraisamy, P. Sharma, and A. Datta, Phys. Rev. D **90**, 074013 (2014).

[72] C. Aubin and C. Bernard, Phys. Rev. D **73**, 014515 (2006).

[73] A. V. Manohar and M. B. Wise, *Heavy Quark Physics*, Cambridge Monographs on Particle Physics, Nuclear Physics and Cosmology (Cambridge University Press, Cambridge, England, 2000).